Review | Open Access

Chemical Synthesis

Lin *et al. Chem. Synth.* **2026**, *6*, 75 **DOI:**10.20517/cs.2026.32

Computational advances in electrochemical CO_2 reduction: design of copper-based and atomically dispersed catalysts, interfacial dynamics, and machine learning

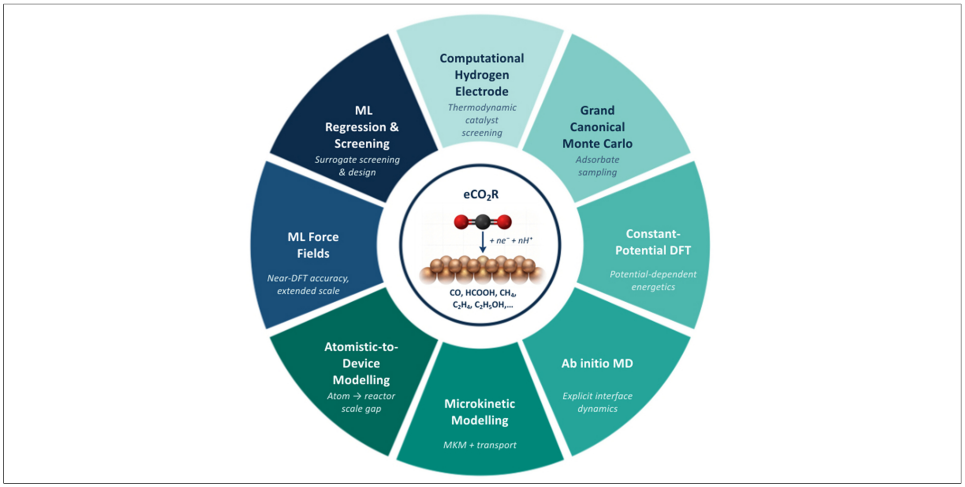
Wuyang Lin, Akshayini Muthuperiyanayagam, Devis Di Tommaso*

Keywords:
Electrochemical CO_2 reduction, density functional theory, machine learning, copper electrocatalysts, single-atom catalysts, reaction selectivity

Citation: Lin, W.; Muthuperiyanayagam, A.; Di Tommaso, D. Computational advances in electrochemical CO_2 reduction: design of copper-based and atomically dispersed catalysts, interfacial dynamics, and machine learning. *Chem. Synth.* **2026**, *6*, 75. https://dx.doi.org/10.20517/cs.2026.32

Received: 4 Jun 2026
First Decision: 24 Jun 2026
Revised: 3 Jul 2026
Accepted: 30 Jul 2026
Published: 28 Oct 2026

Academic Editors: Qinggong Zhu, Aicheng Chen
Copy Editor: Pei-Yun Wang
Production Editor: Pei-Yun Wang



Abstract

Electrochemical CO_2 reduction (eCO_2R) offers a route to convert CO_2 into fuels and chemicals using renewable electricity, but requires catalysts operating at low overpotential with high product selectivity. Computational studies have delivered essential mechanistic insight, yet a persistent gap remains between the idealised models used in most calculations and the structurally disordered, dynamically evolving catalysts encountered under operating conditions. This review surveys recent computational advances across three themes. The first addresses the methodological landscape, from fixed-electron density functional theory (DFT) and the computational hydrogen electrode (CHE) model through grand-canonical and constant-potential DFT, grand canonical Monte Carlo (GCMC), ab initio molecular dynamics (AIMD), machine-learning force fields (MLFFs), and data-driven machine-learning (ML) models. This establishes the capabilities and limitations of each. The second examines three catalyst classes: copper-based materials (high-index surfaces, amorphous systems, bimetallic alloys); single-atom catalysts (SACs), where coordination-environment engineering is the primary strategy for overcoming scaling-relation constraints; and dual-atom catalysts (DACs), where cooperative binding

Check for updates

School of Physical and Chemical Sciences, Queen Mary University of London, London E1 4NS, UK.

***Correspondence to:** Dr. Devis Di Tommaso, School of Physical and Chemical Sciences, Queen Mary University of London, London E1 4NS, UK. E-mail: d.ditommaso@qmul.ac.uk

between adjacent metal centres may lower barriers along C_2 pathways. Copper-based and atomically dispersed catalysts are the primary focus, representing the systems for which the computational literature is most extensive and the idealised-model/operando gap most acute. The third addresses operando phenomena such as potential-induced surface reconstruction, spectator co-adsorption, electrolyte cation effects, and pH-dependent selectivity that static slab models cannot capture but that critically determine performance. Current limitations are assessed and near-future directions proposed, including constant-potential MLFFs, nonlinear implicit solvation, multiscale atomistic-to-device workflows, and computation–operando spectroscopy integration.

INTRODUCTION

Rising atmospheric CO_2 concentrations, driven primarily by fossil fuel combustion and industrial activity, have become one of the defining scientific challenges of the twenty-first century. The IPCC Synthesis Report (2023) confirmed that global warming has already reached approximately 1.1 °C above pre-industrial levels[1]. Addressing this challenge requires not only reducing emissions at the source but also deploying strategies that actively convert CO_2 into useful products. Carbon capture and utilisation (CCU) offer such a pathway, treating CO_2 not merely as a waste product requiring geological storage, but as a carbon feedstock for fuels and chemicals[2]. Among CCU approaches, electrochemical CO_2 reduction (eCO_2R) is particularly attractive because it operates under ambient temperature and pressure, is compatible with renewable electricity, and enables control over reaction selectivity through catalyst design[2].

The practical challenge, however, lies in catalyst performance. CO_2 is a thermodynamically stable, kinetically inert molecule; its linear geometry and fully oxidized carbon centre (+4 formal oxidation state) make activation energetically demanding: the initial single-electron transfer requires significant geometric reorganization toward a bent $CO_2^{\delta-}$ configuration, imposing a large activation barrier even before subsequent protonation steps[3]. Electrocatalysts are therefore required to stabilise intermediates, lower free energy barriers along reduction pathways, and drive product formation at acceptable overpotentials. The diversity of possible products, including carbon monoxide (CO), formic acid (HCOOH), methane (CH_4), ethylene (C_2H_4), and ethanol (C_2H_5OH), each formed via distinct proton-coupled electron transfer (PCET) sequences, makes selectivity a central and unresolved problem[3]. Competing pathways, particularly the hydrogen evolution reaction (HER), further hinder efficiency under typical electrochemical conditions[3]. Copper (Cu) occupies a singular position in this landscape. It remains the only elemental metal to produce C_{2+} products with appreciable selectivity under standard electrochemical conditions, a consequence of its intermediate *CO binding strength that allows further protonation and C–C coupling rather than simple desorption or surface poisoning[4,5]. Yet this reactivity advantage comes at the cost of selectivity, and practical Cu-based catalysts consistently suffer from high overpotentials, mixed product distributions, and competition with HER. Efforts to address these limitations through surface facet engineering, nano-structuring, and bimetallic alloying have each yielded mechanistic insight and incremental improvements, but a unified design strategy remains lacking.

A critical and often underappreciated source of this gap is the disconnect between the idealised crystalline models used in theoretical studies and the structurally disordered, dynamically reconstructed catalysts observed experimentally. Most computational work has been anchored to well-defined low-index Cu surfaces or defect-modified crystalline slabs, which cannot represent the continuous distribution of local coordination environments characteristic of real catalysts under operating conditions[6-10]. Closing this gap requires new computational frameworks capable of explicitly treating structural heterogeneity, dynamic surface reconstruction, and the electrolyte environment. These are the three axes around which this review is organised. This review surveys recent advances in the theoretical and computational study of eCO_2R, organised around the key classes of catalyst design and methodology that have shaped the field. Section

"Computational methods for eCO_2R": outlines the principal computational approaches from conventional fixed-electron DFT and the computational hydrogen electrode (CHE) model through to grand canonical methods, molecular dynamics (MD), machine-learning force fields (MLFFs), and data-driven machine learning models for catalyst screening, establishing the methodological landscape within which catalyst insights are interpreted. The sections "Copper-based catalysts" and "Atomically dispersed catalysts: single-atom and dual-atom sites" address the main catalyst classes, organised by the nuclearity and dispersion of the active site, corresponding to the number of metal atoms forming the catalytic unit and whether they constitute an extended surface or are atomically dispersed on a support, rather than by metal identity: Section "Copper-based catalysts" covers Cu-based materials as extended, ensemble sites (high-index surfaces, nanostructures, amorphous systems, and bimetallic catalysts), and Section "Atomically dispersed catalysts: single-atom and dual-atom sites" covers atomically dispersed single-atom and dual-atom catalysts. On this axis, the same element recurs across classes, since dispersion rather than composition defines the catalytic behaviour. Section "Operando evolution and co-adsorption" addresses operando phenomena: potential-induced surface reconstruction, spectator-species co-adsorption, and electrolyte cation and pH effects that govern activity and selectivity under realistic conditions. Section "Challenges, limitations, and near-future directions of eCO_2R" concludes with an assessment of current limitations and near-future directions.

The scope of this review is focused on Cu-based and atomically dispersed (single- and dual-atom) catalysts, as these represent a significant part of both the experimental and the computational eCO_2R literature, and because the gap between idealised models and operando structure, which is the organising theme of this review, is most extensively studied for these systems.

Computational eCO_2R has been reviewed before, most comprehensively by Dattila *et al.*, whose 2021 survey of modelling under operating conditions spanned surface reconstruction, short-lived intermediates, electrolyte effects, and microkinetic and transport modelling[11]. The field has advanced considerably in the intervening years. Constant-potential and grand-canonical DFT, treated there as emerging approaches, have become routine tools for potential-dependent energetics; MLFFs have advanced from early neural-network potentials to models that make operando-scale dynamics tractable over nanosecond trajectories and large supercells; and atomically dispersed single- and dual-atom catalysts, largely absent from earlier operando-focused syntheses, have emerged as a major class with their own descriptor and coordination-engineering frameworks. The present review covers these developments, updating the methodological landscape and extending the catalyst scope accordingly.

Other recent reviews each take a narrower focus. Methodological reviews treat the field by technique: Re Fiorentin *et al.* frame computational electrocatalysis as a hierarchy from thermochemical models through grand-canonical DFT to MLFFs[12], and Govindarajan *et al.* examine open methodological questions such as the constant-potential *vs.* constant-charge choice and the need for systematic benchmarking[13]. However, neither is specific to eCO_2R or its catalyst classes. Catalyst-centred reviews focus on a single material family: Nitopi *et al.* provide a comprehensive account of Cu in aqueous electrolyte, structured by surface, composition, and electrolyte[3], and Li *et al.* survey Cu selectivity strategies by morphological, compositional, defect, and interfacial design[14], while Wang *et al.* extend the scope to catalyst and reactor-configuration co-design at the device level[15].

COMPUTATIONAL METHODS FOR eCO_2R: FROM THERMODYNAMIC FRAMEWORKS TO DATA-DRIVEN APPROACHES

A wide range of computational methods has been developed to study eCO_2R, because no single approach can simultaneously capture electrode potential, interfacial solvation, configurational disorder, reaction dynamics, and large-scale catalyst screening. Accordingly, the methods discussed in this section are organised from

relatively simple and efficient thermodynamic approaches to more realistic but computationally demanding dynamic and recently emerging data-driven frameworks. We begin with conventional fixed-electron DFT and the CHE, which provide a useful first-pass description of reaction energetics, and then move to grand canonical and statistical methods that better represent electrochemical boundary conditions and fluctuating surface compositions. Then, MD is introduced as an effective approach for treating explicit interfacial dynamics and analysing results derived from long dynamic trajectories. Finally, MLFFs and machine-learning (ML) models are introduced as complementary tools for treating explicit interfacial dynamics and accelerating catalyst discovery across large chemical spaces. A separate subsection (Section "Microkinetics, transport, and interfacial thermodynamics") surveys the mesoscale and thermodynamic tiers - microkinetic modelling, continuum transport and local-pH modelling, electric double-layer (EDL) theory, and surface Pourbaix analysis - that translate atomic-scale outputs into experimentally observable quantities and underpin the operando analysis of Section "Operando evolution and co-adsorption". The section closes with a synthesis of the full multiscale framework and a comparative summary of method capabilities (Section "Multiscale framework and methodological perspective", Table 1).

Conventional fixed-electrons DFT

Conventional fixed-electron DFT for eCO_2R is usually implemented through the CHE model[16]. In this framework, one computes adsorption energies and intermediate stabilities on a slab with a fixed number of electrons, often in a simplified surface-vacuum setting, and then imposes the electrochemical driving force afterwards. In the original Nørskov formulation, the proton–electron pair is referenced to the standard hydrogen electrode (SHE) so that, at pH = 0 and 0 V *vs.* SHE, $\mu(H^+ + e^-)$ is related to $\frac{1}{2}\mu(H_2)$[16]. The effect of bias enters through a $-eU_{SHE}$ term, with U_{SHE} the electrode potential referenced to the SHE, and pH is incorporated through the chemical potential of the proton. Relative to the pH = 0 reference, each proton involved in an elementary step contributes a correction of $k_BT\ln10 \times$ pH to the reaction free energy, corresponding to about 0.059 eV per pH unit at 298 K. As a result, proton-consuming steps become less favourable with increasing pH on the SHE scale, whereas this dependence is largely absorbed into the reference electrode when energies are expressed *vs.* the reversible hydrogen electrode (RHE), though this cancellation holds strictly only for concerted proton–electron transfer steps, not for chemical or electron-only steps whose energetics remain pH-independent on both scales. In this sense, CHE converts conventional surface DFT into potential- and pH-dependent reaction thermodynamics without explicitly simulating ions or a constant-potential electrode. CHE therefore makes it possible to build free-energy diagrams, identify the most uphill elementary step, estimate a theoretical limiting potential, U_L, defined as the least negative potential at which all electrochemical elementary steps become exergonic, $U_L = -\max_i(\Delta G_i)/e$, and map thermodynamic trends in adsorbate stability and product selectivity across catalyst families. These capabilities come with an important caveat: CHE cannot describe kinetic barriers, explicit solvent structure, or potential-dependent mechanism switching.

CHE is much less reliable when the question depends on explicit solvent structure, cation-specific effects, field-sensitive intermediates, decoupled sequential proton-transfer and electron-transfer steps, in which the two transfers do not occur concertedly, or quantitatively accurate activation barriers at a fixed electrode potential, or coverage-dependent lateral interactions between co-adsorbed intermediates whose competition determines surface populations under steady-state conditions; the implications of these limitations for eCO_2R mechanism studies are discussed further in Section "Beyond the CHE"[17-19]. Therefore, in the context of eCO_2R, conventional fixed-electron DFT with CHE is best viewed as a first-pass thermodynamic framework for promising catalyst screening rather than a complete high-accuracy electrochemical theory to resolve detailed catalytic mechanisms at realistic electrochemical interfaces.

Table 1. Comparison of the principal computational methods for eCO_2R surveyed in this review

Method	Physical question addressed	Key output	Main advantages	Principal limitations	Characteristic scale/cost	Ref.
CHE-DFT	Thermodynamic trends and descriptor-based screening across catalyst families	Free-energy diagrams; limiting potential $U_L = -\max(\Delta G_i)/e$; adsorbate-stability and selectivity trends	Computationally efficient; effective first-pass screening; potential and pH enter via -eU and the proton chemical potential without explicit ions	Strictly linear -eU correction; each step treated as concerted PCET; no explicit solvent, cation, field, or kinetic-barrier effects; fixed electron count	Low; single static slab	[16-19]
GC-DFT/constant-potential DFT	Potential-dependent energetics and charge redistribution; barriers at fixed potential (with NEB/dimer)	Potential-dependent adsorption energies, surface charge, and activation barriers; double-layer response	Holds electrode potential fixed ($\mu_e = -eU_{SHE}$); captures non-linear potential response; aligned with operational electrochemistry	Surface composition fixed per calculation; depends on implicit electrolyte/solvation model; higher cost than CHE	Moderate	[20-24]
GCMC	Equilibrium adsorbate populations and active-site coverages at fixed potential; adsorbate-induced reconstruction	Potential-dependent surface coverages; realistic structures; otherwise-hidden adsorption sites	Samples fluctuating coverage and co-adsorption; reveals sites inaccessible to static DFT; comparable to operando coverage measurements	Stochastic configurational sampling with no real-time dynamics; relies on DFT energetics; not suited to elementary barriers	Moderate–high (many DFT evaluations)	[25-30]
AIMD/enhanced sampling	Explicit interfacial dynamics; solvent structure, proton transfer, and solvent-coupled kinetics	Water orientation, H-bond lifetimes, ion pairing, proton-transfer rates; free-energy profiles and barriers (with MetaD/umbrella sampling)	DFT-level accuracy; explicit solvent and bond breaking; most realistic description of the interface	Trajectories of tens of ps over a few hundred atoms; rare events require enhanced sampling; very high cost	High; ~10-100 ps, ~10^2-10^3 atoms	[17,31-35]
MLFFs	Large-scale, long-time interfacial dynamics at near-DFT accuracy	Near-DFT energies and forces over large supercells and long trajectories	Near-DFT accuracy at a fraction of AIMD cost; extends length/time scales; on-the-fly active learning	Mostly trained at fixed electron count, not fixed potential; local energy decomposition omits long-range double-layer electrostatics; limited transferability outside the training domain	Ns over large supercells (after training)	[31,45-52]
ML regression models	Rapid property prediction, materials screening, and operating-condition optimisation across large design spaces	Predicted descriptors/limiting potentials; ranked candidates; structure–property maps	Fast surrogate screening; active-learning and inverse-design loops; scope far beyond one-at-a-time DFT	Bounded by training-data quality, coverage, and descriptor choice; transferability often untested; no community benchmark dataset	Very low at inference; cost shifts to training-data generation	[53-61]
Microkinetic modelling	Steady-state rates, surface coverages, and selectivity as a function of potential and pH	Turnover frequencies; partial current densities; Tafel slopes; potential/pH-dependent selectivity maps	Directly connects DFT-derived energetics to experimentally measurable polarisation behaviour	Rate predictions inherit the accuracy of energetic inputs; most models use CHE-derived thermodynamics, introducing only approximate potential dependence	Low (once energetic inputs are available); coupled differential equations	[62]
Continuum transport/local-pH modelling	Concentration gradients, local pH, and mass-transport limitations across the diffusion layer under operating current	Local surface pH $CO_2/HCO_3^-/CO_3^{2-}$ concentration profiles; limiting current densities	Captures the surface-pH rise (several pH units above bulk) invisible to atomistic models; critical for predicting selectivity at high current density	Decoupled from atomic-scale detail; systematic integration with elementary-step kinetics across the full electrode geometry remains unresolved	Continuum (FEM/FD); cell-geometry scale; moderate cost	[63,64]

EDL theory	Structure and electrostatic response of the inner and outer Helmholtz planes; ion specificity and cation effects	PZC; differential capacitance; inner- *vs.* outer-Helmholtz-plane charge distribution; cation-field coupling	Provides a framework for disentangling direct cation coordination (inner-Helmholtz-plane) from field effects (outer-Helmholtz-plane); guides interpretation of cation-specific activity	Simplified continuum EDL models neglect specific ion–surface chemistry; full atomistic EDL description requires AIMD or MLFF trajectories at high cost	Analytical/continuum to atomistic; depends on implementation	[19,36]
Surface Pourbaix diagrams	Thermodynamically stable surface termination and oxidation state as a function of potential and pH	Phase diagram of adsorbed/oxidised surface states; stable *OH, *H, oxide coverages under operating conditions	Predicts active surface state under reaction conditions from DFT energetics; essential baseline for interpreting reconstruction and disorder	Thermodynamic construction only; cannot describe kinetically trapped or metastable states that frequently govern operando behaviour	Low; single static slab per surface state (same cost tier as CHE-DFT)	[65-67]

eCO_2R: Electrochemical CO_2 reduction; CHE-DFT: computational hydrogen electrode-density functional theory; U_L: limiting potential; ΔG: reaction free energy; PCET: proton-coupled electron transfer; GC-DFT: grand canonical-density functional theory; NEB: nudged elastic band; GCMC: grand canonical Monte Carlo; AIMD: ab initio molecular dynamics; MLFFs: machine-learning force fields; ML: machine-learning; FEM: finite element method; FD: finite difference; EDL: electric double-layer; PZC: potential of zero charge.

Grand canonical and constant potential DFT

While CHE-based fixed-electron DFT is useful for constructing approximate free-energy landscapes, its inability to maintain a specific electrode potential limits its accuracy for genuinely potential-dependent electrochemical interfaces. This motivates the use of grand canonical DFT (GC-DFT). This method treats the electrode as an open electronic system coupled to an external electron reservoir, representing the potentiostat in an electrochemical cell, such that the electron chemical potential $\mu e = -eU_{SHE}$ is held fixed, where U_{SHE} is the applied electrode potential referenced to the SHE, and the number of electrons adjusts self-consistently to maintain the target electrode potential[20]. In practice, GC-DFT fixes the electrode potential by holding the electron chemical potential $\mu e = -eU$ constant while the number of electrons varies self-consistently; this constant-potential (grand canonical) treatment is the counterpart to a constant-charge (canonical) calculation, in which the electron number is fixed, and the potential is left to float. Realising a fixed potential requires the net charge of the cell to be neutralised and an absolute potential reference to be established, which is the role of the counter-charge model: the standard and more physical choice is an implicit Poisson–Boltzmann electrolyte, in which the compensating charge forms a diffuse ionic layer in a continuum electrolyte that also references the potential to the bulk solution, while a homogeneous (jellium) background charge is a cruder alternative that lacks such a reference. Implicit-electrolyte models are thus themselves a standard means of imposing constant potential, and the constant inner potential (CIP) formulation[20], which constrains the electrostatic potential at the electrode rather than the Fermi level, is an equivalent constant-potential scheme rather than an alternative to the counter-charge representation. The methodologically important distinction is therefore between constant-charge and constant-potential treatments, not between implicit-electrolyte counter-charge and the constant-potential formulations. That makes it better aligned with operational conditions in electrochemistry than conventional fixed-electron DFT. Moreover, GC-DFT can directly determine how adsorbate geometries, surface charge, reaction kinetics, and energetics change with electrode potential rather than relying on a linear estimation as the CHE model does.

Many studies indicate that the non-linear response between electrode potential and intermediate geometries, binding strength, and charge distribution may be neglected by an excessively simplified CHE model and lead to misleading results[21]. Non-linear dependence of intermediate geometry, binding strength, and surface charge on electrode potential has been documented in several eCO_2R-relevant systems[22,23]. Simplifying this response to a linear $-eU$ correction, as in CHE, can produce qualitatively incorrect predictions of the rate-determining step and preferred pathway. Furthermore, the CHE potential correction enters as a strictly

linear $-eU$ term applied uniformly to each electron-transfer step; it does not capture the non-linear dependence of intermediate geometry, binding strength, and surface charge on electrode potential that has been documented computationally for several eCO_2R-relevant systems. Fixed-electron DFT combined with transition-state search methods such as nudged elastic band (NEB) can provide first-order estimates of activation barriers at a given surface geometry, but the barrier is evaluated at a fixed electron count and the potential dependence is introduced only through a post hoc correction; however, this approach omits the non-linear response of the electric double layer and the effect of the potential of zero charge (PZC) on barrier heights, effects that are most self-consistently captured within a grand canonical framework. Additionally, the specific reaction mechanism may differ with the applied potential; for example, *CO dimerisation is more favourable at mild potentials while CO–CHO* coupling takes place at more reduced potentials for C_2 product formation[24].

Grand canonical DFT therefore provides a more realistic description of electrochemical interfaces under applied bias than static fixed-electron approaches. Nevertheless, grand canonical DFT still treats the surface composition as fixed during each calculation; the fluctuating populations of co-adsorbed intermediates under steady-state electrochemical conditions are more naturally addressed by grand canonical Monte Carlo (GCMC) sampling, introduced in the following subsection.

GCMC

GCMC methods are an ensemble-sampling method in which the catalyst surface exchanges adsorbates with a reservoir through stochastic insertion and deletion moves, accepted or rejected according to a Metropolis criterion based on DFT-computed binding energies, so that the number and identity of adsorbed species fluctuate at fixed temperature and chemical potentials[25]. The electrochemical driving force enters through the chemical potential of each electroactive adsorbate, which is coupled to the electrode potential U via $\mu_i(U) = \mu_i^0 - n_i e U_{SHE}$, where U_{SHE} is the electrode potential referenced to the SHE, n_i is the number of electrons transferred in forming species i from solution-phase reactants; varying U therefore shifts the relative stability of all adsorbates simultaneously and yields a potential-dependent surface coverage directly comparable to operando spectroscopic measurements. In electrocatalysis, the primary value of GCMC is not the calculation of elementary reaction barriers, but the identification of realistic catalyst structures, surface coverages, and active-site populations under operating conditions[25]. The dynamic competition between adsorbates can reveal active sites inaccessible to static DFT simulations[26], explicitly capture potential-dependent co-adsorption and site-blocking[27], and provide mechanistic insight into adsorbate-induced surface reconstruction[28]. In eCO_2R studies, the GCMC-DFT integrated method has been used to investigate surface reconstruction under operational conditions and uncover hidden adsorption sites that can be missed[27]. Additionally, large-scale GCMC simulations have been used to sample adsorbate-induced Cu surface roughening under eCO_2R conditions, linking high *H coverage to facet-dependent reconstruction and subsurface H incorporation[29]. GCMC provides statistically sampled, condition-dependent structures and coverages that can feed into DFT energetics, micro-kinetics, and selectivity analysis[30] [Figure 1]. The operando application of GCMC to Cu-based and single-atom catalyst (SAC) systems is discussed in detail in Section "Operando evolution and co-adsorption". Nevertheless, GCMC samples configurational space stochastically and does not propagate nuclear motion in time; capturing the real-time dynamics of interfacial solvent, ion transport, and proton transfer requires MD-based approaches, introduced in the following subsection.

Dynamic modelling

Even when realistic adsorbate coverages and surface compositions are established, for example through GCMC sampling, the electrochemical interface remains intrinsically dynamic: solvent molecules continuously reorient, hydrogen-bond networks fluctuate, and ions migrate on picosecond-to-nanosecond

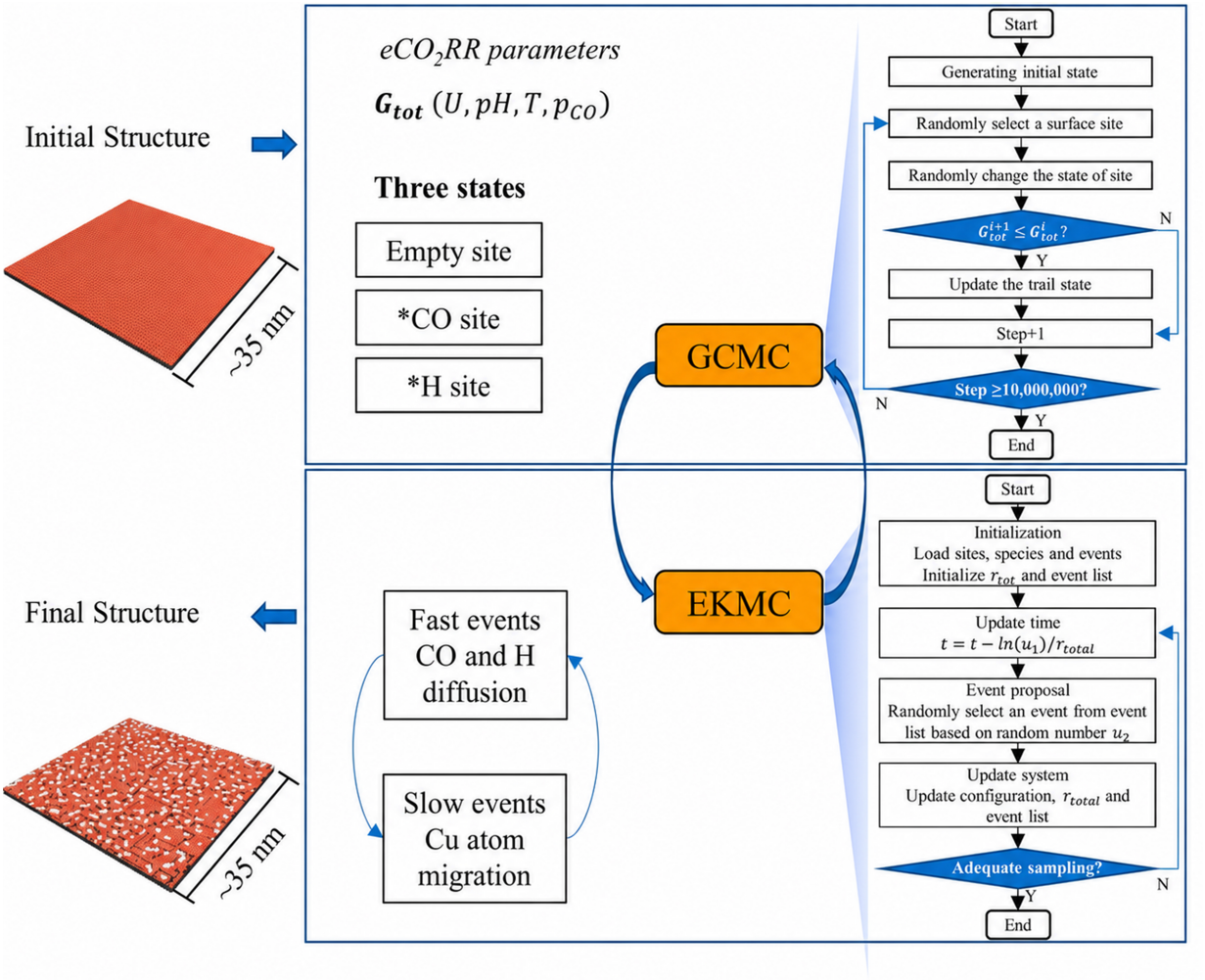


Figure 1. Coupled GCMC–EKMC workflow for simulating potential-dependent *CO/*H co-adsorption and Cu(100) surface reconstruction under eCO_2R conditions. Top left: Initial ordered Cu(100) surface (~35 nm lateral dimension)[30]. Top right: The GCMC loop samples the occupancy of each surface site (empty, *CO-occupied, or *H-occupied) under fixed electrochemical parameters (*U*, pH, *T*, *p*CO) via Metropolis-criterion acceptance until convergence: a proposed move is accepted with probability $min\{1, exp(-\Delta G_{tot}/k_BT)\}$, where $\Delta G_{tot} = G_{tot}^{i+1} - G_{tot}^{i}$, so that moves lowering the total free energy are always accepted, and those raising it are accepted with Boltzmann probability[30]. Bottom left: Final reconstructed Cu(100) surface (~35 nm), in which adsorbate-driven Cu atom migration produces a disordered morphology qualitatively distinct from the initial slab[30]. Bottom right: The converged GCMC coverage is passed to an EKMC loop, which propagates the surface in time by distinguishing fast (CO and H diffusion) from slow (Cu migration) events[30]. All panels reproduced with permission from Ref.[30]. Copyright © 2026 American Chemical Society. GCMC–EKMC: Grand canonical Monte Carl and environmental kinetic Monte Carlo; eCO_2R: electrochemical CO_2 reduction.

timescales that are inaccessible to static DFT or stochastic Monte Carlo methods. Capturing these effects requires MD simulations, in which nuclear positions are propagated in time according to forces derived either directly from DFT [ab initio molecular dynamics (AIMD)] or from a parameterised interatomic potential. In eCO_2R, AIMD is the most rigorous MD approach, providing explicit treatment of electronic structure, proton transfer, and bond breaking at the interface, but its high computational cost restricts accessible simulation times to tens of picoseconds and system sizes to a few hundred atoms[17]. Key interfacial quantities such as water orientation distributions, hydrogen-bond lifetimes, ion pairing at the double layer, and proton transfer rate constants are obtained as time-averaged observables over these trajectories and cannot be inferred from single static configurations[31]. Dynamic simulations therefore become essential when the chemical processes of interest depend on explicit solvent structure, ion-specific effects at the double layer, or kinetic bottlenecks involving proton or electron transfer steps that are sequential rather than concerted. However, the high cost of AIMD severely limits the length and timescales accessible, motivating

the development of MLFFs that can reproduce AIMD-quality forces at a fraction of the computational cost, as described in the following subsection.

AIMD provides DFT-level accuracy by propagating nuclear motion at the solvated electrochemical interface, with trajectories typically spanning 10-100 ps over systems of a few hundred atoms[32]. In eCO_2R, AIMD captures explicit water effects, proton shuttling through hydrogen-bond networks via the Grotthuss mechanism, dynamic adsorption and desorption of intermediates, short-range cation–intermediate interactions, and, when combined with enhanced sampling techniques such as metadynamics or umbrella sampling, free energy profiles and activation barriers along solvent-coupled reaction coordinates; all of these are inaccessible to static DFT calculations[33]. AIMD therefore provides the most chemically realistic description of the eCO_2R interface currently accessible to first-principles simulation, at the cost of trajectories limited to tens of picoseconds and systems of a few hundred atoms[34].

Given the computational cost of AIMD, trajectories are typically limited to 10-100 ps, often too short to directly observe key reaction steps such as intermediate protonation or C–C coupling, which occur on timescales inaccessible to unbiased simulation[32]. To address this limitation, metadynamics (MetaD) provides an effective approach to accelerate rare events by reconstructing the free energy surface (FES) along selected collective variables through the accumulation of a history-dependent bias potential that progressively fills free energy minima and drives the system across otherwise rarely visited transition states[35]. The key advantage of MetaD is that it transforms qualitative structural trajectories into quantitative free energy profiles and activation barriers for elementary steps too infrequent to be sampled within an unbiased trajectory. However, converged free energy profiles require long MetaD simulations that can themselves exceed the reach of AIMD, because convergence demands exhaustive sampling of all accessible free energy basins, a condition that becomes increasingly demanding as the complexity of the free energy landscape or the number of collective variables grows.

Classical force fields extend the spatial and temporal reach of atomistic simulation by replacing quantum mechanical force evaluation with analytical interatomic potential functions, eliminating the electronic structure calculation at each timestep and enabling trajectories of nanoseconds to microseconds over systems of millions of atoms[36-38]. Standard non-reactive force fields, such as TIP4P for water or the embedded atom method (EAM) for metal surfaces, assume a fixed bonding topology and cannot describe bond breaking or formation[39]. Reactive force fields such as ReaxFF overcome this restriction by using a bond-order formalism in which connectivity is determined dynamically from interatomic distances, allowing chemical reactions to be simulated at classical cost[40-42]. In eCO_2R, ReaxFF has been applied to long-time equilibration of the electrode–electrolyte interface and to investigating how surface modifiers influence interfacial water organisation and hydride dynamics, problems that are computationally intractable with AIMD. However, the accuracy of ReaxFF for bond-breaking chemistry depends critically on the quality of the parametrisation, which is typically derived from gas-phase or vacuum quantum mechanical reference data and therefore does not capture the potential-dependent charge redistribution, surface polarisation, or solvation effects that govern reactivity at electrochemical interfaces[34,41,43,44]. This transferability gap motivates the development of MLFFs, which retain the reactive flexibility and near-classical computational cost of empirical potentials while being trained directly on AIMD-quality data for the relevant interfacial environment, as described in the following subsection.

Machine learning forcefields

The spatial and temporal limitations of AIMD and enhanced-sampling approaches make it difficult to access the larger systems and longer trajectories needed to describe electrochemical interfaces under realistic operating conditions. MLFFs offer a practical route to extending such simulations by training interatomic

potentials on DFT energies and forces, reproducing the potential energy surface with near-DFT accuracy at a fraction of the computational cost of direct AIMD[45,46]. A key strategy for generating MLFFs is the on-the-fly active learning approach implemented in VASP by Jinnouchi *et al.*, in which the force field is updated during the simulation whenever the Bayesian uncertainty of the predicted energy exceeds a threshold, triggering a new DFT single-point calculation and automatically expanding the training set to include the new configuration, making the approach well suited to reactive, fluctuating interfaces whose configurational space cannot be anticipated in advance[47,48]. Beyond on-the-fly active learning, other widely used MLFF strategies include offline active-learning potentials[49], deep-potential models[50], equivariant graph neural network potentials such as MACE[51], and in the electrochemical context, constant-potential MLFFs adapted to charged electrochemical interfaces[52]. All of these retain near-DFT fidelity while extending accessible length and time scales far beyond conventional AIMD. In eCO_2R, MLFFs are particularly valuable when the catalyst–electrolyte interface is too dynamic for a static slab picture. Tian *et al.* applied an MLFF to the Cu–water interface under applied cathodic potential and found that potential-driven reorganisation of interfacial water and modification of the hydrogen-bond network measurably alter the barriers of key hydrogenation and ion-pair dissociation steps[31], effects entirely inaccessible to static slab models and only marginally resolvable within the timescales of conventional AIMD. Compared with AIMD, MLFFs make it practical to simulate larger supercells, longer trajectories, explicit solvent environments, and more extensive rare-event sampling, capturing solvent reorganisation, double-layer fluctuations, potential-dependent interface dynamics, competitive C–C coupling pathways, and large adsorbate-configuration ensembles. A current limitation is that most MLFFs are trained at fixed electron count rather than fixed electrode potential, which restricts their fidelity for genuinely potential-dependent phenomena; the development of constant-potential MLFFs represents one of the most important near-term methodological priorities in the field[52]. A further limitation shared by most current MLFFs is their use of a strictly local energy decomposition, in which each atomic contribution depends only on the chemical environment within a finite cutoff radius. This approximation neglects long-range electrostatic interactions from the charged double layer, restricts explicit representation of charge transfer between the metal surface and adsorbed intermediates, and cannot capture non-local through-metal coupling between co-adsorbed species, all of which contribute to adsorption energies and lateral interactions central to eCO_2R selectivity. Equivariant graph neural network (GNN) architectures with extended message-passing schemes[51] partially address this limitation, but a fully satisfactory treatment of long-range electrostatics within the MLFF framework for electrochemical interfaces remains an open methodological challenge, discussed further in Section "Challenges, limitations, and near-future directions of eCO_2R".

Machine learning regression models

Whereas MLFFs accelerate atomistic simulations by approximating the potential energy surface, a broader class of ML regression models addresses a complementary challenge: rapidly predicting catalytic properties, screening materials, and optimising operating conditions across large design spaces that are inaccessible to systematic DFT computation or experimental screening. Models in use for eCO_2R include decision-tree-based ensemble methods such as gradient boosting regression (GBR)[53] and random forest regression (RFR)[54], and graph-based architectures including GNNs[55,56], all used as surrogate models that map catalyst descriptors, atomic structures, or operating variables to target properties. Decision-tree-based models are especially effective when the input is a tabular descriptor set, as they can rapidly rank catalysts, interpolate structure–property trends, and narrow the search space before expensive first-principles validation [Figure 2][57], and are robust to noise and practical for feature importance ranking. Graph-based and transformer architectures become more powerful when the problem requires learning nonlinear relationships directly from atomic environments, adsorption-site geometry, or large combinatorial catalyst spaces[58]. The principal advantage of these ML models in eCO_2R is therefore not only speed, but scope: they enable a shift from one-candidate-at-a-time DFT computation toward fast surrogate screening, active-learning loops that

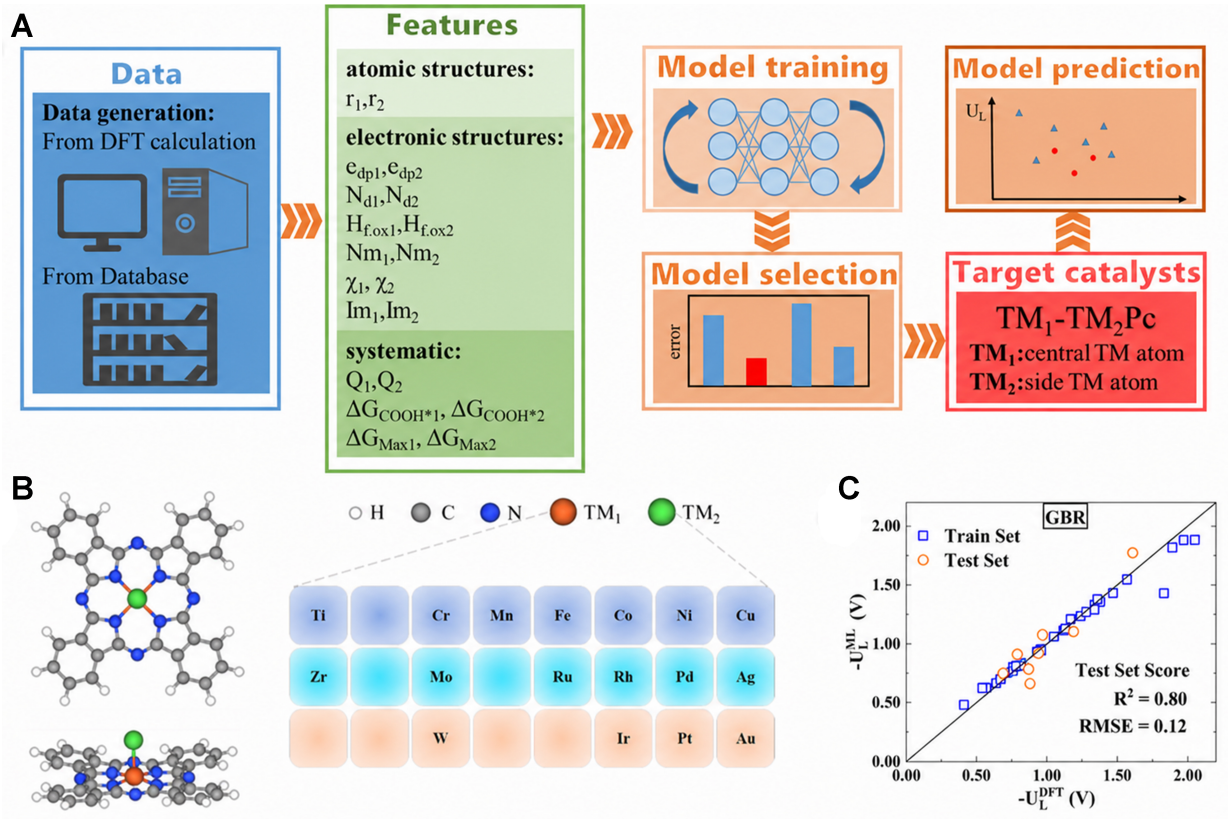


Figure 2. ML-accelerated prediction of catalytic activity for transition metal Pc DMSCs. (A) Workflow for predicting the limiting potential U_L: DFT- and database-derived features spanning atomic (r_1, r_2), electronic (e_d, N_d, $H_{f,ox}$, χ, I_m), and thermodynamic (Q, ΔG_{COOH^*}, ΔG_{Max}) descriptors are used for model training, model selection, and prediction of target TM_1–TM_2 Pc DMPcs, where TM_1 is the central and TM_2 the side transition-metal atom; (B) Structure of the Pc DMSCs and the transition metals surveyed; (C) Parity plot for the best-performing GBR model: DFT-computed *vs.* ML-predicted limiting potential ($-U_L$), with test-set R^2 = 0.80 and RMSE = 0.12 V. (A-C) Reprinted (adapted) with permission from Ref.[57]. Copyright © 2021 American Chemical Society. ML: Machine-learning; Pc DMSCs: phthalocyanine dual-metal-site catalysts; DFT: density functional theory; GBR: gradient boosting regression; RMSE: root mean squared error.

strategically select the most informative new DFT calculations to maximise model improvement at minimum computational cost, inverse catalyst design, and data-driven optimisation of electrolyser operating conditions[59].

Nevertheless, the predictive accuracy of ML regression models depends critically on the quality and coverage of the training data. Most eCO_2R models are trained on DFT adsorption energies computed for clean, idealised surfaces, and their transferability to structurally distinct catalysts, reconstructed surfaces, or co-adsorption environments is often untested. The absence of large, community-standardised benchmark datasets for eCO_2R, analogous to OC20 and OC22 for heterogeneous catalysis[60,61], represents a significant constraint on model generalisability. Furthermore, descriptor-based models are bounded by the informativeness of the chosen descriptors: if the descriptor set does not encode the effect of surface reconstruction, co-adsorbed spectators, or potential-dependent charge redistribution, the model will produce confident but unreliable predictions for the operating conditions most relevant to eCO_2R. These data and transferability limitations are discussed further as part of the near-term challenges in Section "Challenges, limitations, and near-future directions of eCO_2R".

Microkinetics, transport, and interfacial thermodynamics

The methods surveyed above describe the catalyst–electrolyte interface at the atomic scale, but several of the phenomena, which are discussed in the catalyst and operando sections that follow emerge only when this atomistic description is coupled to the kinetics of the full reaction network, to mass transport within the

diffusion layer, and to the thermodynamics of the electrified interface. Four method tiers bridge this gap and are surveyed briefly here, ahead of the operando discussion that depends on them.

Microkinetic modelling converts the elementary-step free energies and activation barriers obtained from CHE or GC-DFT into steady-state observables, namely surface coverages, turnover frequencies, partial current densities, and Tafel slopes, by solving the coupled rate equations of the reaction network[62]. For eCO_2R, microkinetic modelling is the tier that links the energetic landscapes of Sections "Conventional fixed-electrons DFT" and "Grand canonical and constant potential DFT" to experimentally measurable polarisation behaviour, and it is essential for rationalising why selectivity between C_1 and C_{2+} products shifts with potential and pH (Section "Electrolyte pH effects"). Its principal limitation is that the rate predictions inherit the accuracy of their energetic inputs, and most existing eCO_2R microkinetic models use CHE-derived thermodynamics, so that the potential dependence of the rates is introduced only approximately, a constraint discussed further as a near-future priority in Section "Bridging the atomistic-to-device scale gap".

Continuum transport and local-pH modelling describe the diffusion-layer region between the catalyst surface and the bulk electrolyte, solving the coupled transport of ionic species, alongside the homogeneous CO_2/bicarbonate/carbonate equilibria, to predict the local concentrations and the surface pH that the catalyst experiences[63,64]. Because proton-consuming reduction occurs preferentially at the cathode, these models account for the rise of surface pH by several units above the bulk value under operating current, an effect that is invisible to atomistic models of the surface alone but that strongly governs product selectivity (Section "Electrolyte pH effects"). The principal limitation is that continuum transport is typically decoupled from atomistic detail, and its systematic integration with elementary-step kinetics across the full electrode geometry remains an open multiscale problem (Section "Bridging the atomistic-to-device scale gap").

EDL theory describes the structure of the interfacial region, the inner and outer Helmholtz planes, the diffuse layer, the PZC, and the electric field across the double layer, using continuum descriptions such as the Gouy–Chapman–Stern and modified Poisson–Boltzmann models, or explicit double-layer DFT[19]. For eCO_2R, EDL theory provides the conceptual basis for the cation effects examined in Section "Electrolyte cation effects", where the distinction between inner-Helmholtz-plane coordination of CO_2 and outer-Helmholtz-plane field effects is precisely the distinction between two regions of the double layer. Continuum EDL models capture the mean-field electrostatics efficiently but omit the ion-specific and short-range chemical effects that explicit double-layer DFT and AIMD resolve at considerably higher cost.

Surface Pourbaix (electrochemical phase) diagrams map the thermodynamically stable surface termination and oxidation state as a function of applied potential and pH, by comparing the computed free energies of candidate adsorbed and oxidised configurations under the CHE or GC-DFT formalism[65-67]. For eCO_2R, this tier predicts which surface state, for example metallic Cu *vs.* residual oxide or hydroxide, or a given *OH/*H coverage, is thermodynamically favoured under operating conditions, and it therefore provides the thermodynamic baseline against which the potential-driven reconstruction of Section "Applied potential induced reconstruction and property change" and the disorder of amorphous and oxide-derived Cu in Section "Amorphous catalysts" are interpreted. Its principal limitation is that it is a purely thermodynamic construction and cannot by itself capture the kinetically trapped or metastable states that frequently dominate operando behaviour, motivating the dynamic methods introduced above (GCMC, molecular dynamics, and MLFFs).

Multiscale framework and methodological perspective

The computational approaches surveyed in this section constitute a multiscale framework for studying eCO_2R in which each method addresses a distinct but complementary aspect of the problem. Conventional fixed-electron DFT and the CHE model provide thermodynamic free-energy landscapes and activity

descriptors for catalyst screening; grand canonical DFT introduces explicit potential control and captures the non-linear electrochemical response of intermediate geometries, binding energies, and surface charge. GCMC extends this picture to fluctuating adsorbate populations and potential-dependent surface compositions through stochastic configurational sampling, while MD-based methods, from AIMD through enhanced-sampling approaches to MLFF-driven dynamics, reveal the real-time interfacial dynamics governing solvent structure, ion specificity, and proton transfer[68]. MLFFs extend the length and timescales accessible to near-DFT-quality atomistic simulation, and ML regression models enable rapid surrogate screening and data-driven catalyst design across chemical spaces that are inaccessible to systematic first-principles computation. Above the atomistic tiers, the interfacial-thermodynamic and continuum methods of Section "Microkinetics, transport, and interfacial thermodynamics" (surface Pourbaix diagrams, microkinetic modelling, and continuum transport) propagate this atomistic description to the steady-state coverages, turnover frequencies, and local-pH profiles that govern measurable cell behaviour, completing the hierarchy from electronic structure to electrode performance. Rather than competing alternatives, these methods form a hierarchy of approximations whose appropriate use is dictated by the physical question being asked; their capabilities, characteristic outputs, advantages, limitations, and accessible scales are compared in Table 1.

The following sections apply this methodological framework to three catalyst classes, Cu-based materials (Section "Copper-based catalysts"), single-atom and dual-atom catalysts (Section "Atomically dispersed catalysts"), and operando catalyst–electrolyte systems (Section "Operando evolution and co-adsorption"), with the objective of illustrating how the choice of computational approach determines which aspects of catalyst behaviour can be resolved and where the remaining gaps lie.

COPPER-BASED CATALYSTS

Copper-based catalysts occupy a central position in eCO_2R because Cu is the only elemental metal that produces C_{2+} products with appreciable selectivity under standard electrochemical conditions[69]. This selectivity originates from the intermediate binding strength of *CO on Cu, which satisfies the Sabatier criterion: binding strong enough to sustain the *CO surface coverage required for C–C coupling, yet weak enough to permit product desorption rather than surface poisoning[70]. The low-index Cu(111) and Cu(100) surfaces serve as the canonical computational benchmarks for eCO_2R: Cu(111), with a surface coordination number (CN) of 9, predominantly facilitates C_1 pathways such as CH_4 formation, while the more open Cu(100) surface, with CN 8, lowers the barrier for C–C coupling and favours C_{2+} products such as C_2H_4[71,72]. However, these idealised surfaces are poor representations of practical Cu electrodes: clean planar Cu(111) and Cu(100) exhibit sluggish CO_2 activation, low steady-state *CO coverage, and readily restructure under reaction conditions, generating surface states that differ substantially from the static models used in most computational studies[73]. These limitations define the central challenge of Cu-based catalyst design: raising *CO coverage and C–C coupling rates while suppressing competing H_2 evolution and maintaining selectivity toward a specific C_{2+} product. This motivates the four structural and compositional strategies surveyed in this section: high-index surfaces (Section "High-index surfaces"), finite-size nanostructures (Section "Nanostructures"), amorphous systems (Section "Amorphous catalysts"), and bimetallic modifications (Section "Bimetallic catalysts"). Each of these sections is an extended, ensemble realisation of the Cu active site, in contrast to the atomically dispersed sites of Section "Atomically dispersed catalyst".

High-index surfaces

Unlike the ideal Cu(111) and Cu(100) benchmarks, high-index surfaces expose step and kink atoms with lower and more diverse CNs that substantially influence CO_2 activation.

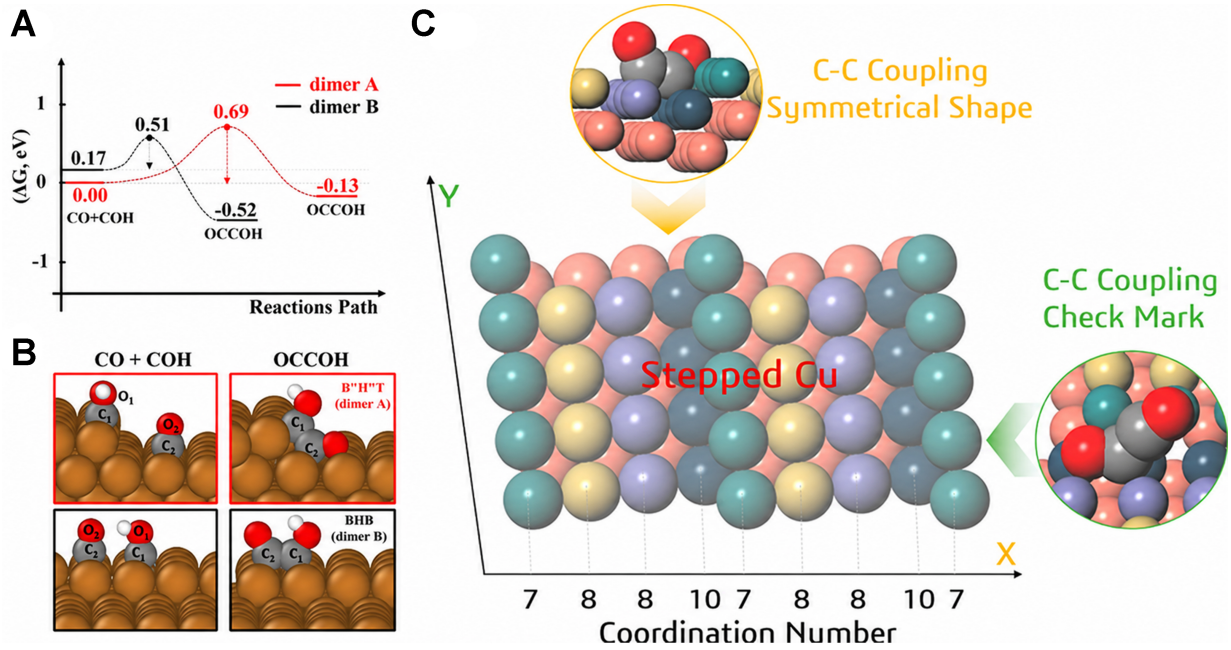


Figure 3. (A) Profiles of the potential energy surface (ΔG) for the CO–COH coupling on the Cu(711) surface; (B) Schematic representations of the optimised structures; (A and B) Reproduced with permission from Ref.[78]. Copyright © 2021 American Chemical Society; (C) Coordination number analysis for Cu(911) surface. Reproduced with permission from Ref.[79]. Copyright © 2022 American Chemical Society.

Unlike the ideal Cu(111) and Cu(100) benchmarks, high-index surfaces expose step and kink atoms with lower and more diverse CNs that substantially influence CO_2 activation[74]. Throughout this review, the coordination number (CN) of a surface atom denotes its first-neighbour coordination, that is, the number of nearest-neighbour metal atoms in the first coordination shell including subsurface neighbours, referenced to CN = 12 in bulk fcc Cu; on this scale, terrace atoms of Cu(111) and Cu(100) have CN = 9 and CN = 8, respectively. The binding strength of CO_2 scales with surface CN: computationally, Cheng *et al.* showed that the chemisorption energy of CO_2 decreases linearly with increasing CN, and that this trend is amplified under applied cathodic potential, where increased electron density at undercoordinated sites enhances charge transfer to CO_2 and strengthens chemisorption[73]. Verga *et al.* demonstrated that 7-coordinated step atoms on Cu(533) exhibit a substantially reduced CO_2 activation barrier relative to the 9-coordinated terrace atoms on the same surface[75].

Undercoordination also switches the binding mode of CO_2. On Cu(111), CO_2 is physiosorbed through weak van der Waals interactions, while on Cu(100) it is chemisorbed at bridge sites[76]; the less sterically constrained geometry of stepped atoms instead favours CO_2 adsorption at atop sites, which is associated with stronger binding, greater charge transfer, and more pronounced O–C–O bond bending[77]. As shown in Figure 3, enhanced CO_2 activation at lower-coordinated step and kink sites reduces the activation barrier of C–C coupling, which is critical for C_{2+} product formation[78,79]. However, C–C coupling itself proceeds more readily on terrace atoms: Cu(100) terraces exhibit a lower C–C coupling barrier than many high-index step geometries, indicating that step and terrace atoms play complementary roles: step atoms facilitate CO_2 chemisorption and *CO accumulation; terrace atoms govern the kinetics of C_2 product formation. This division of labour is the central mechanistic principle of high-index Cu surfaces, but it also defines their limitation: the periodic step geometry of extended high-index surfaces constrains the accessible coordination environment and cannot reproduce the full structural diversity of finite-size or disordered systems. These considerations motivate the move to nanostructured and amorphous Cu catalysts, discussed in the following subsections.

Nanostructures

Unlike extended surfaces, finite-size nanostructures, including nanoparticles and nanowires, are characterised by a high proportion of atoms at edges and corners with reduced CNs, introducing size- and shape-dependent electronic and geometric effects that substantially alter CO_2 activation and product selectivity relative to planar Cu electrodes. As with high-index surfaces, undercoordinated edge and corner sites show a systematic tendency to strengthen CO_2 binding and activation[80]. Edge and corner atoms typically exhibit CNs comparable to or lower than those of step atoms on high-index surfaces, and as nanoparticle size decreases, the surface-to-volume ratio increases, exposing a progressively greater proportion of these undercoordinated sites[81]. However, excessively strong *CO binding at highly undercoordinated sites suppresses C–C coupling by impeding the surface mobility and intermediate proximity required for dimerisation, with the result that C_1 products such as CO, HCOOH, and CH_4 are favoured over C_{2+} species[81].

At the sub-nanometre scale, the continuous size-effect trend gives way to discrete electronic-parity effects, a consequence of the discrete molecular-orbital structure of sub-nanometre clusters, in which the addition or removal of a single atom switches the ground-state spin multiplicity between open-shell (odd-*N*, doublet) and closed-shell (even-*N*, singlet) configurations, fundamentally altering the frontier orbital availability for CO_2 activation. Raju *et al.* showed that odd-numbered Cu clusters (Cu_3 and Cu_5) exhibited similar behaviour to one another but were clearly distinct from even-numbered clusters (Cu_4 and Cu_6), suggesting that the addition or removal of a single Cu atom can substantially alter activity and selectivity[82]. Wu *et al.* similarly showed that breaking the local symmetric structure of Cu_6 clusters promoted the formation of higher-value products[83]. As cluster size increases beyond the sub-nanometre regime, electronic-parity effects become less pronounced, but the CN distribution and size-dependent effects persist, influencing selectivity. Reske *et al.* investigated surface CN distribution [Figure 4A], revealing that the ratio of undercoordinated atoms increases dramatically when the diameter is smaller than 4 nm [Figure 4B][84]. Mistry *et al.* compared product selectivity on Cu clusters with different sizes, indicating that ultra-small clusters promote HER while moderate-sized clusters boost CH_4 formation [Figure 4C][85].

Moreover, the geometric shape of nanoclusters independently influences selectivity. Bu *et al.* reported that icosahedral clusters, exposing predominantly (111)-like facets, showed greater selectivity toward hydrocarbons, while truncated octahedral clusters, presenting both (100) and (111) facets, favoured CO formation[86]. Nabi *et al.* found that the most stable pure Cu clusters adopt low-symmetry, amorphous-like geometries, and that the geometric disorder associated with lower local coordination enhances CO_2 activation, particularly for CO production[87]. The observation that structural disorder at the nanoscale is a feature to be exploited rather than a defect to be minimised motivates the deliberate design of amorphous Cu-based catalysts as a distinct strategy, which is the subject of the following subsection.

Amorphous catalysts

In contrast to ordered crystalline surfaces characterised by well-defined facets, amorphous Cu-based catalysts lack long-range periodicity and instead expose a continuous distribution of local coordination environments, including dangling bonds and undercoordinated sites that are inaccessible on ideal crystalline surfaces. The potential of amorphous Cu for eCO_2R was first demonstrated experimentally by Duan *et al.*, who synthesised amorphous copper nanoparticles and achieved a total Faradaic efficiency (FE) of approximately 59% toward liquid products at -1.4 V *vs.* RHE, outperforming their crystalline counterparts[88]. Subsequent work by Xiong *et al.* reported amorphous CuBi catalysts with Faradaic efficiencies approaching 94.7% for formate[89], while Chen *et al.* achieved up to 84% FE toward C_{2+} products using Cu nanoparticles coated with an amorphous shell, with *in situ* surface-enhanced Raman spectroscopy (SERS) measurements directly linking enhanced *CO surface coverage to the coordination environment diversity of the amorphous phase[90]. These

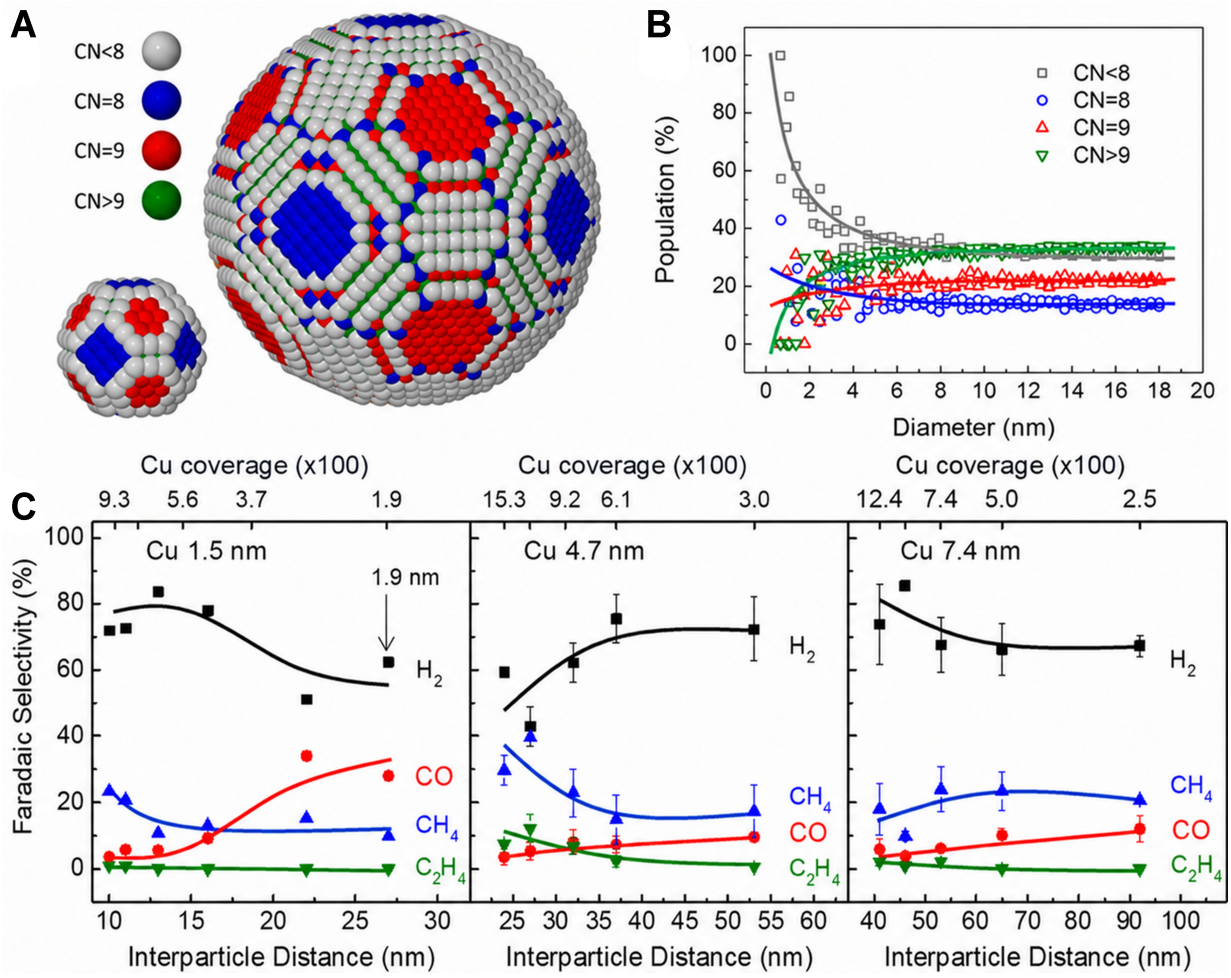


Figure 4. Size effect exhibited by small Cu nanoclusters. (A) Ball models of spherical Cu NPs with 2.2 and 6.9 nm diameters. Surface atoms are colour-coded according to their first-neighbour CN: CN < 8 (grey), CN = 8 (blue), CN = 9 (red), CN > 9 (green); (B) Population (relative ratio) of surface atoms with a specific CN as a function of particle diameter. (A and B) Reproduced with permission from Ref.[84], Copyright © 2014 American Chemical Society; (C) Size-dependent selectivity for main products. Reproduced with permission from Ref.[85], Copyright © 2016 American Chemical Society. NPs: Nanoparticles: CN: coordination number.

experimental observations have highlighted the need for computational approaches capable of explicitly capturing structural heterogeneity.

Early theoretical efforts largely focused on partially disordered Cu models. Liu *et al.* modelled oxide-derived Cu as a partially reduced nanocube containing subsurface oxygen, showing that local Cu distortion strengthens *CO binding and facilitates C–C coupling, though the disorder here is a by-product of oxide reduction rather than true amorphisation[10]. Song *et al.* applied AIMD-driven thermal reconstruction of a high-index Cu surface combined with oxygen doping to introduce local coordination disorder and investigate *CO adsorption and dimerisation, though the underlying structure remained anchored to a crystalline parent phase[91].

To overcome these limitations, Muthuperiyanayagam *et al.* developed a machine learning force field (ML-FF)- driven melt-and-quench framework to generate amorphous Cu and CuNi surfaces with coordination diversity. Comparison of the crystalline *c*-CuNi (111) and amorphous *a*-CuNi (i) surface models [Figure 5A and B] shows that amorphisation produces a structurally disordered surface containing a broader range of local coordination environments. This is reflected in the CN distributions of Cu and Ni atoms [Figure 5C-F],

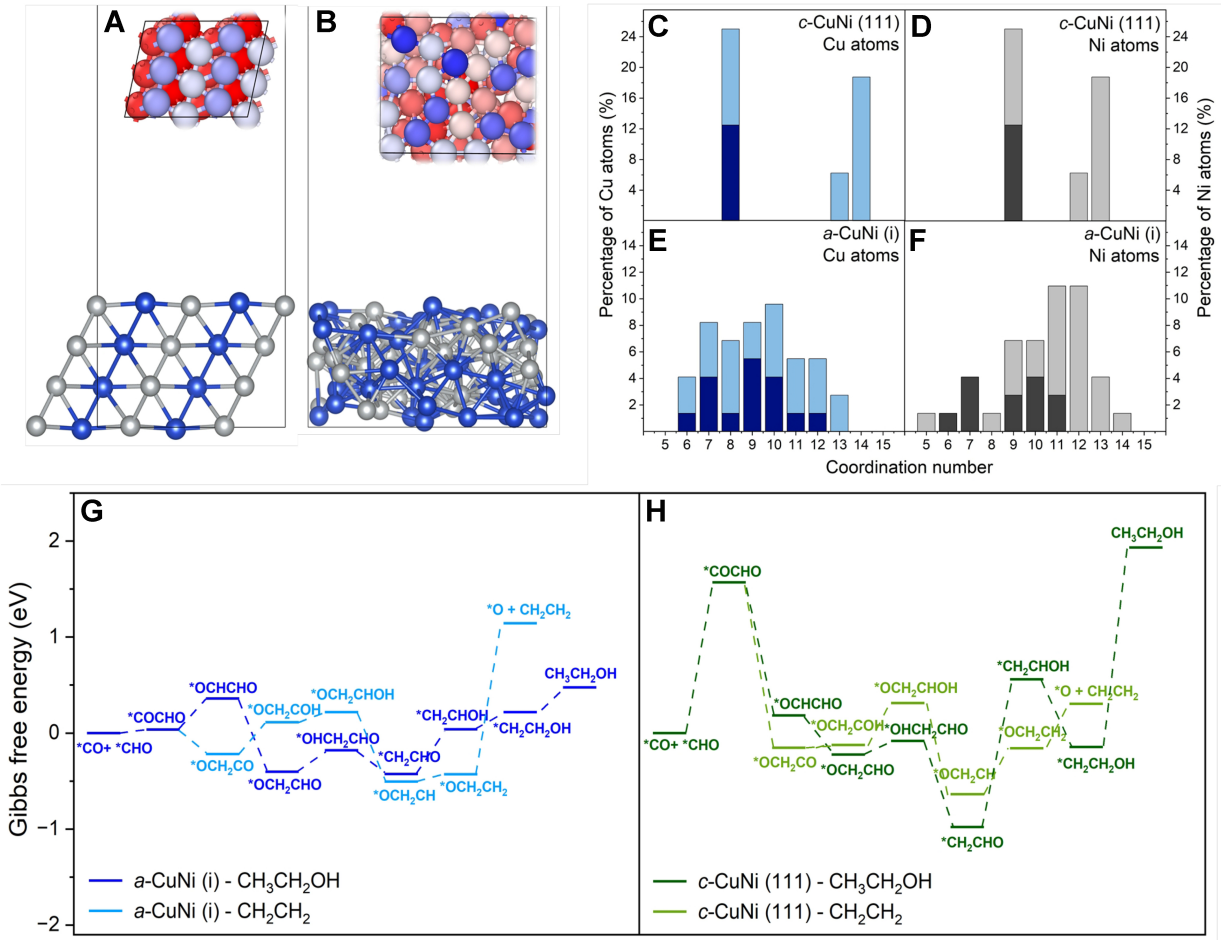


Figure 5. Atomic models of (A) crystalline *c*-CuNi (111) and (B) amorphous *a*-CuNi (i) surfaces colour-coded by CN; Distributions of CN for (C) Cu and (D) Ni atoms on *c*-CuNi (111); and (E) Cu and (F) Ni atoms on the *a*-CuNi (i) surface; grey and blue bars denote bulk and surface atoms, respectively; Computed Gibbs free energy diagrams for the electrochemical reduction of CO_2 to C_2H_5OH and C_2H_4 on (G) *a*-CuNi (i) and (H) *c*-CuNi (111) surfaces. (A-H) Reproduced from Ref.[93], under the terms of the Creative Commons CC-BY 4.0 license. CN: Coordination number.

where the amorphous surface exhibits a substantially larger population of undercoordinated surface sites than the crystalline alloy. These amorphous structures were subsequently characterised by DFT and automated adsorption site screening[92,93]. On amorphous Cu, DFT calculations revealed that undercoordinated sites with CNs equals to 5 and 6 support both CO_2 chemisorption and physisorption, compared to only CO_2 physisorption on the Cu(100) surface[87], with the chemisorbed state associated with significant charge transfer to CO_2 (-0.48e to -0.98e) and pronounced O–C–O bond bending (123.9-144.8°)[92]. For C_2 selectivity, amorphous CuNi alloys showed that adjacent undercoordinated Cu-Ni sites (CN = 6) significantly lower the free energy of CO–CHO coupling (ΔG = 0.04 eV) relative to crystalline CuNi (111) (ΔG = 1.57 eV) [Figure 5G and H][93]. This stabilisation was attributed to localised charge redistribution and enhanced overlap between Ni d states and O 2p orbitals, enabled by the geometric flexibility of the disordered environment, resulting in a preference for ethanol formation over ethylene[93].

Overall, these studies show that amorphisation introduces chemically distinct coordination and electronic environments absent from crystalline Cu surfaces, providing a mechanistic basis for enhanced CO_2 activation and altered selectivity toward C_1 and C_2 products. Structural disorder is one route to modifying the local electronic environment of Cu active sites; compositional modification through introduction of a second

metal offers a complementary and more precisely controllable strategy, which is the focus of the following subsection.

Bimetallic catalysts

Pure Cu catalysts exhibit poor product selectivity and are particularly ineffective for alcohol formation, including CH_3OH and C_2H_5OH. Introducing a second metal dopant generates bimetallic active sites that modify the local geometric and electronic structure, breaking the linear scaling relations between adsorption energies of related intermediates that constrain selectivity on single-metal surfaces and steering reaction pathways towards specific products[94,95]. Computational studies have established that local coordination geometry governs selectivity more strongly than bulk elemental composition, because asymmetric bimetallic sites interact preferentially with different functional groups of adsorbed intermediates, allowing *CO binding and *CHO or *OH stabilisation to be tuned independently[94,95]. The identity of the dopant determines the direction of this selectivity shift: noble metal dopants promote C_{2+} product formation, while post-transition metal dopants direct the reaction toward CO or formate.

Noble-metal dopants, exemplified by Cu–Pt, Cu–Ag, and Cu–Au motifs, promote C–C coupling through two complementary mechanisms. First, a *CO supply effect: the dopant acts as a local CO-producing site, increasing *CO coverage on adjacent Cu atoms and the probability of *CO–*CO encounters. Second, a strain-and-ligand effect: the dopant shifts the Cu *d*-band centre, tuning *CO and *CHO binding energies relative to pure Cu and repositioning the active site closer to the top of the activity volcano. Clark *et al.* showed that Ag dopants increase *CO surface coverage and simultaneously induce compressive strain at Cu sites, enhancing selectivity toward C_2 alcohols through both effects[96]. Zhi *et al.* demonstrated that hydrogen affinity and oxygen affinity of the dopant serve as useful descriptors for product selectivity, with moderate-affinity dopants such as Au and Pd facilitating pathways toward C_{2+} products[97]. Selectivity between hydrocarbons and alcohols within the C_{2+} manifold is further governed by the oxygen affinity of the dopant toward C_2 intermediates. As shown in Figure 6, dopants with higher oxygen affinity (Rh, Ir, Ru) favour C_2H_4 formation, while those with lower oxygen affinity (Pd, Ag, Au) direct selectivity toward C_2H_5OH. Furthermore, the comparison between RhCu and pure Cu catalysts clearly stresses that Rh doping enhances C_2H_4 selectivity, featuring higher FE and current density, while pure Cu produces more C_2H_5OH throughout the studied potential range[98].

Post-transition metal dopants such as Cu–In, Cu–Sn, and Cu–Zn motifs direct selectivity toward C_1 products through a distinct mechanism. Being more oxyphilic than Cu, these dopants stabilise oxygen-bound intermediates through M–O bonds, facilitating protonation at the carbon atom and thereby promoting formate formation[99-101]. Zhang *et al.* showed that trace Sn-doped Cu nanoparticles selectively boost CO formation, while increasing the surface Sn fraction to 50% substantially enhances HCOOH selectivity, a compositional switch that reflects the changing balance between *CO and *OCHO stabilisation as Sn coverage increases[102]. Wan *et al.* showed that phase-separated Cu–Zn bimetallic catalysts enhance CO selectivity through a reduced barrier for *COOH formation[103].

The four Cu-based catalyst strategies surveyed in this section, including high-index surfaces, finite-size nanostructures, amorphous systems, and bimetallic alloys, share a common design logic: each strategy modifies the local coordination environment or electronic structure of Cu active sites to raise steady-state *CO coverage, lower the C–C coupling barrier, or break the scaling relations that constrain selectivity on planar Cu electrodes. Structural heterogeneity, whether introduced through surface steps, finite-size disorder, amorphisation, or a second metal, consistently generates active sites with distinct electronic properties that are not accessible on ideal low-index surfaces and that computational studies based on static CHE-level DFT have only partially characterised. The operando behaviour of these systems, such as surface reconstruction under applied potential, competitive adsorbate populations, and electrolyte-specific

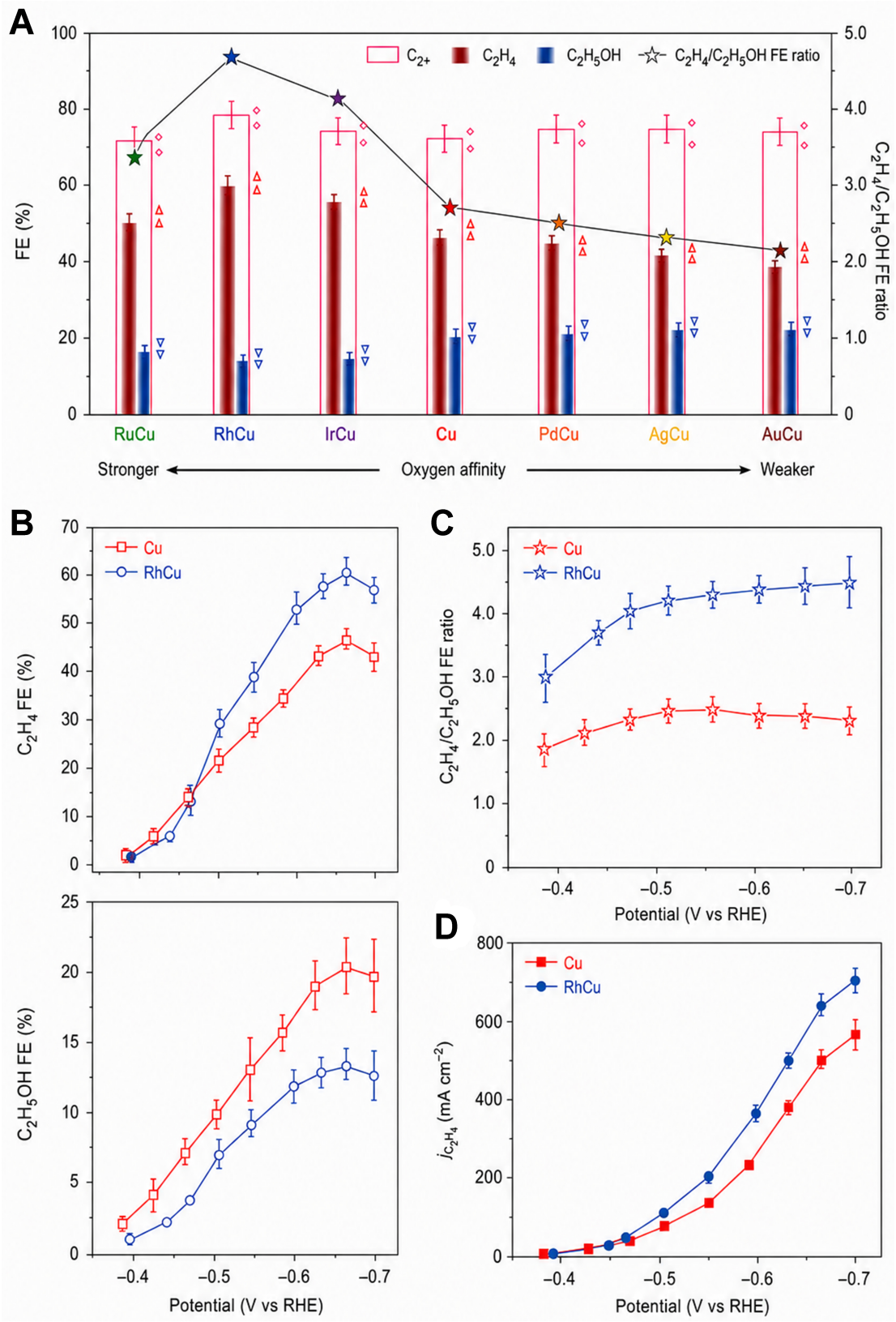


Figure 6. Electrocatalytic eCO_2R performance for different M-Cu bimetallic catalysts. (A) Oxygen-affinity-dependent selectivity; (B-D) selectivity and activity comparison between Cu and Rh-Cu catalysts. (A-D) Reproduced with permission from Ref.[98], Copyright © 2024 Springer Nature. eCO_2R: Electrochemical CO_2 reduction; FE: Faradaic efficiency; RHE: reversible hydrogen electrode.

interactions, introduces additional complexity that is addressed in Section "Operando evolution and co-adsorption".

All these designs operate through extended or ensemble active sites in which multiple surface atoms participate in catalysis; a fundamentally different approach concentrates activity at isolated metal centres, maximising atom-utilisation efficiency and offering independent control over the coordination environment and support interactions. This single-atom and dual-atom catalyst design philosophy is the subject of Section "Atomically dispersed catalysts: single-atom and dual-atom sites".

ATOMICALLY DISPERSED CATALYSTS: SINGLE-ATOM AND DUAL-ATOM SITES

Whereas the Cu-based catalysts of Section "Copper-based catalysts" act through extended, ensemble sites, this section turns to the opposite limit of the nuclearity axis: atomically dispersed catalysts, in which the active unit is reduced to a single metal atom (SACs, Sections "Single-atom M–N_4 sites on nitrogen-doped graphene", "Alternative supports for SACs beyond conventional graphene", and "Coordination environments of SACs") or a pair of adjacent atoms (dual-atom catalysts, DACs; Section "DACs")[104]. Concentrating activity at isolated centres maximises atom-utilisation efficiency and, more importantly for mechanism, decouples the active site from the collective electronic structure of an extended surface, so that selectivity is governed by the first- and second-shell coordination environment and the support rather than by facet or ensemble effects.

This architecture maximises metal atom utilisation and can generate highly dispersed, tunable active sites, making SACs attractive for reactions where activity, selectivity, and precious-metal utilisation are critical [Figure 7][105,106]. A representative feature of SACs is the strong interaction between the single metal atom and the coordination environment and support, which means the catalytic behaviours can be regulated not only by changing the active centre but also by tuning the ligands and defects in the vicinity as well as the support. Common supports include metal oxides[107,108], metal sulphides[109,110], carbon materials[111,112], and other defect-rich surfaces that can anchor isolated atoms and tune their electronic structure. The study and application of SACs in the field of electrocatalysis has developed rapidly since the pioneering work of Zhang's group in 2011[113].

Single-atom M–N_4 sites on nitrogen-doped graphene

Graphene-supported SACs with N_4-moieties are among the most interpretable model systems in electrocatalytic studies for eCO_2R[114]. The active site is sufficiently simple for catalytic mechanism investigations and catalytic performance regulation toward specific reactions[115,116]. Electrically conductive graphene supports that can be readily integrated into electrodes enable efficient electron transfer to atomically dispersed active sites, and support engineering of graphene can tune the local electronic structure and enhance eCO_2R kinetics[117]. Table 2 lists typical SACs as well as the corresponding main products. Graphene-supported SACs can also exhibit good durability in eCO_2R; for example, isolated Ni single atoms in graphene nanosheets maintained stable CO_2 electrolysis for about 20 h, with post-reaction spectroscopy indicating retention of atomically dispersed active sites[128]. Unlike conventional Cu-based catalysts that produce diverse products at the cost of poor selectivity, graphene-supported (Fe, Co or Ni) SACs demonstrated exceptional selectivity to C_1 products such as CO, with FE over 90%[118,129,130]. The impressive selectivity toward HCOOH or CH_4 is also reported by altering the metal centre to In or Zn, respectively[120,121].

The dependence of product selectivity on the metal identity reflects the underlying *d*-electron configuration of the active centre: computational screening of metalloporphyrin analogues of M–N_4 moieties across 110 systems has shown that d^6 and d^7 configurations favour CO_2 chemisorption and charge transfer, while d^{10}

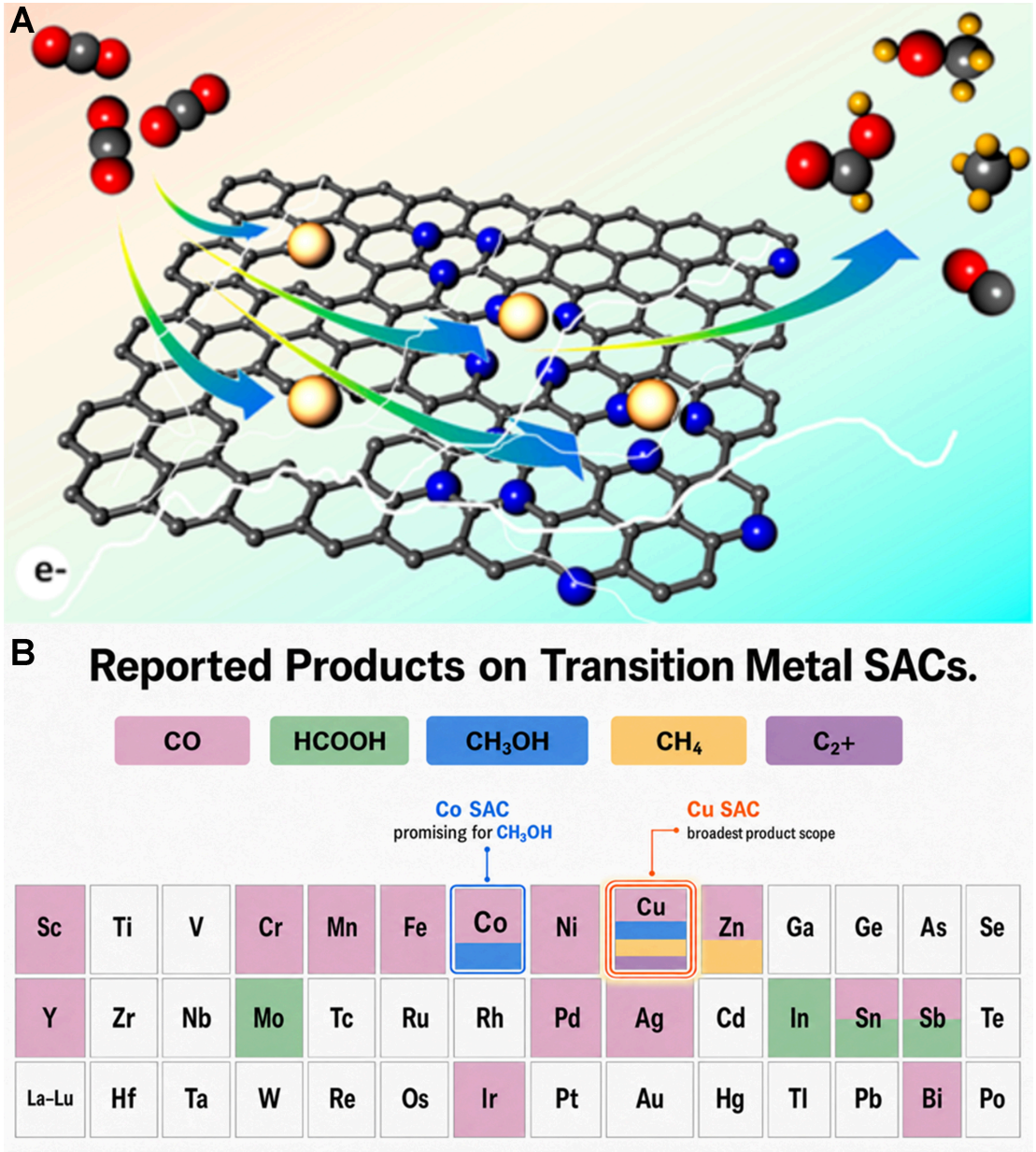


Figure 7. Overview of SACs for eCO_2R. (A) Schematic of M–N–C active-site motifs embedded in a nitrogen-doped carbon support, and the corresponding C_1 (CO, HCOOH, CH_3OH, CH_4) product distributions accessible via eCO_2R. Reproduced with permission from Ref.[105], Copyright © 2020 American Chemical Society; (B) Periodic-table map of transition-metal SACs investigated computationally and/or experimentally, colour-coded by primary reduction product selectivity (CO, HCOOH, CH_3OH, CH_4, and C_{2+}). Adapted from Ref.[106], Copyright © 2021 Royal Society of Chemistry. SACs: Single-atom catalysts; eCO_2R: electrochemical CO_2 reduction.

centres (Cu) are largely inactive toward CO_2 activation, a trend consistent with the selectivity patterns observed in graphene-supported SACs[131].

Consistent with this trend, Zn and Cu centres in symmetric M–N_4 coordination are weak CO_2 activators and, where active, yield CO as the dominant product. The CH_4-selective entries in Table 2 are therefore not representative of these metals in the N4 motif: methane selectivity is achieved in both cases by departing from it, through the microporous N-doped carbon environment of the Zn catalyst[120] and through boron substitution to give the Cu–N_2B_2 site[126]. These results anticipate the coordination-environment strategies examined in Section "Coordination environments of SACs".

Table 2. Selected experimentally reported SACs for eCO_2R

Active centre	Support	Coordination environment	Main product	FE	Potential (V)	Ref.
Fe	Graphene	N_4	CO	94%	-0.58	[117]
Co	Graphene	N_4	CO	> 90%	-0.76	[118]
Ni	Graphene	N_4	CO	92%	-0.68	[119]
Zn	N-doped carbon	N_4	CH_4	85%	-1.8 (*vs.* SCE)	[120]
In	Carbon matrix	N_4	$HCOO^-$	96%	-0.65	[121]
Mn	g-C_3N_4@CNT	N_3	CO	98.8%	-0.55	[112]
CoPc	MXene	N_4	CH_3OH	39%	-1.0	[122]
CoPc	CNT	N_4	CH_3OH	> 60%	-0.9	[123]
CoPc	CNT	N_4	CH_3OH	> 40%	-0.94	[124]
Ni	Carbon matrix	N_1C_3	CO	98%	-0.7/-1.3	[125]
Cu	Carbon matrix	N_2B_2	CH_4	73%	-1.46	[126]
Ni	Carbon matrix	N_4O	CO	97.2%	-0.56/-1.06	[127]
Co	Carbon matrix	N_3S_1	CO	98%	-0.52	[116]

Entries are chosen to span the range of accessible products rather than to represent the modal behaviour of each metal centre. Potentials are quoted *vs.* RHE unless otherwise stated. CoPc denotes a single Co atom anchored in Pc. FEs are maximum values at the stated potential and are not directly comparable across entries: measurements were performed in different cell configurations and at partial current densities differing by more than two orders of magnitude. For Ref.[117], 94% corresponds to a CO partial current density of 4.5 $mA{\cdot}cm^{-2}$ in CO_2-saturated aqueous $KHCO_3$; for Ref.[126], 73% corresponds to a CH_4 partial current density approaching 462 $mA{\cdot}cm^{-2}$. SACs: Single-atom catalysts; eCO_2R: electrochemical CO_2 reduction; FE: Faradaic efficiency; SCE: saturated calomel electrode; CNT: carbon nanotube; RHE: reversible hydrogen electrode.

Graphene-supported M–N_4 SACs face an intrinsic limitation imposed by scaling relations: the free energies of *COOH formation (ΔG_{*COOH}) and *CO adsorption (ΔG_{*CO}) are linearly correlated across different metal centres because both quantities are governed by the same electronic descriptor, the metal–nitrogen interaction strength, which determines the electron-donating capacity of all eCO_2R intermediates that coordinate through carbon or oxygen to the metal centre[132]. Therefore, the thermodynamics of CO_2 activation (via *COOH formation) and CO release cannot be independently optimised within the M–N_4 motif by varying the metal alone. A metal centre that stabilises *COOH sufficiently to reduce the thermodynamic cost of the first PCET step tends, along the scaling line, to bind *CO too strongly for facile desorption; conversely, a metal centre that releases CO readily tends to present too high a thermodynamic cost for *COOH formation. This trade-off, which is a statistical correlation rather than a thermodynamic inevitability, explains why most reported graphene-supported M–N_4 SACs are highly selective CO producers, operating near the optimal point of the *COOH/*CO scaling line, but cannot access the further-reduced products CH_4 or CH_3OH, which require sustained *CO coverage and subsequent hydrogenation steps that strong *CO binding precludes[133].

At the molecular level, NBO analysis of M–POR systems, which are structural analogues of M–N_4 sites, confirms that electron-withdrawing coordination environments increase orbital splitting at the metal centre, suppressing CO_2 activation capacity, while electron-donating ligands enhance it[131]; this ligand-field sensitivity underpins the rationale for coordination environment engineering as a route to shift the *COOH/*CO scaling line.

Moreover, the dispersed active site cannot stabilise two C_1 intermediates simultaneously, which accounts for the absence of C_2 intermediates[134]. To break the notorious "scaling relations", a few promising ideas have been proposed, such as support engineering, synergistic effects in heterogeneous dual atom pairs, asymmetric coordination environments, and ligand co-adsorption[135].

Alternative supports for SACs beyond conventional graphene

The scaling relation constraints inherent to graphene-supported M–N_4 SACs motivate exploration of alternative supports that can provide less symmetric coordination environments, stronger metal anchoring, and modified charge-transfer characteristics. Graphitic carbon nitride (g-C_3N_4), a two-dimensional polymeric semiconductor with sp^2-hybridised C and N atoms arranged in heptazine or triazine units, is the most widely investigated alternative, offering M–N_3 coordination environments that partially decouple CO_2 and CO binding energies and enabling selectivity toward products beyond CO. Although its electrical conductivity is lower compared to graphene, g-C_3N_4-supported SACs offer less symmetric coordination environments, stronger intrinsic single-atom anchoring, and more tuneable charge transfer. Recent studies reported that M-N_3 local environments broadly existed on g-C_3N_4; such asymmetric coordination environments impair the correlation of adsorption energy between CO_2 and CO[110]; N-rich local environments inherently contribute to stronger anchoring of metal atoms with fewer defects and less local distortion compared with that on N_4-doped graphene, and they provide an effective leverage to tune local electronic structures[136,137]. More importantly, SACs supported on g-C_3N_4 can steer reactions toward further reduced C_1 products beyond CO. For example, Zhu *et al.* reported that Cr-g-C_3N_4 boosted CH_4 and CH_3OH formation[137], while Shui *et al.* claimed that CH_3OH was the most favourable product on Au- and Ag-g-C_3N_4[138].

Beyond g-C_3N_4, other two-dimensional materials such as MXenes[139,140] and MoS_2[141-144] have also been widely investigated as supports for SACs due to tuneable electronic structures that facilitate HCOOH formation or CO reduction to CH_4 or CH_3OH. In addition to planar 2D supports, carbon nanotubes (CNTs), characterised by adjustable diameters and surface strains, are a typical 1D support for SAC anchoring. Wang *et al.* reported that sluggish proton-electron transfer was the main bottleneck in eCO_2R, which can be improved by utilising highly conductive CNTs to accelerate reaction kinetics[145]. Similarly, the curved surface of CNTs also contributes to breaking the "scaling relations", as previous literature reported that Cr-, Fe-, and Co-N_4 SACs can produce CH_4 or CH_3OH[146,147], while the asymmetric coordination environments on boron nitride nanotubes (BNNT) open the pathway toward CH_4 and HCOOH[148-150]. Theoretical calculations indicate that highly curved nanotubes can upshift the d-band centre of the active site[147]; therefore, retaining adsorbed *CO, while lowly curved nanotubes decrease the interaction with intermediates[151]. Experimental observations confirm that the FE of CO is negatively correlated with the curvature of nanotubes[152], which aligns well with theoretical predictions.

Furthermore, it is also noteworthy that phthalocyanine (Pc), featuring a planar N_4-coordinated cavity, is widely used as the support for SACs in electrocatalysis. Recent studies suggest that anchoring the CoPc SAC on highly curved CNTs leads to notable structural deformation and electronic redistribution around the Co active site, which lowers the CO_2 activation barrier[124]. Intriguingly, other related work claimed that CoPc on CNTs with the appropriate diameter exhibits CH_3OH selectivity, as shown in Figure 8[153], rather than CO or H_2 as previously reported on Co-N_4-graphene[118,154]. Since the similarity of the first coordination shell motif between Co-N_4-graphene and CoPc, the distinct selectivity may originate from the discrepancy of global structures. Wang's group proposed that Co-N_4-graphene and CoPc exhibit different PZC; adding vacancies on Co-N_4-graphene could narrow its PZC gap with CoPc and might facilitate CH_3OH formation on Co-N_4-graphene[155].

The enhanced current density observed in the flow cell configuration [Figure 8D] corroborates the mechanistic picture: curvature-induced electronic redistribution at the Co centre not only steers selectivity toward CH_3OH but simultaneously lowers the kinetic barrier to CO_2 activation, producing measurably higher partial current densities than those recorded on uncurved CoPc or Co–N_4–graphene analogues. Collectively, these findings demonstrate that global structural features, including support curvature and PZC,

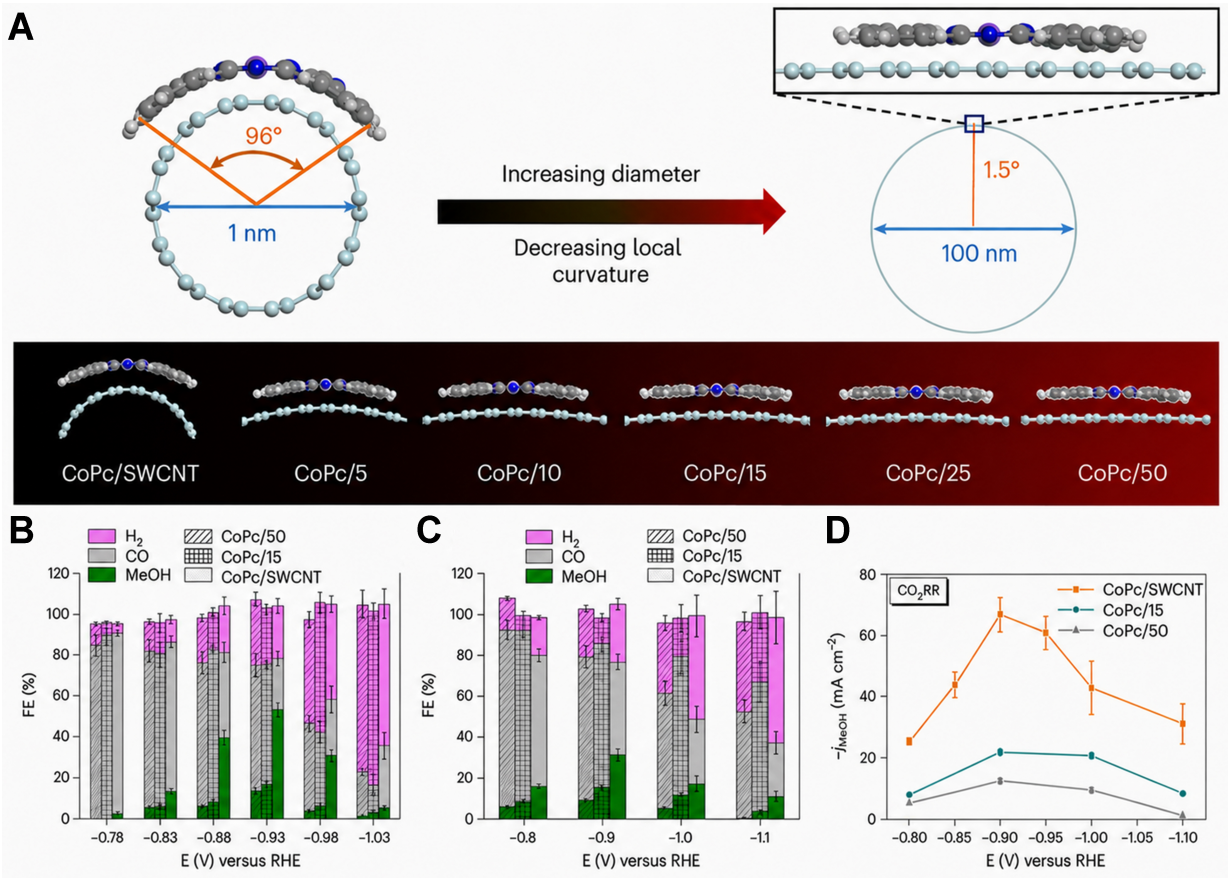


Figure 8. CoPc catalysts supported on a CNT for eCO_2R. (A) Curvature-induced local strain effect; (B) FE of CH_3OH, CO and H_2 in an H-cell with 0.5 M $KHCO_3$ as electrolyte; (C) FE of CH_3OH, CO and H_2 in a flow cell with 0.1 M KOH + 3 M KCl as electrolyte; (D) Current density in a flow cell. (A-D) reproduced from Ref.[153] under the terms of the Creative Commons CC-BY 4.0 license. CNT: Carbon nanotube; eCO_2R: electrochemical CO_2 reduction; FE: Faradaic efficiency; SWCNT: single-walled carbon nanotubes; RHE: reversible hydrogen electrode.

exert a determining influence on SAC selectivity that is not captured by models restricted to the first coordination shell.

This finding demonstrates that atoms beyond the immediate first coordination exert measurable influence on SAC selectivity, a point that has been underappreciated in studies focused exclusively on the metal centre and its nearest ligands. Recognising that both the support and the global structure modulate catalytic behaviour, the most direct route to active-site engineering remains the deliberate modification of the first-shell coordination environment itself, which is addressed in the following subsection.

Coordination environments of SACs

While the symmetric M–N_4 motif has been the most extensively studied coordination environment in graphene-supported SACs, a range of asymmetric configurations including N_3[110], N_5[156], N_3C_1[157], N_2C_2[158] and N_1C_3[125] have been proposed and experimentally validated for eCO_2R, each offering distinct activity–stability trade-offs relative to the N_4 benchmark. Theoretically, Hossain *et al.* predicted that although the Ni–N_4 motif delivers the highest current at more negative potential, the Ni-N_2C_2 and Ni-N_3C_1 exhibit lower onset potential for eCO_2R[23]. Han *et al.* identified the true active sites in Ni–N–C catalysts under

operational conditions, establishing that the Ni–N_3C_1 motif is the most robust and active configuration and showing that spatial separation of distinct active sites enhances product selectivity[159]. Luo *et al.* systematically substituted N with C in the Ni–N_4 motif and showed that increasing the number of C neighbours strengthens both *COOH and *CO binding, with Ni–N_3C_1 giving the lowest energy cost for the potential-limiting step among the motifs examined[160].

An important exception to the C-substitution trend is the N_5-coordinated motif, whose special local structure, comprising the symmetric N_4 configuration augmented by one axial N atom bound out-of-plane to the active centre, reduces the *COOH formation barrier and facilitates CO desorption, addressing the principal weaknesses of the N_4 site without incurring the poisoning risk associated with C substitution[156,161].

M–N_4 coordination confers thermodynamic stability on the active site and suppresses HER through weaker H adsorption, but the correspondingly weak intermediate binding raises concerns regarding insufficient CO_2 activation and high onset potentials for products beyond CO. Substituting N with C atoms improves activity at the cost of reduced active-site stability and an increased risk of intermediate poisoning or elevated HER selectivity, a trade-off that requires careful management in catalyst design.

B-, O-, and S-decorated coordination environments provide further routes to tune catalytic performance. B strengthens intermediate binding and promotes more deeply reduced products: Dai *et al.* showed that replacing N with B in the Cu–N_4 site strengthens *CO and *CHO binding, promoting CH_4 formation[126], while Kong *et al.* demonstrated that B in the first coordination shell promotes CH_4 formation whereas second-shell B has no equivalent effect[162]. As with C-substituted motifs, B coordination can produce excessively strong intermediate binding, impairing catalytic performance through active-site poisoning. O-coordinated environments substantially weaken intermediate binding, restricting selectivity to CO as the sole eCO_2R product[127]. As a softer and less electronegative ligand than N, S donates electron density more effectively to the metal centre, partially relieving the excessive metal–N covalency of M–N_4 sites and restoring intermediate binding to a more favourable range; Fe– and Co–S_1N_3 SACs accordingly outperform their N_4 counterparts[116,163].

Coordination-environment engineering thus provides a powerful and tunable route to control the stability, adsorption energetics, and product selectivity of SACs, and represents one of the most effective strategies for overcoming the limitations of conventional M–N_4 motifs in eCO_2R. A complementary approach, rather than modifying the ligand environment of a single metal atom, is to introduce a second adjacent metal centre, creating a dual-atom site in which cooperative binding between two atoms can stabilise pairs of intermediates simultaneously and enable C–C coupling pathways that are structurally inaccessible to isolated SAC sites; this is the subject of the following subsection.

DACs

DACs consist of dispersed metal atom pairs, either homonuclear (two identical metal atoms) or heteronuclear (two distinct metals). They retain the high atom utilisation of SACs while the second metal centre cooperatively tunes adsorption energetics, charge distribution, and reaction pathways beyond what an isolated atom can achieve[164]. DACs should not be conflated with the bimetallic Cu systems of Section "Bimetallic catalysts", which they superficially resemble in containing two metals: the difference is dispersion, not composition. A bimetallic Cu catalyst is an extended alloy whose active ensemble remains many contiguous atoms, whereas a DAC is an isolated, support-anchored pair acting as a discrete two-site unit. Thus, a Cu–Ag pair constitutes a DAC here only when atomically dispersed, not as an extended alloy surface.

Homonuclear DACs serve as a useful conceptual bridge between SACs and heteronuclear DACs: two identical adjacent metal centres introduce dual-site reactivity beyond SAC behaviour while avoiding the additional variable of heterometal compositional asymmetry[164]. The interaction between the two active sites further refines the local electronic structure and enhances catalytic performance. Zhao *et al.* demonstrated that the Fe_2N_6 DAC outperformed its FeN_4 SAC counterpart for CO formation by facilitating CO_2 activation and reducing the energy cost of CO desorption at the diatomic site[165]. Zhang *et al.* showed that charge transfer within the Pd_2 dimer promotes selective CO formation, with the diatomic character of the active site confirmed by X-ray absorption fine structure (XAFS) analysis[166].

The neighbouring dual site can also provide sufficient local space and cooperative binding to stabilise two adsorbates simultaneously, which is especially relevant for C–C coupling and C_{2+} product formation. Liu *et al.* identified FeFe@C_2N as the most active DAC for C_2H_4 production among a computationally screened set, with a CHE-derived limiting potential of U_L = -0.76 V, a thermodynamic estimate of the minimum overpotential that does not account for kinetic barriers along the C–C coupling pathway[167]. Ma *et al.* showed that O/OH co-adsorption at the bridge site of Co_2 and Ni_2 dimers destabilises the over-bound bridged-*CO intermediate, a configuration that typically blocks C_2 formation on DACs, thereby opening lower-energy coupling pathways[168].

Heteronuclear DACs introduce an additional compositional degree of freedom that enables a trade-off between activity, stability, and selectivity inaccessible to homonuclear systems[169]. The asymmetric coordination of heteronuclear sites allows the two metal centres to favour different intermediate binding modes, C-bound or O-bound, enabling *COOH, *CO, and *CHO binding to be tuned independently rather than being constrained by the scaling relations that limit single-metal and homonuclear surfaces. This asymmetry gives rise to a "division-of-labour" principle in which one metal centre specializes in CO_2 activation while the other stabilizes key intermediates: in the Ni–Fe DAC, for example, the Fe site preferentially activates CO_2 while the Ni site stabilizes *COOH[170], and one centre may act as a promoter while functioning as a spectator in the direct bond-making steps[171]. Computationally, heteronuclear DAC performance has been rationalised through descriptors including the *CO binding energy difference between the two metal sites, the degree of inter-metal charge transfer, and the asymmetry of the projected d-band density of states; these are quantities that connect naturally to the ML screening workflows described in Section "Machine learning regression models". Representative predictions of DACs and their experimental realisation are listed in Tables 3 and 4, respectively. Computational predictions for both homonuclear and heteronuclear DAC systems have been substantiated by experimental realisation. Zhao *et al.* demonstrated that a precisely synthesised homonuclear Fe_2N_6 DAC delivered higher CO FE than its FeN_4 SAC counterpart, attributing the improvement to facilitated CO_2 activation and reduced CO desorption energy at the diatomic site[165]. Zhang *et al.* reported a supported Pd_2 DAC in which charge transfer within the Pd–Pd dimer promoted selective CO formation[166]. For heteronuclear systems targeting C_{2+} products, Ren *et al.* demonstrated that isolated Ni–Fe diatomic sites embedded in nitrogen-doped carbon achieved selective CO_2 electroreduction, with operando XAS confirming retention of the diatomic active-site geometry under reaction conditions and synergistic binding between the two metal centres stabilising *COOH[170]. More recent work has extended DAC synthesis to metal–organic framework supports: Zhao *et al.* reported that a Cu–Sn hetero-bimetal MOF achieved selective electroreduction of CO_2 to ethanol via an asymmetric *CO–*OCH_2 coupling pathway[172], while Chen *et al.* showed that asymmetrically coordinated Cu dual-atom sites on doped carbon directed selectivity towards ethanol with suppressed competing pathways[173]. Collectively, these experimental results confirm that the cooperative reactivity predicted computationally for DAC systems is chemically realisable, and that the "division-of-labour" principle translates to measurable selectivity advantages under electrochemical conditions.

Table 3. Computational predictions for homonuclear and heteronuclear DACs targeting C_2 formation in eCO_2R

Active centre	Support	Coordination environment	Main product	RDS	Ref.
Fe–Fe	2D C_2N	N_2–N_2	C_2H_4	*CO–*COH coupling	[167]
Mn–Ni	g-C_3N_4	N_3–N_3	C_2H_5OH	*CO–*CHO coupling	[174]
Ti–Rh	Graphene	N_4–N_4	C_2H_5OH	Not reported	[175]
Co–Cu	2D C_2N	N_2–N_2	C_2H_4	*CO–*COH coupling	[167]
Cu–Cu	Graphene	NO_2–NO_2	C_2H_4	*CO–*COH coupling	[176]
Cu–Sn	MOF	N_4–N_2O_2	C_2H_5OH	*CO–*OCH_2 coupling	[172]
Cu–Cu	Doped carbon	N_2–NS	C_2H_5OH	*CHCOH → *CHCHOH	[173]

"Not reported" denotes a quantity applicable to the study type but not stated in the cited source. DACs: Dual-atom catalysts; eCO_2R: electrochemical CO_2 reduction; RDS: rate-determining step; MOF: metal–organic framework.

Table 4. Experimentally realised DACs for eCO_2R

Active centre	Support	Coordination environment	Main product	FE (%)	Potential (V *vs.* RHE)	Ref.
Fe–Fe	Doped carbon	N_3–N_3	CO	96	-0.6	[165]
Pd–Pd	Acetylene black	N_2O_2–N_2O_2	CO	98.2	-0.85	[166]
Ni–Fe	Nitrogenated carbon	N_3–N_3	CO	98	-0.7	[170]
Sn–Cu	MOF	N_2O_2–N_4	C_2H_5OH	56	-0.57	[172]
Cu–Cu	Carbon matrix	N_2–NS	C_2H_5OH	62.6	-0.8	[173]

Potentials are reported *vs.* RHE. DACs: Dual-atom catalysts; eCO_2R: electrochemical CO_2 reduction; FE: Faradaic efficiency; RHE: reversible hydrogen electrode; MOF: metal–organic framework.

Despite this progress, DACs present synthesis and characterisation challenges that are qualitatively distinct from those of SACs and that remain incompletely resolved. Achieving precise control over the metal–metal distance and coordination geometry of the diatomic site, parameters that are critical determinants of the cooperative binding effects described above, is considerably more demanding than anchoring isolated single atoms, because diatomic sites must be prevented from either separating into two independent SAC sites or aggregating into metal clusters under the reducing conditions of eCO_2R. Characterizing the true atomic structure of DAC active sites under operando conditions requires a combination of XAFS, scanning transmission electron microscopy (STEM), and ideally *in situ* SERS, since the diatomic geometry may evolve under applied potential in ways not captured by *ex situ* structural analysis, a reconstruction pathway that the GCMC and GC-DFT frameworks discussed in Section "Applied potential induced reconstruction and property change" are well positioned to model but that has not yet been systematically applied to DAC systems. Bridging this characterisation gap represents a concrete near-future priority: MLFF-generated structural ensembles for DAC active sites could be used to compute simulated XAFS spectra for direct comparison with operando measurements, providing a quantitative test of whether the computational active-site models correspond to the experimentally observed structures.

Overall, DACs extend the concept of atomically dispersed catalysis by introducing cooperative multi-centre reactivity. Experimental realisations across homonuclear and heteronuclear systems confirm that the adsorption and scaling limitations of conventional SACs can be overcome through rational diatomic site design. The operando structural evolution of these sites under electrochemical conditions, and its influence on product selectivity, is addressed in the context of potential-induced reconstruction and co-adsorption phenomena in Section "Operando evolution and co-adsorption".

The single-atom, dual-atom, and oxide-derived Cu results surveyed above rest on DFT of doped, heteroatom-coordinated, and partially oxidised surfaces, for which conventional DFT carries limitations

more acute than for clean metal slabs. First, exchange–correlation functional error in adsorption energies, of the order of 0.1-0.3 eV on transition-metal and M–N–C centres, is comparable to the free-energy differences that distinguish competing eCO_2R pathways, so that selectivity predictions can be qualitatively sensitive to the functional chosen[177,178]. Second, on doped and semiconducting supports such as g-C_3N_4 and N-doped carbon, computed adsorption energetics depend on the Fermi-level position and the net charge of the cell[179]; fixed-electron, fixed-cell DFT represents this dependence only approximately, and doping level, vacancy formation, protonation, and oxidative surface treatment each shift the Fermi level and therefore the computed binding energies of *COOH, *CO, and *CHO[180,181]. Third, the correlated 3d centres that dominate SAC and DAC chemistry (Fe, Co, Ni) and the partially oxidised Cu of oxide-derived catalysts are susceptible to self-interaction error, which corrupts d-state energetics and spin-state ordering unless a Hubbard-*U* correction (DFT + *U*) or a hybrid functional is applied[182-185]. These limitations are mitigated rather than eliminated: benchmarking adsorption energies against higher-level references, determining *U* non-empirically (for example by linear response) rather than fitting it, performing hybrid-functional spot checks on spin-state energetics, and adopting grand-canonical or Fermi-level-aware schemes that represent the support charge state explicitly (Section "Grand canonical and constant potential DFT") each reduce the corresponding error. For the doped semiconductor surfaces on which several of the cited SAC and DAC studies rest, the Fermi-level and surface-treatment dependence of the computed energetics is therefore a determinant of the predicted selectivity rather than a second-order correction, and reported adsorption energies should be interpreted with the functional, *U* value, and charge treatment in view.

OPERANDO EVOLUTION AND CO-ADSORPTION

Computational investigations of eCO_2R have long relied on static and idealised catalyst models, most notably low-index Cu(100) and Cu(111) surfaces. While such models have provided valuable mechanistic insight, they do not fully capture the structural evolution of catalysts under operating potential. Furthermore, solvent effects are commonly incorporated through implicit-solvent treatments that primarily account for energetic stabilisation but do not explicitly describe solvent–catalyst interactions. Consequently, important features such as the orientation of interfacial water, hydrogen-bonding networks, and the co-adsorption of H_2O or OH^- on reactive sites often remain unresolved. Methods such as GCMC, which sample adsorbate populations at fixed chemical potential, offer an improved route for describing potential-dependent surface coverages and electrolyte effects under operando conditions. Therefore, this section focuses on computational approaches that move beyond static surface models to capture catalyst restructuring, explicit interfacial interactions, and co-adsorption phenomena under realistic reaction conditions.

Applied potential induced reconstruction and property change

Simulating catalyst reconstruction and surface roughening under operando conditions remains one of the principal challenges in computational eCO_2R because the active surface can evolve substantially under applied potential and adsorbate coverage[186]. Using the coupled GCMC–EKMC framework described in Section "GCMC", Zhang *et al.* showed that Cu adatoms and small Cu clusters (principally Cu_4) migrate and aggregate at defect sites on the Cu(100) surface under applied cathodic potential[28], with the resulting Cu_4 clusters positioning adsorbed *CO between the first and second layers of interfacial water, an interfacial geometry that lowers the barrier for *CO activation and C–C coupling[30]. Cheng *et al.* demonstrated that simultaneous *CO and *H co-adsorption drives Cu surface roughening by weakening subsurface Cu–Cu bonds through adsorbate-induced charge redistribution, lowering the barrier for Cu atom migration and cluster formation[73]; the same reconstruction pathway was subsequently identified on Cu(111)[73]. Together, these results indicate that co-adsorption-driven roughening operates on both low-index Cu facets examined under the studied conditions, evidence consistent with a general roughening mechanism across Cu electrodes under eCO_2R conditions. Beyond structural reconstruction, the applied electrode potential substantially alters reaction energetics, surface coverages, and product selectivity. Alsunni *et al.* showed that

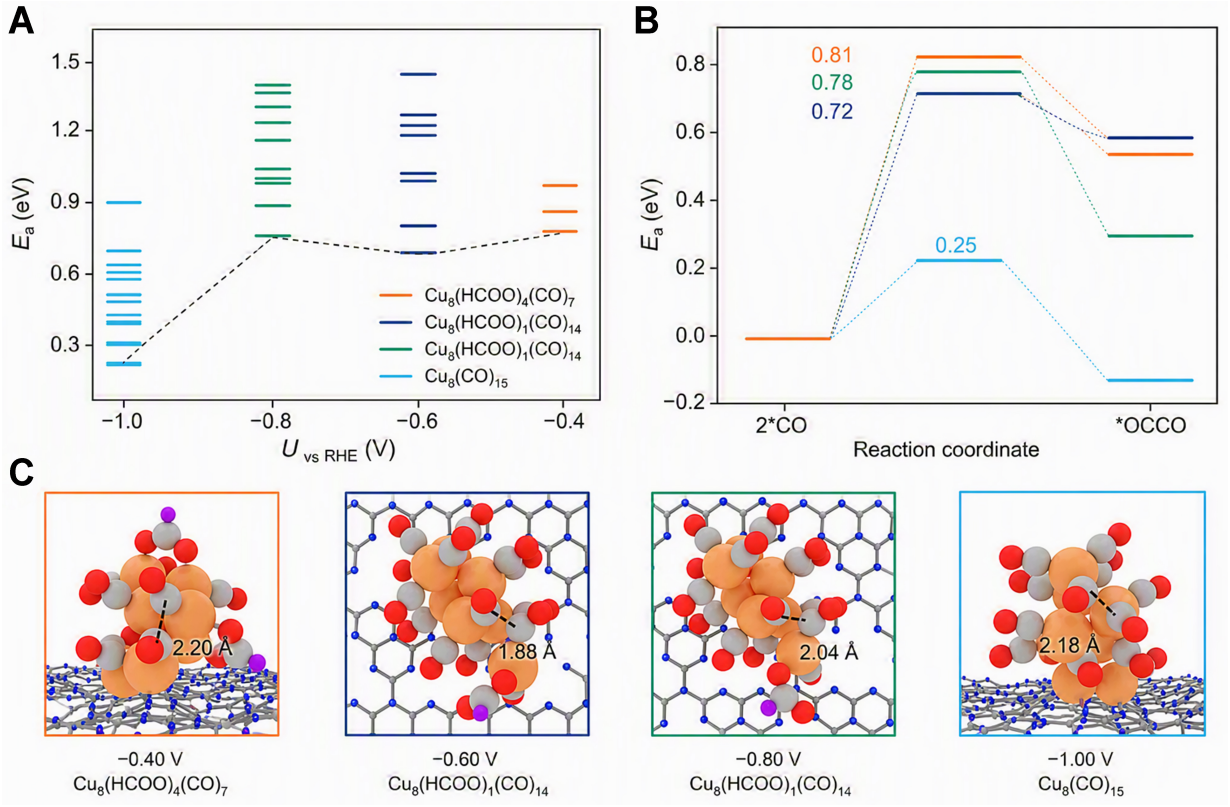


Figure 9. CO dimerisation on the most stable Cu_8 clusters at different potentials. (A) Distribution of all calculated CO dimerisation barriers on $Cu_8(HCOO)_4(CO)_7$ at -0.40 V, $Cu_8(HCOO)_1(CO)_{14}$ at -0.60 and -0.80 V, and $Cu_8(CO)_{15}$ at -1.00 V. Each line represents an individual CO dimerisation event; (B) Energy profiles of the lowest-barrier CO dimerisation pathways on the four clusters; (C) Transition-state structures correspond to the lowest-barrier CO dimerisation pathways. The bond distances between the two fragments at the transition states are indicated in Å. This figure reproduced with permission from Ref.[187], Copyright © 2026 American Chemical Society. RHE: Reversible hydrogen electrode.

adsorbate geometry is governed by the applied potential, and that the free energy of key intermediates responds non-linearly to applied potential, causing the preferred reaction pathway to switch between moderately and highly reducing conditions; for example, from *CO dimerisation at moderate overpotentials to *CO–*CHO coupling at more negative applied potentials (cf. Section "Grand canonical and constant potential DFT")[22]. Using a hybrid neural-network/GCMC approach, Zhu *et al.* systematically investigated the competition between *CO and *HCOO adsorption on Cu nanoclusters as a function of applied potential [Figure 9][187]: *HCOO adsorption, formed via a single proton–electron transfer step from CO_2, dominates the moderately reducing potential window, while *CO adsorption, requiring two proton–electron transfer steps, becomes thermodynamically favoured at more negative potentials. The higher *CO surface coverage at more negative potentials reduces the mean distance between adjacent *CO adsorbates, increasing the density of C–C coupling sites and lowering the activation barrier for *CO dimerisation. Potential-dependent effects are not confined to extended metal surfaces. At molecularly defined and atomically dispersed centres, applied potential modifies the formal oxidation and spin state of the metal, established for CoN_4 sites, where interfacial charge drives an electrostatic spin crossover, and for cobalt porphyrins, where the accessible redox state governs the reduction mechanism[188,189], redistributing electron density at the metal site and thereby shifting intermediate binding energies and product selectivity.

Co-adsorption of ligands

Beyond the support and coordination environment effects discussed in the Sections "Copper-based catalysts" and "Atomically dispersed catalysts", catalytic performance under operando conditions is substantially

influenced by co-adsorption of spectator species. These are molecular and ionic entities present at the interface that are not direct reaction intermediates but modify intermediate stabilisation, the local electrostatic field, and the accessibility of reactants and proton donors to active sites.

Because water is the primary proton source in aqueous electrolytes, proton-coupled electron-transfer processes near the cathode generate OH^- locally, leading to high interfacial OH^- concentrations and a significant probability of OH^- co-adsorption at active sites. Sun *et al.* showed that *OH surface coverage is directly correlated with CH_4/C_2H_4 selectivity on Cu surfaces, with higher *OH coverage favouring C_2H_4 formation[190]. Further computational studies show that OH^- co-adsorption reduces the *CO–*CO separation distance, extends the *CO surface residence time through electrostatic stabilisation of the adsorbed state, and lowers the C–C coupling barrier[191-193]. The local electrostatic field generated by co-adsorbed OH^- contributes independently to these effects by polarising adsorbed *CO and *CHO dipoles, a mechanism captured by GC-DFT but absent from CHE-based analyses that treat the interface as field-free.

In addition to inorganic spectator species, organic additives enhance PCET, tune intermediate binding strength, and steer selectivity toward specific products. For Ag-based catalysts, which are already selective for CO production, carefully designed ligand, dihexadecyldimethylammonium bromide (abbreviated 2-C16) co-adsorption increases the FE for CO to nearly 100%[194]. On Cu-based catalysts, Xu *et al.* showed that co-adsorbed functional groups exert distinct and group-specific effects on eCO_2R selectivity: NH_3^+- and SO_3H-decorated Cu surfaces promote CH_4 formation by stabilising *CO, *CHO, and $*OCH_3$[195]. Qiu *et al.* demonstrated the positive role of the NH_3^+ group for CH_4 formation and the concurrent suppression of HER[196].

C_{2+} selectivity can also be regulated through tailored ligand modification. Glycine-modified Cu surfaces enhance C_{2+} selectivity via *CO–*CHO coupling, driven by charge transfer between glycine and C_1 intermediates[197]. A tricomponent copolymer-modified Cu surface achieved 77% selectivity toward C_{2+} products; MD simulations showed that this improvement arises from enhanced reactant access through the porous interfacial structure and from modification of the local electrostatic field[198].

Co-adsorbed spectator species and organic ligands therefore play an active mechanistic role in tuning intermediate stabilisation, interfacial electrostatics, and product selectivity in eCO_2R, effects that operate in parallel with the influence of bulk electrolyte composition.

Electrolyte cation effects

Alkali metal cations modify the electrochemical double layer, alter the local electric field at the catalyst surface, and, in some cases, directly participate in CO_2 activation, making cation identity and concentration experimentally accessible variables for controlling eCO_2R activity and selectivity.

Two mechanistic interpretations of cation effects have emerged in the computational literature, differing in whether cations act through direct coordination of CO_2 intermediates or through modification of the interfacial electric field. The first proposes that cations directly coordinate CO_2 at the interface and contribute to the first electron transfer step. Qin *et al.* established that cations switch the operative electron-transfer mechanism: in a cation-free electrolyte, CO_2 reduction proceeds through an outer-sphere electron transfer (OS-ET) at the electrode, whereas alkali metal cations raise the OS-ET barrier and open a competing inner-sphere channel[19]. Using slow-growth sampling combined with ab initio molecular dynamics (SG-AIMD) on an explicit Au(110)–water interface at U = -1.17 V *vs.* RHE, Qin *et al.* showed that, in the absence of interfacial cations, CO_2 activation cannot proceed: the free energy along the adsorption coordinate rises monotonically, and no transition state is located[19,33]. Introducing two K^+ ions into the inner-Helmholtz

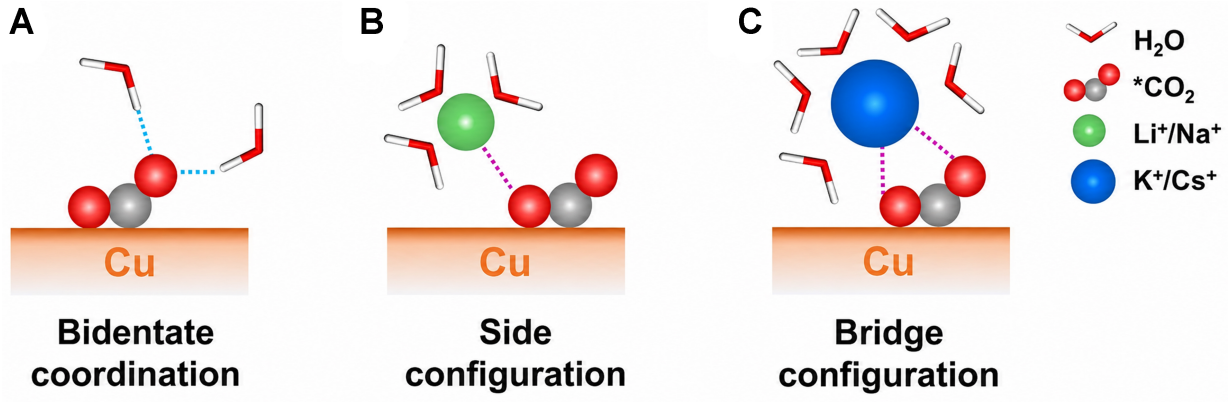


Figure 10. Local interactions between $*CO_2$ at the Cu(100) surface and the surrounding environment: (A) Schematic of the bidentate adsorption of $*CO_2$ at Cu surface in an explicit solvent with C and one of the O atoms coordinating with Cu, and the other O atom forming hydrogen bonds (light blue dashed lines) with surrounding water; (B) Schematic of the side configuration of Li^+ or Na^+ coordinated with only one O atom of $*CO_2$ (magenta dashed line); (C) Schematic of the bridge configuration of K^+ or Cs^+ coordinated with two O atoms of $*CO_2$. (A-C) Reproduced from Ref.[199] under the terms of the Creative Commons CC-BY 4.0 licence.

region opens an inner-sphere electron-transfer (IS-ET) channel in which the cations coordinate the bent $CO_2^{\delta-}$ intermediate through short-range K–O interactions, yielding a constant-potential free-energy barrier of ΔG_b = 0.66 eV for the rate-determining $CO_2(aq) \rightarrow *CO_2$ step. Under the same conditions, the rate-determining Volmer step of HER carries a markedly higher barrier of ΔG_b = 1.27 eV, so that the K^+ accumulation at the inner-Helmholtz plane simultaneously promotes CO_2 activation and suppresses water dissociation at the same applied potential, a kinetic blockage effect attributable to disruption of the interfacial hydrogen-bond network at high near-surface cation coverage. Zhang *et al.* extended this picture through systematic DFT calculations of cation–CO_2 interactions across the alkali series [Figure 10], showing that smaller cations (Li^+, Na^+) coordinate only one oxygen atom and activate CO_2 weakly, while larger cations (K^+, Cs^+) simultaneously coordinate both oxygen atoms, producing strong activation; larger cations also suppress interfacial proton adsorption, providing a route to inhibit parasitic HER[199]. Yang and co-workers showed through AIMD simulations that smaller cations are characterised by a rigid hydration shell, causing water molecules to intercalate between the cation and C_1 intermediates and favouring C_1 products; larger cations present a loose hydration shell that creates a hydrophobic microenvironment near *CO intermediates, reducing local proton availability, suppressing *CHO formation, and promoting *CO–*CO dimerisation and C_{2+} product formation[200].

A second interpretation proposes that cations influence eCO_2R primarily through modification of the interfacial electric field rather than through direct coordination of intermediates. Ringe *et al.* showed, using a modified Poisson–Boltzmann continuum model combined with DFT, that cation-induced interfacial electric fields stabilise dipolar intermediates and transition states, including the bent $CO_2^{\delta-}$ species and the *CO–*CO coupling transition state, through field–dipole interactions, accounting quantitatively for the experimentally observed cation-size dependence of CO production on Ag and C_{2+} formation on Cu[201]. Gu *et al.* provided further support for this interpretation, showing that physiosorbed hydrated cations near the cathode generate a local electric field that stabilises key intermediates and promotes eCO_2R[202].

These two interpretations are not mutually exclusive. A reconciling framework distinguishes inner-Helmholtz-plane effects, where cations can directly coordinate CO_2 and stabilise bent intermediates through short-range Coulomb interactions, from outer-Helmholtz-plane effects, where the accumulated cation layer generates the interfacial electric field that stabilises dipolar transition states. Both mechanisms operate simultaneously, with their relative importance depending on cation size, applied potential, and surface

charge density. Together, cations reshape the local electric double layer, modify proton availability, modulate HER competition, and in some cases directly stabilise reactive interfacial intermediates. Cation identity and concentration therefore constitute experimentally accessible tools for tuning both activity and selectivity in eCO_2R.

Electrolyte pH effects

Electrolyte pH governs proton availability at the cathode and thereby directly determines the competition between eCO_2R and HER, as well as the distribution of products formed along reduction pathways that diverge at proton-consuming steps.

Because proton-consuming reduction reactions occur preferentially at the cathode, the local pH near the electrode surface rises by several pH units relative to the bulk electrolyte under typical eCO_2R operating conditions. Conventionally, eCO_2R has been performed in near-neutral to alkaline CO_2-saturated bicarbonate electrolytes to suppress HER[203]. Within the pH range that supports eCO_2R, product selectivity correlates strongly with operational pH. Liu *et al.* showed, using CHE-based DFT calculations on Cu(211), that higher pH strongly promotes C_{2+} product formation while lower pH facilitates the sequential reduction of C_1 intermediates to C_1 products[204]. Kastlunger *et al.* examined the pH dependence of C_2 product selectivity using GC-DFT calculations and showed that the first proton–electron transfer to O atoms of C_2 intermediates produces C_2H_4, which is kinetically preferred owing to the greater accessibility of oxygen lone pairs to proton transfer, while the first reduction at the C atom produces C_2H_5OH, which is thermodynamically favoured but kinetically inhibited under conditions of high proton availability[205]. Under strongly alkaline conditions, where proton activity is low, thermodynamically favoured C-protonation becomes dominant, a result consistent with experimental observations that C_2H_5OH yield increases substantially at pH > 13.

eCO_2R under strongly acidic conditions has received comparatively less computational attention, owing to reduced catalyst stability and strong HER competition[206]. Recent efforts have turned to acidic eCO_2R, motivated by the need to avoid the parasitic conversion of CO_2 to carbonate and bicarbonate in alkaline electrolytes, which can consume up to 70% of the CO_2 feed, and by the enhanced ionic conductivity of acidic media. High proton concentrations substantially enhance selectivity toward hydrocarbons such as CH_4 and C_2H_4, but suppressing parasitic HER becomes the central challenge. Three strategies have been proposed: first, the local pH near the cathode rises during eCO_2R as protons are consumed, so that reduction effectively occurs within a neutral or alkaline interfacial microenvironment even when the bulk electrolyte is acidic[207,208]; second, introducing larger cations such as K^+ generates a hydrophobic local environment and suppresses proton adsorption at active sites[209,210]; third, raising intermediate surface coverage and weakening proton binding at active sites further reduces HER competition[193,211]. The eCO_2R in acidic bulk electrolytes is therefore best understood as reduction occurring within a locally engineered neutral or alkaline interfacial microenvironment, while the acidic bulk conditions serve to minimise carbonate losses and enhance electrolyte conductivity.

The effect of pH in eCO_2R is not merely a bulk electrolyte property but a coupled interfacial phenomenon involving proton availability, the local reaction microenvironment, and competition with HER. The operando complexity documented across he catalyst and operando sections above (dynamic catalyst restructuring, co-adsorption effects, and cation- and pH-dependent interfacial behaviour) highlights a fundamental tension between the idealised models used in most computational studies and the conditions that prevail in real electrochemical systems. Section "Challenges, limitations, and near-future directions of eCO_2R" examines the methodological limitations that underlie this tension and identifies the computational advances needed to resolve it.

CHALLENGES, LIMITATIONS, AND NEAR-FUTURE DIRECTIONS OF eCO_2R

The preceding sections have identified a set of recurrent computational challenges that limit the fidelity and predictive power of theoretical eCO_2R studies: the gap between static slab models and dynamically reconstructed catalysts, the scale mismatch between atomistic simulations and device-level operation, the inadequate treatment of explicit solvent and electrolyte effects, and the transferability constraints of current ML approaches. This section examines each limitation in turn and identifies recent methodological advances such as constant-potential dynamics, multiscale modelling, solvation theory, and data-driven catalyst design that are most likely to close the gap between computational prediction and experimental observation.

Beyond the CHE

As established in Section "Conventional fixed-electrons DFT", the CHE model, while computationally efficient and valuable for thermodynamic screening, treats each elementary step as a concerted PCET, applies a strictly linear $-eU$ potential correction, and cannot represent the non-linear response of intermediate geometries, binding energies, or surface charge to applied potential[16]. In eCO_2R, these approximations become particularly consequential because the most mechanistically important steps, CO_2 activation, *CO–*CO coupling, and potential-dependent surface reconstruction, are precisely those where CHE and GC-DFT predictions diverge most substantially, and where the choice of computational model determines not just quantitative accuracy but qualitative mechanistic conclusions. Mechanistically accurate descriptions of eCO_2R therefore require methods that explicitly represent electrode potential, kinetic barriers, and the electrolyte environment.

To address these limitations, grand canonical/constant-potential DFT is a widely used approach to treat electrode potential explicitly. Governed by the constant chemical potential, the number of electrons in a specific system can be varied, which is more realistic than CHE for potential-dependent charge redistribution, double-layer response, and reactions where the applied bias changes the interfacial state[20].

GC-DFT addresses the potential-representation limitation of CHE by treating the electrode as an open electronic system at fixed electron chemical potential (Section "Grand canonical and constant potential DFT")[20]. A productive near-future direction is the systematic integration of constant-potential transition-state methods such as NEB[212] and dimer[213] searches within GC-DFT workflows as a standard intermediate tier between CHE-based thermodynamics and full AIMD simulations. Such workflows can locate saddle points and compute activation barriers at a specified electrode potential, enabling assessment of whether thermodynamically favoured pathways identified by CHE remain kinetically accessible under operating conditions. This integration is particularly important for steps where CHE and GC-DFT predictions diverge qualitatively, such as *CO dimerisation at moderately reducing potentials *vs.* *CO–*CHO coupling at more negative potentials (Section "Grand canonical and constant potential DFT"), and for potential-dependent reconstruction pathways on Cu(100) (Section "Applied potential induced reconstruction and property change"). Coupling constant-potential barrier calculations with microkinetic models would enable genuinely potential-dependent rate predictions, currently unavailable because existing eCO_2R microkinetic models rely on CHE-derived thermodynamics as inputs and would provide a direct computational route to Tafel slopes, partial current densities, and selectivity maps as functions of applied potential, enabling rigorous comparison with experimental polarisation curves.

A parallel limitation is the treatment of solvation. Most eCO_2R DFT studies employ linear continuum solvation models (PCM, VASPsol) that cannot represent the non-linear dielectric response near highly charged interfaces, the specific orientation of interfacial water molecules, or the co-structure of ions and solvent at the inner Helmholtz plane, all of which contribute measurably to adsorption energies and barrier heights in the operando studies reviewed in Section "Operando evolution and co-adsorption". The

development of non-linear implicit solvation models that incorporate field-dependent dielectric saturation, and their systematic validation against AIMD-derived interfacial properties, represents a concrete methodological priority that would substantially improve the accuracy of GC-DFT and CHE calculations without the prohibitive cost of fully explicit solvent treatment.

Bridging the atomistic-to-device scale gap

A further persistent challenge in eCO_2R modelling is the scale mismatch between atomistic simulation and device-level experiment. Most atomistic simulations rely on small, periodic, and idealised interfacial models at the nanometre scale and trajectories spanning picoseconds to nanoseconds, whereas experiments probe catalytic performance across electrode areas of cm^2, over timescales of hours to days, and under mass-transport conditions (CO_2 diffusion to the electrode surface, local pH gradient formation, and product removal) determined by electrolyte flow rates and cell geometry. This represents a span of roughly six orders of magnitude in both length and time, and descriptors or mechanisms derived from atomistic models under idealised conditions cannot in general be transferred to device-level performance without accounting for the intervening scales of surface coverage, mass transport, and cell geometry.

Recent advances at the atomistic tier are progressively narrowing this gap. Constant-potential GC-DFT provides electrochemically faithful energetics; hybrid explicit/implicit solvation models improve the description of the interfacial dielectric environment; and MLFFs extend accessible system sizes and timescales to scales previously reachable only by classical empirical potentials. A critical prerequisite for integrating these advances into a multiscale workflow is the development of constant-potential MLFFs. These are force fields trained at fixed electrode potential rather than fixed electron count, so that MD trajectories feeding into higher-tier models correctly represent potential-dependent interfacial structure and barrier heights (Section "Machine learning forcefields").

The most direct near-term route to closing the scale gap is a three-tier multiscale workflow in which MLFF-driven MD provides an atomistic-resolved description of the catalyst–electrolyte interface, microkinetic modelling propagates elementary-step rate constants to steady-state turnover frequencies, and CFD accounts for mass transport, local concentration gradients, and pH profiles across the full electrolyser geometry. Although the individual tiers, microkinetic modelling and continuum transport, are each established (Section "Microkinetics, transport, and interfacial thermodynamics"), their systematic coupling, and particularly the transfer of potential-dependent rate constants from the atomistic tier to the microkinetic tier, remains an open challenge. A further priority is the development of standardised interfaces between tiers, so that atomistic descriptors computed for a given catalyst can be propagated to reactor-level predictions without system-specific reimplementation. A prerequisite for reliable multiscale workflows is also the standardisation of the atomistic inputs that feed into them: the absence of community-curated benchmark datasets for eCO_2R adsorption energies and barriers, across catalyst families, DFT functionals, and solvation treatments, means that microkinetic models built from inputs from different studies are not directly comparable. Development of such datasets, analogous to the OC20 and OC22 benchmarks for heterogeneous catalysis[60,61], represents a foundational data infrastructure priority for the field.

Treatment of solvent effects

At present, solvent effects in eCO_2R are treated primarily with implicit continuum models such as VASPsol[214] because they are computationally efficient and compatible with GC-DFT, making them the default approach for electrochemical interface simulations in the eCO_2R literature. Their principal limitation is that the electrolyte is represented as a structureless medium characterised only by its bulk dielectric constant and ionic screening length, leaving atomistic solvent structure, hydrogen-bond fluctuations, proton shuttling, and specific ion or water adsorption without explicit representation. The widely used linear

continuum models cannot reproduce the non-linear dielectric saturation and ion-specific response that govern interfacial charging and double-layer capacitance under eCO_2R conditions, and they treat the electrode–solvent boundary as a sharp dielectric discontinuity that excludes charge transfer, exchange interactions, and chemisorption at the first solvent layer[215-217]. For eCO_2R specifically, this last limitation is consequential for intermediates such as *COOH, whose stabilisation energy depends on orientation-specific hydrogen-bonding interactions with the first water layer that can contribute 0.2-0.4 eV to the adsorption free energy[215], a contribution that implicit models miss entirely and that propagates into errors in CHE-derived limiting potential estimates. These limitations are most severe precisely where they matter most for eCO_2R: at the highly charged, structured interfacial environment where non-linear dielectric saturation, specific water orientation, and proton shuttling via the Grotthuss mechanism collectively determine adsorption energetics and barrier heights.

Three near-future developments are likely to substantially improve the treatment of solvent effects. First, non-linear and non-local continuum models, including extensions of the VASPsol framework toward field-dependent dielectric response and the implicit electrolyte model of Islam *et al.*, address the failure of standard linear models to capture non-linear dielectric saturation and ion-specific response at charged interfaces[217]; systematic validation of these models against explicit-solvent AIMD benchmarks for eCO_2R-relevant interfaces, particularly Cu/water and Ag/water systems where MLFF-based trajectories are now accessible[31,52], is needed to establish their reliability across operating conditions. Second, hybrid explicit-implicit schemes, in which the first one or two solvent layers are treated explicitly at the DFT or MLFF level while the bulk solvent is represented by a continuum, offer a balance between accuracy and computational cost; such schemes have been demonstrated for related electrochemical reactions but remain underexplored for eCO_2R. Third, the interfacial water structures, hydrogen-bond networks, and dielectric response functions sampled in MLFF-driven trajectories (Section "Machine learning forcefields") can serve as physically motivated reference data to reparametrize next-generation implicit models. Specifically, this data can optimise cavity construction, dielectric permittivity profiles, and ionic screening functions. These quantities are currently fitted to bulk experimental data, leaving them poorly constrained for the highly charged interfacial environments relevant to eCO_2R. Addressing this establishes a parametrisation loop between dynamic and continuum descriptions of the interface, substantially improving GC-DFT accuracy without requiring fully explicit solvent treatment.

Machine learning for eCO_2R

Machine learning represents a promising route for accelerating electrocatalysis simulations, but its robustness, transferability, and generalisation are still limited. For MLFFs, transferability outside the training domain remains challenging, especially when nonlocal interactions, rare reactive configurations, or chemically distinct environments are not adequately represented in the reference set[45]. More generally, the predictive quality of ML models is still strongly constrained by the quantity, diversity, and consistency of available data. In catalysis, many datasets remain small, biased, or non-standardised, while generating reliable labels from DFT, AIMD, or experiments is itself computationally and experimentally expensive[218,219]. Another major limitation lies in descriptor engineering: hand-crafted descriptors still exert substantial control over model quality, poor feature choices can constrain performance at an early stage, and a universal descriptor framework for catalytic prediction has not yet been established[220]. Consequently, model development often remains iterative and system-specific rather than broadly transferable. Recent progress in active learning, learned representations, and data-efficient ML potentials is promising, but these challenges remain active areas of development.

Four near-future directions stand out as having the greatest potential to advance ML-driven eCO_2R research. First, constant-potential MLFFs[49] represent a critical methodological advance: by training force fields at

fixed electrode potential rather than at zero charge, they can capture the potential-dependent reorganisation of the double layer and the associated changes in reaction barriers identified in Sections "Applied potential induced reconstruction and property change", "Co-adsorption of ligands", and "Electrolyte cation effects", without the prohibitive cost of GC-DFT MD. Second, the development of community-curated, standardised benchmark datasets for eCO_2R, analogous to the OC20 and OC22 datasets established for heterogeneous catalysis, would address the data scarcity and inconsistency that currently constrain ML model transferability; such datasets should include not only adsorption energies but also activation barriers, explicit-solvent configurations, and operando structural snapshots. Third, uncertainty quantification (UQ) should become a standard component of ML model outputs in eCO_2R, so that predictions used to prioritise experimental synthesis efforts carry explicit confidence intervals; Bayesian ensemble methods and conformal prediction are practical routes to UQ without prohibitive retraining costs. Fourth, inverse design workflows, in which generative models propose catalyst structures optimised for a target property and active learning loops iteratively refine the training set, have demonstrated early promise for eCO_2R catalyst discovery[221] and represent the most direct path from data-driven screening to experimental realisation.

Bridging computation and experiment

A cross-cutting challenge that transcends the individual methodological limitations discussed in limitations discussed above in this section is the absence of systematic workflows for integrating computational predictions with operando experimental characterisation data. The classes of catalyst reviewed above are routinely characterised by operando X-ray absorption spectroscopy (XAS), SERS, and *in situ* transmission electron microscopy (TEM), yet these techniques yield ensemble-averaged or spatially resolved structural information that is rarely used as a direct constraint on computational models. This disconnect means that theoretical predictions of active-site geometries, oxidation states, and intermediate coverages are typically validated only indirectly through comparison with product distributions, rather than through structural observables measured under reaction conditions.

A productive direction is the development of computation-experiment feedback loops in which operando spectroscopic signatures such as XAS edge positions, EXAFS coordination shells, and Raman band positions of adsorbed *CO and *OH are used to discriminate between competing structural models generated by DFT, GCMC, or MLFF simulations. For single-atom and dual-atom catalysts (Section "Atomically dispersed catalysts: single-atom and dual-atom sites"), where the active site geometry is directly accessible by XAS, such feedback is particularly tractable: the approach demonstrated by Martini *et al.*[114], combining operando XAS with ML analysis to track active-site evolution in SACs, represents an early example of this strategy and points toward a broader framework applicable across catalyst classes. For amorphous Cu-based catalysts (Section "Amorphous catalysts"), where the absence of long-range order makes conventional crystallographic validation impossible, MLFF-generated structural ensembles could be used to compute simulated XAS or pair distribution function (PDF) spectra for direct comparison with experiment, providing a quantitative measure of model fidelity.

Beyond structural validation, UQ in ML model predictions should be informed to experimental collaborators in a form that directly informs synthesis prioritisation: identifying not the single best-predicted catalyst but the region of compositional and structural space where model uncertainty is lowest and predicted performance is highest. Establishing shared data standards and open workflows for computation-experiment integration represents one of the most impactful near-future investments the eCO_2R community can make.

CONCLUSIONS AND OUTLOOK

The computational study of eCO_2R has matured from thermodynamic screening of idealised crystalline surfaces into a multiscale discipline that aspires to describe catalysts as they exist under operating conditions. The recurring theme of this review is that the central difficulty in the field is not any single missing capability

but a systematic mismatch: the models that are most tractable are also the most idealised, while the catalysts that are most active are disordered, dynamically reconstructing, and inseparable from their electrolyte environment. Each of the three themes surveyed here is a facet of that same tension.

The methodological hierarchy of Section "Computational methods for eCO_2R" is, in effect, a sequence of trade-offs between computational cost and fidelity to operating conditions. The CHE and descriptor-based screening remain indispensable for rapid exploration of trends, but their idealisations, namely concerted proton–electron transfer, a linear potential correction, and a static surface, are precisely the assumptions that break down for the mechanistically decisive steps of eCO_2R. Grand-canonical and constant-potential DFT, GCMC, AIMD, and MLFFs each relax one or more of these idealisations, at correspondingly higher cost, and the central methodological task is no longer to identify a single best method but to match each method to the physical question being asked. The catalyst classes of Sections "Copper-based catalysts" and "Atomically dispersed catalysts: single-atom and dual-atom sites" sharpen the same point. Copper-based materials, whether high-index, nanostructured, amorphous, or bimetallic, derive their activity from undercoordinated and disordered sites that the crystalline slab does not represent, while atomically dispersed single- and dual-atom catalysts concentrate reactivity at sites whose coordination environment and support interactions govern selectivity. In both classes, the structures that matter are those that emerge under reaction conditions. The operando phenomena of Section "Operando evolution and co-adsorption", namely potential- and adsorbate-driven reconstruction, spectator and ligand co-adsorption, cation effects, and local-pH gradients, are the direct experimental manifestation of this gap, and the studies reviewed there show consistently that a static, gas-phase-like picture of the interface is insufficient to predict either activity or selectivity.

The challenges set out in Section "Challenges, limitations, and near-future directions of eCO_2R" follow from this diagnosis, and they are not of equal priority. Two stand out as the most consequential because they would unblock the others. The first is the development of constant-potential MLFFs, which attack the scale gap and the potential-representation problem simultaneously: by reproducing near-DFT accuracy at fixed electrode potential over the length and time scales on which reconstruction and double-layer reorganisation actually occur, they would bring the most realistic description of the interface within routine computational reach. The second is the construction of community-curated, standardised benchmark datasets for eCO_2R, analogous to those that have driven progress in heterogeneous catalysis more broadly. Because the transferability of every data-driven method depends on the quantity, diversity, and internal consistency of its training data, and because the underlying DFT reference errors are comparable to the energy differences that determine selectivity, a shared and consistently computed dataset, encompassing activation barriers, explicit-solvent configurations, and operando structural snapshots, is a prerequisite rather than an incremental improvement. Beyond these, the development of non-linear implicit solvation models validated against explicit dynamics, the assembly of genuinely multiscale workflows that propagate constant-potential energetics through microkinetic and continuum-transport models to device-relevant predictions, and the systematic integration of computation with operando characterisation each address a distinct and necessary part of the same problem.

Taken together, these directions describe a field in transition from the description of idealised models towards the modelling of catalysts under operation. None of the outstanding problems is likely to be resolved by a single method in isolation; progress will instead come from coordinated advances across the methodological hierarchy and from a closer coupling between computation and experiment than has so far been the norm. The developments of the past several years, in potential-dependent dynamics, ML interatomic potentials, and atomically dispersed catalyst design, make this a realistic prospect rather than an aspiration, and they indicate that the most informative computational eCO_2R studies of the coming years will

be those that treat the idealised model not as the object of study but as the starting point from which the operating catalyst is reconstructed.

DECLARATIONS

Authors' contributions

Conceptualisation, writing - original draft (Sections "Computational methods for eCO_2R: from thermodynamic frameworks to data-driven approaches", "Copper-based catalysts", "Atomically dispersed catalysts: single-atom and dual-atom sites", "Operando evolution and co-adsorption", and "Challenges, limitations, and near-future directions of eCO_2R"), visualisation, writing - review and editing, validation: Lin, W.

Writing - original draft (Sections "Introduction" and "Amorphous catalysts"), visualisation, validation: Muthuperiyanayagam, A.

Conceptualisation, writing - review and editing, supervision, project administration, funding acquisition, resources, validation: Di Tommaso, D.

Availability of data and materials

Not applicable.

AI and AI-assisted tools statement

Claude Sonnet 4.6 (Anthropic, released 17 February 2026) was used for language editing. All AI-assisted outputs were reviewed and verified by the authors, who take full responsibility for the accuracy, integrity, and scientific content of the manuscript. AI assistance did not contribute to study design, data analysis, or interpretation.

Financial support and sponsorship

Lin, W. thanks the China Scholarship Council (202206310040) for financial support. Di Tommaso, D. thanks the Leverhulme Trust (RPG-2023-239) for resources supporting projects advancing materials characterisation by computational means.

Conflicts of interest

All authors declared that there are no conflicts of interest.

Ethical approval and consent to participate

Not applicable.

Consent for publication

Not applicable.

Copyright

© The Author(s) 2026.

REFERENCES

1. IPCC. Climate Change 2023: Synthesis Report. A report of the intergovernmental panel on climate change. https://www.ipcc.ch/report/ar6/syr/downloads/report/IPCC_AR6_SYR_FullVolume.pdf. (accessed 2026-09-30).
2. Nagireddi, S.; Agarwal, J. R.; Vedapuri, D. Carbon dioxide capture, utilization, and sequestration: current status, challenges, and future prospects for global decarbonization. *ACS. Eng. Au.* **2024**, *4*, 22-48. DOI
3. Nitopi, S.; Bertheussen, E.; Scott, S. B.; et al. Progress and perspectives of electrochemical CO_2 reduction on copper in aqueous electrolyte. *Chem. Rev.* **2019**, *119*, 7610-72. DOI PubMed
4. Bagger, A.; Ju, W.; Varela, A. S.; Strasser, P.; Rossmeisl, J. Electrochemical CO_2 reduction: a classification problem. *Chemphyschem* **2017**, *18*, 3266-73. DOI PubMed
5. Hori, Y.; Kikuchi, K.; Suzuki, S. Production of CO and CH_4 in electrochemical reduction of CO_2 at metal electrodes in aqueous hydrogencarbonate solution. *Chem. Lett.* **1985**, *14*, 1695-8. DOI

6. Garza, A. J.; Bell, A. T.; Head-Gordon, M. Mechanism of CO_2 reduction at copper surfaces: pathways to C_2 products. *ACS. Catal.* **2018**, *8*, 1490-9. DOI
7. Peterson, A. A.; Nørskov, J. K. Activity descriptors for CO_2 electroreduction to methane on transition-metal catalysts. *J. Phys. Chem. Lett.* **2012**, *3*, 251-8. DOI
8. Huo, C.; Cao, X.; Ye, Z.; Li, Y.; Lu, T. Hierarchical bimetallic electrocatalyst with amorphous SnO layer for highly efficient electroreduction of CO_2. *ChemCatChem* **2021**, *13*, 4931-6. DOI
9. Calle-Vallejo, F.; Koper, M. T. Theoretical considerations on the electroreduction of CO to C2 species on Cu(100) electrodes. *Angew. Chem. Int. Ed. Engl.* **2013**, *52*, 7282-5. DOI PubMed
10. Liu, C.; Hedström, S.; Stenlid, J. H.; Pettersson, L. G. M. Amorphous, periodic model of a copper electrocatalyst with subsurface oxygen for enhanced CO coverage and dimerization. *J. Phys. Chem. C.* **2019**, *123*, 4961-8. DOI
11. Dattila, F.; Seemakurthi, R. R.; Zhou, Y.; López, N. Modeling operando electrochemical CO_2 reduction. *Chem. Rev.* **2022**, *122*, 11085-130. DOI PubMed
12. Re Fiorentin, M.; Bianchi, M. G.; Christiansen, M. A. H.; et al. Methodological frameworks for computational electrocatalysis: from theory to practice. *Small. Methods.* **2026**, *10*, e01542. DOI PubMed PMC
13. Govindarajan, N.; Kastlunger, G.; Gauthier, J. A.; et al. The intricacies of computational electrochemistry. *ACS. Energy. Lett.* **2025**, *10*, 4277-88. DOI PubMed PMC
14. Li, Y.; Sun, Y.; Yu, M. Strategies for improving product selectivity in electrocatalytic carbon dioxide reduction using copper-based catalysts. *Adv. Funct. Mater.* **2024**, *34*, 2410186. DOI
15. Wang, Z.; Zhou, Y.; Qiu, P.; et al. Advanced catalyst design and reactor configuration upgrade in electrochemical carbon dioxide conversion. *Adv. Mater.* **2023**, *35*, e2303052. DOI PubMed
16. Nørskov, J. K.; Rossmeisl, J.; Logadottir, A.; et al. Origin of the overpotential for oxygen reduction at a fuel-cell cathode. *J. Phys. Chem. B.* **2004**, *108*, 17886-92. DOI
17. Chan, K. A few basic concepts in electrochemical carbon dioxide reduction. *Nat. Commun.* **2020**, *11*, 5954. DOI PubMed PMC
18. Kastlunger, G.; Wang, L.; Govindarajan, N.; et al. Using pH dependence to understand mechanisms in electrochemical CO reduction. *ACS. Catal.* **2022**, *12*, 4344-57. DOI
19. Qin, X.; Hansen, H. A.; Honkala, K.; Melander, M. M. Cation-induced changes in the inner- and outer-sphere mechanisms of electrocatalytic CO_2 reduction. *Nat. Commun.* **2023**, *14*, 7607. DOI PubMed PMC
20. Melander, M. M.; Wu, T.; Weckman, T.; Honkala, K. Constant inner potential DFT for modelling electrochemical systems under constant potential and bias. *npj. Comput. Mater.* **2024**, *10*, 1184. DOI
21. Brimley, P.; Almajed, H.; Alsunni, Y.; et al. Electrochemical CO_2 reduction over metal-/nitrogen-doped graphene single-atom catalysts modeled using the grand-canonical density functional theory. *ACS. Catal.* **2022**, *12*, 10161-71. DOI
22. Alsunni, Y. A.; Alherz, A. W.; Musgrave, C. B. Electrocatalytic reduction of CO_2 to CO over Ag(110) and Cu(211) modeled by grand-canonical density functional theory. *J. Phys. Chem. C.* **2021**, *125*, 23773-83. DOI
23. Hossain, M. D.; Huang, Y.; Yu, T. H.; Goddard, W. A. I. I. I.; Luo, Z. Reaction mechanism and kinetics for CO_2 reduction on nickel single atom catalysts from quantum mechanics. *Nat. Commun.* **2020**, *11*, 2256. DOI PubMed PMC
24. Liu, H.; Yang, B. Potential-dependent C-C coupling mechanism and activity of C_2 formation in the electrocatalytic reduction of CO_2 on defective Cu(100) surfaces. *Chem. Commun.* **2022**, *58*, 709-12. DOI PubMed
25. Wexler, R. B.; Qiu, T.; Rappe, A. M. Automatic prediction of surface phase diagrams using ab initio grand canonical Monte Carlo. *J. Phys. Chem. C.* **2019**, *123*, 2321-8. DOI
26. Meng, J.; Freeze, J.; Nowack, L.; et al. Competitive carbonate binding hinders electrochemical CO_2 reduction to CO on Cu surfaces at low overpotentials. *J. Am. Chem. Soc.* **2025**, *147*, 25361-71. DOI PubMed PMC
27. Verga, L. G.; Wang, Y.; Chakraborty, T.; Da Silva, J. L. F.; Mueller, T. The effects of near-surface atomic order on the catalytic properties of Cu_3Au and $CuAu_3$ intermetallics for the CO_2 reduction reaction. *Catal. Sci. Technol.* **2023**, *13*, 6415-30. DOI
28. Zhang, S.; Tang, Q.; Zhu, B.; Gao, Y. Reaction-driven varieties of active sites on Cu(100) in electrochemical CO_2 reduction reaction. *ACS. Catal.* **2025**, *15*, 6497-506. DOI
29. Zhang, S.; Lv, H. B.; Shi, Z. Z.; Wang, R.; Zheng, S.; Li, J. F. Subsurface hydrogen as a hidden driver of copper surface reconstruction in CO_2 electroreduction. *Natl. Sci. Rev.* **2026**, *13*, nwag128. DOI PubMed PMC
30. Tang, Q.; Zhang, S.; Zhu, B.; Gao, Y. In situ reconstruction of a Cu(100) surface for promoted C–C coupling in CO_2 electroreduction from first-principles multiscale modeling. *ACS. Catal.* **2026**, *16*, 1325-37. DOI
31. Tian, X.; Tosello Gardini, A.; Raucci, U.; Xiao, H.; Zhuo, Y.; Parrinello, M. Electrochemical potential-driven water dynamics control CO_2 electroreduction at the Ag/H_2O interface. *Nat. Commun.* **2025**, *16*, 10636. DOI PubMed PMC

32. Sundararaman, R.; Vigil-Fowler, D.; Schwarz, K. Improving the accuracy of atomistic simulations of the electrochemical interface. *Chem. Rev.* **2022**, *122*, 10651-74. DOI PubMed PMC
33. Qin, X.; Vegge, T.; Hansen, H. A. Cation-coordinated inner-sphere CO_2 electroreduction at Au-water interfaces. *J. Am. Chem. Soc.* **2023**, *145*, 1897-905. DOI PubMed
34. Cheng, T.; Xiao, H.; Goddard, W. A. 3rd. Full atomistic reaction mechanism with kinetics for CO reduction on Cu(100) from ab initio molecular dynamics free-energy calculations at 298 K. *Proc. Natl. Acad. Sci. U. S. A.* **2017**, *114*, 1795-800. DOI PubMed PMC
35. Bussi, G.; Laio, A. Using metadynamics to explore complex free-energy landscapes. *Nat. Rev. Phys.* **2020**, *2*, 200-12. DOI
36. Johnson, E.; Haussener, S. Contrasting views of the electric double layer in electrochemical CO_2 reduction: continuum models vs molecular dynamics. *J. Phys. Chem. C. Nanomater. Interfaces.* **2024**, *128*, 10450-64. DOI PubMed PMC
37. Antolínez, S.; Jones, P. E.; Phillips, J. C.; Hadden-Perilla, J. A. AMBERff at scale: multimillion-atom simulations with AMBER force fields in NAMD. *J. Chem. Inf. Model.* **2024**, *64*, 543-54. DOI PubMed PMC
38. Chmiela, S.; Sauceda, H. E.; Müller, K. R.; Tkatchenko, A. Towards exact molecular dynamics simulations with machine-learned force fields. *Nat. Commun.* **2018**, *9*, 3887. DOI PubMed PMC
39. Groß, A.; Sakong, S. Ab initio simulations of water/metal interfaces. *Chem. Rev.* **2022**, *122*, 10746-76. DOI PubMed
40. Cheng, T.; Xiao, H.; Goddard, W. A. 3rd. Reaction mechanisms for the electrochemical reduction of CO_2 to CO and formate on the Cu(100) surface at 298 K from quantum mechanics free energy calculations with explicit water. *J. Am. Chem. Soc.* **2016**, *138*, 13802-5. DOI PubMed
41. Senftle, T. P.; Hong, S.; Islam, M. M.; et al. The ReaxFF reactive force-field: development, applications and future directions. *npj. Comput. Mater.* **2016**, *2*, 15011. DOI
42. Harrison, J. A.; Schall, J. D.; Maskey, S.; Mikulski, P. T.; Knippenberg, M. T.; Morrow, B. H. Review of force fields and intermolecular potentials used in atomistic computational materials research. *Appl. Phys. Rev.* **2018**, *5*, 031104. DOI
43. van Duin, A. C. T.; Dasgupta, S.; Lorant, F.; Goddard, W. A. ReaxFF: a reactive force field for hydrocarbons. *J. Phys. Chem. A.* **2001**, *105*, 9396-409. DOI
44. Buckley, A. K.; Lee, M.; Cheng, T.; et al. Electrocatalysis at organic-metal interfaces: identification of structure-reactivity relationships for CO_2 reduction at modified Cu surfaces. *J. Am. Chem. Soc.* **2019**, *141*, 7355-64. DOI PubMed
45. Unke, O. T.; Chmiela, S.; Sauceda, H. E.; et al. Machine learning force fields. *Chem. Rev.* **2021**, *121*, 10142-86. DOI PubMed PMC
46. Jinnouchi, R.; Minami, S. Machine learning force fields in electrochemistry: from fundamentals to applications. *ACS. Nano.* **2025**, *19*, 22600-44. DOI PubMed PMC
47. Jinnouchi, R.; Lahnsteiner, J.; Karsai, F.; Kresse, G.; Bokdam, M. Phase transitions of hybrid perovskites simulated by machine-learning force fields trained on the fly with bayesian inference. *Phys. Rev. Lett.* **2019**, *122*, 225701. DOI PubMed
48. Jinnouchi, R.; Karsai, F.; Verdi, C.; Asahi, R.; Kresse, G. Descriptors representing two- and three-body atomic distributions and their effects on the accuracy of machine-learned inter-atomic potentials. *J. Chem. Phys.* **2020**, *152*, 234102. DOI PubMed
49. Wang, R.; Fang, S.; Huang, Q.; Liu, Y. Constant-potential machine learning force field for the electrochemical interface. *J. Chem. Theory. Comput.* **2025**, *21*, 7628-35. DOI PubMed
50. Zhang, L.; Han, J.; Wang, H.; Saidi, W. A.; Car, R.; E, W. End-to-end symmetry preserving inter-atomic potential energy model for finite and extended systems. *arXiv* **2018**, arXiv:1805.09003. Available online: https://doi.org/10.48550/arXiv.1805.09003. (accessed 2026-09-30).
51. Batatia, I.; Kovács, D. P.; Simm, G. N. C.; Ortner, C.; Csányi, G. MACE: higher order equivariant message passing neural networks for fast and accurate force fields. *arXiv* **2022**, arXiv:2206.07697. Available online: https://doi.org/10.48550/arXiv.2206.07697. (accessed 2026-09-30).
52. Schran, C.; Behler, J.; Marx, D. Automated fitting of neural network potentials at coupled cluster accuracy: protonated water clusters as testing ground. *J. Chem. Theory. Comput.* **2020**, *16*, 88-99. DOI PubMed
53. Xing, M.; Zhang, Y.; Li, S.; He, H.; Sun, S. Prediction of carbon dioxide reduction catalyst using machine learning with a few-feature model: WLEDZ. *J. Phys. Chem. C.* **2022**, *126*, 17025-35. DOI
54. Abraham, B. M.; Piqué, O.; Khan, M. A.; Viñes, F.; Illas, F.; Singh, J. K. Machine learning-driven discovery of key descriptors for CO_2 activation over two-dimensional transition metal carbides and nitrides. *ACS. Appl. Mater. Interfaces.* **2023**, *15*, 30117-26. DOI PubMed PMC
55. Chen, H.; Yin, J.; Li, J.; Wang, X. Theoretical high-throughput screening of single-atom CO_2 electroreduction catalysts to methanol using active learning. *Engineering* **2025**, *52*, 172-82. DOI
56. Anselmi, M.; Slabaugh, G.; Crespo-Otero, R.; Di Tommaso, D. Molecular graph transformer: stepping beyond ALIGNN into long-range interactions. *Digit. Discov.* **2024**, *3*, 1048-57. DOI

57. Wan, X.; Zhang, Z.; Niu, H.; et al. Machine-learning-accelerated catalytic activity predictions of transition metal phthalocyanine dual-metal-site catalysts for CO_2 reduction. *J. Phys. Chem. Lett.* **2021**, *12*, 6111-8. DOI
58. Mok, D. H.; Li, H.; Zhang, G.; Lee, C.; Jiang, K.; Back, S. Data-driven discovery of electrocatalysts for CO_2 reduction using active motifs-based machine learning. *Nat. Commun.* **2023**, *14*, 7303. DOI PubMed PMC
59. Wang, Z.; Sun, Z.; Yin, H.; et al. The role of machine learning in carbon neutrality: catalyst property prediction, design, and synthesis for carbon dioxide reduction. *eScience* **2023**, *3*, 100136. DOI
60. Noh, J.; Chang, H. Data-driven prediction of configurational stability of molecule-adsorbed heterogeneous catalysts. *J. Chem. Inf. Model.* **2023**, *63*, 5981-95. DOI PubMed
61. Tran, R.; Lan, J.; Shuaibi, M.; et al. The open catalyst 2022 (OC22) dataset and challenges for oxide electrocatalysts. *ACS. Catal.* **2023**, *13*, 3066-84. DOI
62. Gholizadeh, R.; Pavlin, M.; Huš, M.; Likozar, B. Multiscale modeling of CO_2 electrochemical reduction on copper electrocatalysts: a review of advancements, challenges, and future directions. *ChemSusChem* **2025**, *18*, e202400898. DOI PubMed PMC
63. Raciti, D.; Mao, M.; Wang, C. Mass transport modelling for the electroreduction of CO_2 on Cu nanowires. *Nanotechnology* **2018**, *29*, 044001. DOI PubMed
64. Gupta, N.; Gattrell, M.; Macdougall, B. Calculation for the cathode surface concentrations in the electrochemical reduction of CO_2 in $KHCO_3$ solutions. *J. Appl. Electrochem.* **2006**, *36*, 161-72. DOI
65. Vinogradova, O.; Krishnamurthy, D.; Pande, V.; Viswanathan, V. Quantifying confidence in DFT-predicted surface pourbaix diagrams of transition-metal electrode-electrolyte interfaces. *Langmuir* **2018**, *34*, 12259-69. DOI PubMed
66. Anderson, A. B. Pourbaix diagrams for H_2O oxidation to adsorbed OH on Pt(111) and why they differ from those for bulk solids. *J. Phys. Chem. C.* **2018**, *122*, 9958-64. DOI
67. Russell, A. E. Electrocatalysis: theory and experiment at the interface. *Phys. Chem. Chem. Phys.* **2008**, *10*, 3607-8. DOI PubMed
68. Weitzner, S. E.; Dabo, I. Quantum–continuum simulation of underpotential deposition at electrified metal–solution interfaces. *npj. Comput. Mater.* **2017**, *3*, 4. DOI
69. Hori, Y.; Murata, A.; Takahashi, R. Formation of hydrocarbons in the electrochemical reduction of carbon dioxide at a copper electrode in aqueous solution. *J. Chem. Soc. Faraday. Trans. 1.* **1989**, *85*, 2309. DOI
70. Ooka, H.; Huang, J.; Exner, K. S. The sabatier principle in electrocatalysis: basics, limitations, and extensions. *Front. Energy. Res.* **2021**, *9*, 654460. DOI
71. Cai, J.; Zhao, Q.; Hsu, W. Y.; et al. Highly selective electrochemical reduction of CO_2 into methane on nanotwinned Cu. *J. Am. Chem. Soc.* **2023**, *145*, 9136-43. DOI PubMed PMC
72. Huang, Y.; Handoko, A. D.; Hirunsit, P.; Yeo, B. S. Electrochemical reduction of CO_2 using copper single-crystal surfaces: effects of CO* coverage on the selective formation of ethylene. *ACS. Catal.* **2017**, *7*, 1749-56. DOI
73. Cheng, D.; Nguyen, K. C.; Sumaria, V.; et al. Structure sensitivity and catalyst restructuring for CO_2 electro-reduction on copper. *Nat. Commun.* **2025**, *16*, 4064. DOI PubMed PMC
74. Zhu, C.; Zhang, Z.; Zhong, L.; et al. Product-specific active site motifs of Cu for electrochemical CO_2 reduction. *Chem* **2021**, *7*, 406-20. DOI
75. Verga, L. G.; Mendes, P. C. D.; Ocampo-Restrepo, V. K.; Da Silva, J. L. F. The role of site coordination on the CO_2 electroreduction pathway on stepped and defective copper surfaces. *Catal. Sci. Technol.* **2021**, *11*, 2770-81. DOI
76. Gholizadeh, R.; Pavlin, M.; Likozar, B.; Huš, M. Why including solvation is paramount: first-principles calculations of electrochemical CO_2 reduction to CO on a Cu electrocatalyst. *Chempluschem* **2025**, *90*, e202400346. DOI PubMed PMC
77. Kowalec, I.; Kabalan, L.; Catlow, C. R. A.; Logsdail, A. J. A computational study of direct CO_2 hydrogenation to methanol on Pd surfaces. *Phys. Chem. Chem. Phys.* **2022**, *24*, 9360-73. DOI PubMed
78. Chang, C. C.; Ku, M. S. Role of high-index facet Cu(711) surface in controlling the C2 selectivity for CO_2 reduction reaction - a DFT study. *J. Phys. Chem. C.* **2021**, *125*, 10919-25. DOI
79. Song, M.; Jiao, Z.; Jing, W.; Liu, Y.; Guo, L. Revealing the nature of C-C coupling sites on a Cu surface for CO_2 reduction. *J. Phys. Chem. Lett.* **2022**, *13*, 4434-40. DOI PubMed
80. Lin, W.; Ghulam Nabi, A.; Palma, M.; Di Tommaso, D. Copper nanowires for electrochemical CO_2 reduction reaction. *ACS. Appl. Nano. Mater.* **2024**, *7*, 27883-98. DOI
81. Xu, Y.; Li, F.; Xu, A.; et al. Low coordination number copper catalysts for electrochemical CO_2 methanation in a membrane electrode assembly. *Nat. Commun.* **2021**, *12*, 2932. DOI PubMed PMC
82. Raju, R. K.; Rodriguez, P.; Johnston, R. L. Can a single valence electron alter the electrocatalytic activity and selectivity for CO_2 reduction on the subnanometer scale? *J. Phys. Chem. C.* **2019**, *123*, 14591-609. DOI

83. Wu, Q. J.; Si, D. H.; Sun, P. P.; et al. Atomically precise copper nanoclusters for highly efficient electroreduction of CO_2 towards hydrocarbons via breaking the coordination symmetry of Cu site. *Angew. Chem. Int. Ed. Engl.* **2023**, *62*, e202306822. DOI PubMed
84. Reske, R.; Mistry, H.; Behafarid, F.; Roldan Cuenya, B.; Strasser, P. Particle size effects in the catalytic electroreduction of CO_2 on Cu nanoparticles. *J. Am. Chem. Soc.* **2014**, *136*, 6978-86. DOI PubMed
85. Mistry, H.; Behafarid, F.; Reske, R.; Varela, A. S.; Strasser, P.; Roldan Cuenya, B. Tuning catalytic selectivity at the mesoscale via interparticle interactions. *ACS. Catal.* **2016**, *6*, 1075-80. DOI
86. Bu, Y.; Zhao, M.; Zhang, G.; Zhang, X.; Gao, W.; Jiang, Q. Electroreduction of CO_2 on Cu clusters: the effects of size, symmetry, and temperature. *ChemElectroChem* **2019**, *6*, 1831-7. DOI
87. Nabi, A. G.; Ur-Rehman, A.; Hussain, A.; Di Tommaso, D. Ab initio random structure searching and catalytic properties of copper-based nanocluster with Earth-abundant metals for the electrocatalytic CO_2-to-CO conversion. *Mol. Catal.* **2022**, *527*, 112406. DOI
88. Duan, Y. X.; Meng, F. L.; Liu, K. H.; et al. Amorphizing of Cu nanoparticles toward highly efficient and robust electrocatalyst for CO_2 reduction to liquid fuels with high Faradaic efficiencies. *Adv. Mater.* **2018**, *30*, e1706194. DOI PubMed
89. Xiong, Y.; Wei, B.; Wu, M.; et al. Rapid synthesis of amorphous bimetallic copper-bismuth electrocatalysts for efficient electrochemical CO_2 reduction to formate in a wide potential window. *J. CO2. Util.* **2021**, *51*, 101621. DOI
90. Chen, C.; Yan, X.; Wu, Y.; et al. Oxidation of metallic Cu by supercritical CO_2 and control synthesis of amorphous nano-metal catalysts for CO_2 electroreduction. *Nat. Commun.* **2023**, *14*, 1092. DOI PubMed PMC
91. Song, M.; Jiao, Z.; Jing, W.; Liu, Y.; Guo, L. How *CO spill-over affects C–C coupling on amorphous Cu for converting CO_2 to multi-carbon products. *J. Catal.* **2023**, *428*, 115170. DOI
92. Muthuperiyanayagam, A.; Di Tommaso, D. Impact of amorphous structure on CO_2 electrocatalysis with Cu: a combined machine learning forcefield and DFT modelling approach. *Electrochim. Acta.* **2024**, *507*, 145188. DOI
93. Muthuperiyanayagam, A.; Pedretti, E.; Righi, M. C.; Tommaso, D. D. Optimized selectivity in CO_2 electrochemical reduction using amorphous CuNi catalysts: insights from density functional theory and machine learning simulations. *J. Energy. Chem.* **2026**, *112*, 1014-25. DOI
94. Feng, Y.; An, W.; Wang, Z.; Wang, Y.; Men, Y.; Du, Y. Electrochemical CO_2 reduction reaction on M@Cu(211) bimetallic single-atom surface alloys: mechanism, kinetics, and catalyst screening. *ACS. Sustain. Chem. Eng.* **2020**, *8*, 210-22. DOI
95. Liu, T.; Song, G.; Liu, X.; et al. Insights into the mechanism in electrochemical CO_2 reduction over single-atom copper alloy catalysts: a DFT study. *iScience* **2023**, *26*, 107953. DOI PubMed PMC
96. Clark, E. L.; Hahn, C.; Jaramillo, T. F.; Bell, A. T. Electrochemical CO_2 reduction over compressively strained CuAg surface alloys with enhanced multi-carbon oxygenate selectivity. *J. Am. Chem. Soc.* **2017**, *139*, 15848-57. DOI PubMed
97. Zhi, X.; Jiao, Y.; Zheng, Y.; Vasileff, A.; Qiao, S. Selectivity roadmap for electrochemical CO_2 reduction on copper-based alloy catalysts. *Nano. Energy.* **2020**, *71*, 104601. DOI
98. Li, Z.; Wang, P.; Lyu, X.; et al. Directing CO_2 electroreduction pathways for selective C2 product formation using single-site doped copper catalysts. *Nat. Chem. Eng.* **2024**, *1*, 159-69. DOI
99. Wang, T.; Dong, C.; Lin, J.; et al. Recent advances in carbon dioxide conversion: a circular bioeconomy perspective. *Sustainability* **2021**, *13*, 6962. DOI
100. Barberini, F.; Barile, A.; Restuccia, P.; et al. Dopant redox stability as a design principle for selective CO_2 electroreduction on Cu. *Phys. Chem. Chem. Phys.* **2026**, *28*, 21230-45. DOI PubMed PMC
101. Hoffman, Z. B.; Gray, T. S.; Moraveck, K. B.; Gunnoe, T. B.; Zangari, G. Electrochemical reduction of carbon dioxide to syngas and formate at dendritic copper–indium electrocatalysts. *ACS. Catal.* **2017**, *7*, 5381-90. DOI
102. Zhang, M.; Zhang, Z.; Zhao, Z.; et al. Tunable selectivity for electrochemical CO_2 reduction by bimetallic Cu–Sn catalysts: elucidating the roles of Cu and Sn. *ACS. Catal.* **2021**, *11*, 11103-8. DOI
103. Wan, L.; Zhang, X.; Cheng, J.; et al. Bimetallic Cu–Zn catalysts for electrochemical CO_2 reduction: phase-separated versus core–shell distribution. *ACS. Catal.* **2022**, *12*, 2741-8. DOI
104. Mitchell, S.; Pérez-Ramírez, J. Single atom catalysis: a decade of stunning progress and the promise for a bright future. *Nat. Commun.* **2020**, *11*, 4302. DOI PubMed PMC
105. Nguyen, T. N.; Salehi, M.; Le, Q. V.; Seifitokaldani, A.; Dinh, C. T. Fundamentals of electrochemical CO_2 reduction on single-metal-atom catalysts. *ACS. Catal.* **2020**, *10*, 10068-95. DOI
106. Zhang, J.; Cai, W.; Hu, F. X.; Yang, H.; Liu, B. Recent advances in single atom catalysts for the electrochemical carbon dioxide reduction reaction. *Chem. Sci.* **2021**, *12*, 6800-19. DOI PubMed PMC

107. Liang, Y.; Wu, C.; Meng, S.; et al. Ag single atoms anchored on CeO_2 with interfacial oxygen vacancies for efficient CO_2 electroreduction. *ACS. Appl. Mater. Interfaces.* **2023**, *15*, 30262-71. DOI PubMed

108. Yang, Z.; Zhang, J.; Tan, X.; et al. Manipulating the coordination environment of Cu single atoms via regulating ZrO_2 support crystal phases for enhanced CO_2 electroreduction. *J. Am. Chem. Soc.* **2025**, *147*, 35985-94. DOI PubMed

109. Chen, R.; Zhao, J.; Zhang, X.; et al. Visualizing catalytic dynamics of single-Cu-atom-modified SnS_2 in CO_2 electroreduction via rapid freeze-quench Mössbauer spectroscopy. *J. Am. Chem. Soc.* **2024**, *146*, 24368-76. DOI PubMed

110. Lin, Y.; Wang, M.; Xiang, Y.; et al. MoS_2 grain boundary-supported single-atom catalysts for efficient electrocatalytic CO_2 conversion to CO. *J. Phys. Chem. Lett.* **2026**, *17*, 1805-14. DOI PubMed

111. Yang, H.; Lin, Q.; Zhang, C.; et al. Carbon dioxide electroreduction on single-atom nickel decorated carbon membranes with industry compatible current densities. *Nat. Commun.* **2020**, *11*, 593. DOI PubMed PMC

112. Feng, J.; Gao, H.; Zheng, L.; et al. A Mn-N_3 single-atom catalyst embedded in graphitic carbon nitride for efficient CO_2 electroreduction. *Nat. Commun.* **2020**, *11*, 4341. DOI PubMed PMC

113. Qiao, B.; Wang, A.; Yang, X.; et al. Single-atom catalysis of CO oxidation using Pt1/FeOx. *Nat. Chem.* **2011**, *3*, 634-41. DOI

114. Martini, A.; Hursán, D.; Timoshenko, J.; et al. Tracking the evolution of single-atom catalysts for the CO_2 electrocatalytic reduction using operando X-ray absorption spectroscopy and machine learning. *J. Am. Chem. Soc.* **2023**, *145*, 17351-66. DOI PubMed PMC

115. Kim, H.; Shin, D.; Yang, W.; et al. Identification of single-atom Ni site active toward electrochemical CO_2 conversion to CO. *J. Am. Chem. Soc.* **2021**, *143*, 925-33. DOI PubMed

116. Pei, J.; Shang, H.; Mao, J.; et al. A replacement strategy for regulating local environment of single-atom Co-S_xN_{4-x} catalysts to facilitate CO_2 electroreduction. *Nat. Commun.* **2024**, *15*, 416. DOI PubMed PMC

117. Pan, F.; Li, B.; Sarnello, E.; et al. Pore-edge tailoring of single-atom iron–nitrogen sites on graphene for enhanced CO_2 reduction. *ACS. Catal.* **2020**, *10*, 10803-11. DOI

118. Zhang, H.; Wang, H.; Jia, S.; et al. CoN_4 active sites in a graphene matrix for the highly efficient electrocatalysis of CO_2 reduction. *New. Carbon. Mater.* **2022**, *37*, 734-42. DOI

119. Bi, W.; Li, X.; You, R.; et al. Surface immobilization of transition metal ions on nitrogen-doped graphene realizing high-efficient and selective CO_2 reduction. *Adv. Mater.* **2018**, *30*, e1706617. DOI PubMed

120. Han, L.; Song, S.; Liu, M.; et al. Stable and efficient single-atom Zn catalyst for CO_2 reduction to CH_4. *J. Am. Chem. Soc.* **2020**, *142*, 12563-7. DOI PubMed

121. Shang, H.; Wang, T.; Pei, J.; et al. Design of a single-atom indium$^{\delta+}$-N_4 interface for efficient electroreduction of CO_2 to formate. *Angew. Chem. Int. Ed. Engl.* **2020**, *59*, 22465-9. DOI PubMed

122. Bihua, H.; Hailin, C.; Zhiwei, L.; et al. Electronic regulation & improved conductivity of molecular catalysts as electrocatalysts. *Catal. Sci. Technol.* **2024**, *14*, 4127-31. DOI

123. Shi, G.; Zhang, W.; Kang, Y.; et al. Nanoconfinement promotes CO_2 electroreduction to methanol on a molecular catalyst. *Nat. Commun.* **2025**, *16*, 7359. DOI PubMed PMC

124. Tian, P.; Zhang, B.; Chen, J.; et al. Curvature-induced electronic tuning of molecular catalysts for CO_2 reduction. *Catal. Sci. Technol.* **2021**, *11*, 2491-6. DOI

125. Sui, R.; Wang, B.; Wang, Y.; et al. A general and facile calcination method to synthesize single-site catalysts for highly efficient electrochemical CO_2 reduction. *Nano. Res.* **2024**, *17*, 3895-901. DOI

126. Dai, Y.; Li, H.; Wang, C.; et al. Manipulating local coordination of copper single atom catalyst enables efficient CO_2-to-CH_4 conversion. *Nat. Commun.* **2023**, *14*, 3382. DOI PubMed PMC

127. Huang, M.; Deng, B.; Zhao, X.; et al. Template-sacrificing synthesis of well-defined asymmetrically coordinated single-atom catalysts for highly efficient CO_2 electrocatalytic reduction. *ACS. Nano.* **2022**, *16*, 2110-9. DOI PubMed

128. Su, P.; Iwase, K.; Nakanishi, S.; Hashimoto, K.; Kamiya, K. Nickel-nitrogen-modified graphene: an efficient electrocatalyst for the reduction of carbon dioxide to carbon monoxide. *Small* **2016**, *12*, 6083-9. DOI PubMed

129. Gul, S.; Nasim, F.; Nadeem, M. A. Single-atom metal-based electrocatalysts (Fe, Ni, and Co) for CO_2-to-CO conversion: a comprehensive review. *ACS. Appl. Energy. Mater.* **2025**, *8*, 11786-812. DOI

130. Li, X.; Bi, W.; Chen, M.; et al. Exclusive Ni-N_4 sites realize near-unity CO selectivity for electrochemical CO_2 reduction. *J. Am. Chem. Soc.* **2017**, *139*, 14889-92. DOI PubMed

131. Uddin, A. T.; Zhao, Q.; Toroz, D.; Crespo-Otero, R.; Di Tommaso, D. Computational screening of metalloporphyrin catalysts for the activation of carbon dioxide. *Mol. Catal.* **2024**, *565*, 114386. DOI

132. Sarma, S. C.; Barrio, J.; Bagger, A.; et al. Reaching the fundamental limitation in CO_2 reduction to CO with single atom catalysts. *Adv. Funct. Mater.* **2023**, *33*, 2302468. DOI
133. Hung, S. F.; Xu, A.; Wang, X.; et al. A metal-supported single-atom catalytic site enables carbon dioxide hydrogenation. *Nat. Commun.* **2022**, *13*, 819. DOI PubMed PMC
134. Fauzi, A.; Chen, X.; Zhao, H.; et al. Recent progress of M-N-C single atom electrocatalysts for carbon dioxide reduction reaction. *Next. Energy.* **2023**, *1*, 100045. DOI
135. Bai, X.; Zhao, Z.; Lu, G. Breaking the scaling relationship on single-atom embedded MBene for selective CO_2 electroreduction. *J. Phys. Chem. Lett.* **2023**, *14*, 5172-80. DOI PubMed
136. P, S.; John, J.; Rajan, T. P. D.; et al. Graphitic carbon nitride (g-C_3N_4) based heterogeneous single atom catalysts: synthesis, characterisation and catalytic applications. *J. Mater. Chem. A.* **2023**, *11*, 8599-646. DOI
137. Zhu, H.; Liu, S.; Yu, J.; Chen, Q.; Mao, X.; Wu, T. Computational screening of effective g-C_3N_4 based single atom electrocatalysts for the selective conversion of CO_2. *Nanoscale* **2023**, *15*, 8416-23. DOI PubMed
138. Shui, H.; Li, G.; Fu, C.; et al. A DFT study on the structural properties and CO_2 electrocatalytic reduction activity of monolayer graphitic carbon nitride supported Ag/Au single atom catalysts. *Surf. Sci.* **2025**, *754*, 122692. DOI
139. Baskaran, S.; Jung, J. Mo_2CS_2-MXene supported single-atom catalysts for efficient and selective CO_2 electrochemical reduction. *Appl. Surf. Sci.* **2022**, *592*, 153339. DOI
140. Al-Mahayni, H.; Yuan, R.; Seifitokaldani, A. A MXene-supported single atom catalyst selectively converts CO_2 into methanol and methane. *RSC. Sustain.* **2025**, *3*, 1729-40. DOI
141. Ren, Y.; Sun, X.; Qi, K.; Zhao, Z. Single atom supported on MoS_2 as efficient electrocatalysts for the CO_2 reduction reaction: a DFT study. *Appl. Surf. Sci.* **2022**, *602*, 154211. DOI
142. Ren, H.; Lang, Z.; Tan, H.; Wang, Y.; Li, Y. p-Block single-atom anchored MoS_2 monolayer for efficient electroreduction of CO_2 to formate via strong p–sp interaction. *J. Phys. Chem. C.* **2024**, *128*, 6702-10. DOI
143. Sun, Y.; Liu, L.; Liu, J. Theoretical study on the electrochemical CO_2 reduction performance of MoS_2-supported Ni single atoms with transition metal substrate doping. *Surf. Interfaces.* **2024**, *52*, 104938. DOI
144. Linghu, Y.; Tong, T.; Li, C.; Wu, C. The catalytic mechanism of CO_2 electrochemical reduction over transition metal-modified 1T'-MoS_2 monolayers. *Appl. Surf. Sci.* **2022**, *590*, 153001. DOI
145. Wang, X.; Wang, C.; Ren, H.; et al. Accelerating proton and electron transfer enables highly active Fe–N–C catalyst for electrochemical CO_2 reduction. *Adv. Funct. Mater.* **2024**, *34*, 2311818. DOI
146. Ao, C.; Zhao, W.; Ruan, S.; et al. Theoretical investigations of electrochemical CO_2 reduction by transition metals anchored on CNTs. *Sustain. Energy. Fuels.* **2020**, *4*, 6156-64. DOI
147. Lin, W.; Di Tommaso, D. Screening nitrogen-coordinated single atom catalysts on armchair carbon nanotubes for enhanced electrochemical CO_2 reduction to C_1 products. *ACS. Catal.* **2025**, *15*, 16463-75. DOI
148. Chen, Q.; Yang, H.; Wang, P.; Ke, Q.; Ge, X.; Chen, X. Charge transfer regulates electrocatalytic CO_2 reduction on one-dimensional carbon nanotube/boron nitride nanotube heterostructures. *Sep. Purif. Technol.* **2025**, *354*, 128981. DOI
149. Zhou, Y.; Chen, H. Electrocatalytic CO_2 conversion on boron nitride nanotubes by metal single-atom engineering. *Chem. Phys. Lett.* **2024**, *852*, 141518. DOI
150. Chen, Q.; Ke, Q.; Zhao, X.; Chen, X. Ruthenium-doped boron nitride nanotubes as promising electrocatalysts for carbon dioxide reduction to methane. *Diamond. Relat. Mater.* **2023**, *136*, 109942. DOI
151. Ma, A.; Pang, Y.; Ding, Z.; Fan, G.; Xu, H. Curvature effect of TMN_4 sites on carbon nanotube for electrochemical reduction of carbon dioxide revealed by machine learning. *Electrochim. Acta.* **2025**, *537*, 146862. DOI
152. Lv, K.; Wan, D.; Pan, R.; Suo, W.; Zhu, Y. Curvature of NCNTs induced selectivity of CO_2 electroreduction into CO. *Carbon. Neutral.* **2022**, *1*, 189-97. DOI
153. Su, J.; Musgrave, C. B.; Song, Y.; et al. Strain enhances the activity of molecular electrocatalysts via carbon nanotube supports. *Nat. Catal.* **2023**, *6*, 818-28. DOI
154. Jiang, K.; Siahrostami, S.; Zheng, T.; et al. Isolated Ni single atoms in graphene nanosheets for high-performance CO_2 reduction. *Energy. Environ. Sci.* **2018**, *11*, 893-903. DOI
155. Cui, Y.; Wu, Y.; Ren, C.; Li, Q.; Ling, C.; Wang, J. Beyond local coordination: how global structure engineers the selectivity of single atom catalysts for CO_2 reduction. *Angew. Chem. Int. Ed. Engl.* **2026**, *65*, e19826. DOI PubMed
156. Zhang, F.; Li, J.; Chen, Y.; et al. Highly coordinated Ni-N_5 sites for efficient electrocatalytic CO_2 reduction toward CO with Faradaic efficiency exceeding 99%. *J. Catal.* **2024**, *433*, 115495. DOI

157. Kim, J. H.; Kim, J.; Ma, J.; et al. Spontaneous metal-chelation strategy for highly dense Ni single-atom catalysts with asymmetric coordination in CO_2 electroreduction. *Small* **2025**, *21*, e2409481. DOI PubMed

158. Liu, X.; Liao, L.; Xia, G.; et al. An accurate "metal pre-buried" strategy for constructing Ni–N_2C_2 single-atom sites with high metal loadings toward electrocatalytic CO_2 reduction. *J. Mater. Chem. A.* **2022**, *10*, 25047-54. DOI

159. Han, Y.; Wei, Y.; Goswami, A.; Alexandrova, A. Uncovering the true active sites in Ni-N-C catalysts for CO_2 electroreduction. *J. Am. Chem. Soc.* **2025**, *147*, 38636-46. DOI PubMed

160. Luo, Z.; Yin, Z.; Yu, J.; et al. General synthetic strategy to ordered mesoporous carbon catalysts with single-atom metal sites for electrochemical CO_2 reduction. *Small* **2022**, *18*, e2107799. DOI PubMed

161. Bao, Y.; Xiao, J.; Huang, Y.; et al. Regulating spin polarization via axial nitrogen traction at Fe-N_5 sites enhanced electrocatalytic CO_2 reduction for Zn-CO_2 batteries. *Angew. Chem. Int. Ed. Engl.* **2024**, *63*, e202406030. DOI PubMed

162. Kong, Y.; Jia, X.; Chai, X.; et al. Modulating the local microenvironment over isolated nickel sites through first-shell coordination to regulate the reaction pathway of CO_2 electroreduction. *Natl. Sci. Rev.* **2025**, *12*, nwaf173. DOI PubMed PMC

163. Cao, S.; Wei, S.; Wei, X.; et al. Can N, S cocoordination promote single atom catalyst performance in CO_2RR? Fe-N_2S_2 porphyrin versus Fe-N_4 porphyrin. *Small* **2021**, *17*, e2100949. DOI PubMed

164. Li, Y.; Li, Y.; Sun, H.; et al. Current status and perspectives of dual-atom catalysts towards sustainable energy utilization. *Nanomicro. Lett.* **2024**, *16*, 139. DOI PubMed PMC

165. Zhao, X.; Zhao, K.; Liu, Y.; et al. Highly efficient electrochemical CO_2 reduction on a precise homonuclear diatomic Fe–Fe catalyst. *ACS. Catal.* **2022**, *12*, 11412-20. DOI

166. Zhang, N.; Zhang, X.; Kang, Y.; et al. A supported Pd_2 dual-atom site catalyst for efficient electrochemical CO_2 reduction. *Angew. Chem. Int. Ed. Engl.* **2021**, *60*, 13388-93. DOI PubMed

167. Liu, H.; Huang, Q.; An, W.; Wang, Y.; Men, Y.; Liu, S. Dual-atom active sites embedded in two-dimensional C_2N for efficient CO_2 electroreduction: a computational study. *J. Energy. Chem.* **2021**, *61*, 507-16. DOI

168. Ma, Z.; Zhong, Z.; Dou, Y.; Zhang, X. Enhanced C–C coupling in CO_2 electroreduction on dual-atom catalysts modified by bridge O/OH. *Appl. Surf. Sci.* **2024**, *672*, 160837. DOI

169. Wang, Z.; Ma, A.; Liu, Z.; et al. Density functional theory study of transition metal dual-atom anchored phthalocyanine as high-performance electrocatalysts for carbon dioxide reduction reaction. *Appl. Surf. Sci.* **2024**, *669*, 160532. DOI

170. Ren, W.; Tan, X.; Yang, W.; et al. Isolated diatomic Ni-Fe metal-nitrogen sites for synergistic electroreduction of CO_2. *Angew. Chem. Int. Ed. Engl.* **2019**, *58*, 6972-6. DOI PubMed

171. Zhao, Q.; Crespo-Otero, R.; Di Tommaso, D. The role of copper in enhancing the performance of heteronuclear diatomic catalysts for the electrochemical CO_2 conversion to C1 chemicals. *J. Energy. Chem.* **2023**, *85*, 490-500. DOI

172. Zhao, Z. H.; Huang, J. R.; Liao, P. Q.; Chen, X. M. Highly efficient electroreduction of CO_2 to ethanol via asymmetric C-C coupling by a metal-organic framework with heterodimetal dual sites. *J. Am. Chem. Soc.* **2023**, *145*, 26783-90. DOI PubMed

173. Chen, C.; Sun, Z.; Qin, G.; et al. Asymmetrically coordinated Cu dual-atom-sites enables selective CO_2 electroreduction to ethanol. *Adv. Mater.* **2024**, *36*, e2409797. DOI PubMed

174. Roongcharoen, T.; Mano, P.; Jitwatanasirikul, T.; et al. Theoretical insight on why N-vacancy promotes the selective CO_2 reduction to ethanol on NiMn doped graphitic carbon nitride sheets. *Appl. Surf. Sci.* **2022**, *595*, 153527. DOI

175. Bai, Z.; Zhi, Z.; Jiang, X. Z.; Luo, K. H. Rational design of dual-atom catalysts for electrochemical CO_2 reduction to C_1 and C_2 products with high activity and selectivity: a density functional theory study. *Ind. Eng. Chem. Res.* **2025**, *64*, 4378-87. DOI PubMed PMC

176. Sun, G.; Cao, Y.; Li, D.; et al. Dual-atom Cu_2/N-doped carbon catalyst for electroreduction of CO_2 to C_2H_4. *Appl. Catal. A. Gen.* **2023**, *651*, 119025. DOI

177. Hensley, A. J. R.; Ghale, K.; Rieg, C.; et al. DFT-based method for more accurate adsorption energies: an adaptive sum of energies from RPBE and vdW density functionals. *J. Phys. Chem. C.* **2017**, *121*, 4937-45. DOI

178. Lei, J.; Zhu, T. Impact of potential and active-site environment on single-iron-atom-catalyzed electrochemical CO_2 reduction from accurate quantum many-body simulations. *ACS. Catal.* **2024**, *14*, 3933-42. DOI

179. Zhi, X.; Jiao, Y.; Zheng, Y.; Qiao, S. Z. Impact of interfacial electron transfer on electrochemical CO_2 reduction on graphitic carbon nitride/doped graphene. *Small* **2019**, *15*, e1804224. DOI PubMed

180. Wang, Y.; Tian, Y.; Yan, L.; Su, Z. DFT study on sulfur-doped g-C_3N_4 nanosheets as a photocatalyst for CO_2 reduction reaction. *J. Phys. Chem. C.* **2018**, *122*, 7712-9. DOI

181. Siahrostami, S.; Jiang, K.; Karamad, M.; Chan, K.; Wang, H.; Nørskov, J. Theoretical investigations into defected graphene for electrochemical reduction of CO_2. *ACS. Sustain. Chem. Eng.* **2017**, *5*, 11080-5. DOI

182. Mishra, A. K.; Roldan, A.; de Leeuw, N. H. A density functional theory study of the adsorption behaviour of CO_2 on Cu_2O surfaces. *J. Chem. Phys.* **2016**, *145*, 044709. DOI PubMed
183. Gallagher, C.; Zhao, Q. Multireference wavefunction methods for accurate adsorption energies on single-atom catalysts. *J. Catal.* **2026**, *462*, 117069. DOI
184. Misra, D.; Di Liberto, G.; Pacchioni, G. CO_2 electroreduction on single atom catalysts: the role of the DFT functional. *Phys. Chem. Chem. Phys.* **2024**, *26*, 10746-56. DOI PubMed
185. He, S.; Cao, G.; Nie, J.; Li, S.; Ren, J. Essential role of self-interaction correction in single-atom catalysis: from electronic structure to activity predictions. *Phys. Rev. B.* **2026**, *113*, 235413. DOI
186. Han, Z.; Han, D.; Chen, Z.; et al. Steering surface reconstruction of copper with electrolyte additives for CO_2 electroreduction. *Nat. Commun.* **2022**, *13*, 3158. DOI PubMed PMC
187. Zhu, J.; Chen, J. L.; Qi, X. Z.; et al. Electron-rich subnanometer Cu clusters facilitate CO-CO coupling in CO_2 electroreduction. *J. Am. Chem. Soc.* **2026**, *148*, 4008-19. DOI PubMed
188. Duan, Z.; Henkelman, G. Surface charge and electrostatic spin crossover effects in CoN_4 electrocatalysts. *ACS. Catal.* **2020**, *10*, 12148-55. DOI
189. Shen, J.; Kolb, M. J.; Göttle, A. J.; Koper, M. T. M. DFT study on the mechanism of the electrochemical reduction of CO_2 catalyzed by cobalt porphyrins. *J. Phys. Chem. C.* **2016**, *120*, 15714-21. DOI
190. Sun, M.; Staykov, A.; Yamauchi, M. Understanding the roles of hydroxide in CO_2 electroreduction on a Cu electrode for achieving variable selectivity. *ACS. Catal.* **2022**, *12*, 14856-63. DOI
191. Li, C.; Guo, Z.; Liu, Z.; et al. Boosting electrochemical CO_2 reduction via surface hydroxylation over Cu-based electrocatalysts. *ACS. Catal.* **2023**, *13*, 16114-25. DOI
192. Iijima, G.; Inomata, T.; Yamaguchi, H.; Ito, M.; Masuda, H. Role of a hydroxide layer on Cu electrodes in electrochemical CO_2 reduction. *ACS. Catal.* **2019**, *9*, 6305-19. DOI
193. Cao, Y.; Chen, Z.; Li, P.; et al. Surface hydroxide promotes CO_2 electrolysis to ethylene in acidic conditions. *Nat. Commun.* **2023**, *14*, 2387. DOI PubMed PMC
194. Buckley, A. K.; Cheng, T.; Oh, M. H.; et al. Approaching 100% selectivity at low potential on Ag for electrochemical CO_2 reduction to CO using a surface additive. *ACS. Catal.* **2021**, *11*, 9034-42. DOI
195. Xu, W.; Qiu, Y.; Zhang, T.; Li, X.; Zhang, H. The effect of organic additives on the activity and selectivity of CO_2 electroreduction: the role of functional groups. *ChemSusChem* **2018**, *11*, 2904-11. DOI
196. Qiu, Y.; Zhong, H.; Xu, W.; Zhang, T.; Li, X.; Zhang, H. Tuning the electrocatalytic properties of a Cu electrode with organic additives containing amine group for CO_2 reduction. *J. Mater. Chem. A.* **2019**, *7*, 5453-62. DOI
197. Wang, H.; Lu, R.; Dong, C.; Du, X.; Liang, H. Glycine modified copper promotes CO_2 electroreduction to multi-carbon products: a computational study. *Phys. Chem. Chem. Phys.* **2024**, *26*, 22314-8. DOI
198. Wang, J.; Cheng, T.; Fenwick, A. Q.; et al. Selective CO_2 electrochemical reduction enabled by a tricomponent copolymer modifier on a copper surface. *J. Am. Chem. Soc.* **2021**, *143*, 2857-65. DOI PubMed
199. Zhang, Z.; Li, H.; Shao, Y.; et al. Molecular understanding of the critical role of alkali metal cations in initiating CO_2 electroreduction on Cu(100) surface. *Nat. Commun.* **2024**, *15*, 612. DOI PubMed PMC
200. Yang, X.; Ding, H.; Li, S.; Zheng, S.; Li, J. F.; Pan, F. Cation-induced interfacial hydrophobic microenvironment promotes the C-C coupling in electrochemical CO_2 reduction. *J. Am. Chem. Soc.* **2024**, *146*, 5532-42. DOI PubMed
201. Ringe, S.; Clark, E. L.; Resasco, J.; et al. Understanding cation effects in electrochemical CO_2 reduction. *Energy. Environ. Sci.* **2019**, *12*, 3001-14. DOI
202. Gu, J.; Liu, S.; Ni, W.; Ren, W.; Haussener, S.; Hu, X. Modulating electric field distribution by alkali cations for CO_2 electroreduction in strongly acidic medium. *Nat. Catal.* **2022**, *5*, 268-76. DOI
203. Marcandalli, G.; Goyal, A.; Koper, M. T. M. Electrolyte effects on the Faradaic efficiency of CO_2 reduction to CO on a gold electrode. *ACS. Catal.* **2021**, *11*, 4936-45. DOI PubMed PMC
204. Liu, X.; Schlexer, P.; Xiao, J.; et al. pH effects on the electrochemical reduction of $CO_{(2)}$ towards C(2) products on stepped copper. *Nat. Commun.* **2019**, *10*, 32. DOI PubMed PMC
205. Kastlunger, G.; Heenen, H. H.; Govindarajan, N. Combining first-principles kinetics and experimental data to establish guidelines for product selectivity in electrochemical CO_2 reduction. *ACS. Catal.* **2023**, *13*, 5062-72. DOI
206. Lee, T.; Lee, Y.; Eo, J.; Nam, D. H. Acidic CO_2 electroreduction for high CO_2 utilization: catalysts, electrodes, and electrolyzers. *Nanoscale* **2024**, *16*, 2235-49. DOI PubMed

207. Hicks, M. H.; Nie, W.; Boehme, A. E.; Atwater, H. A.; Agapie, T.; Peters, J. C. Electrochemical CO_2 reduction in acidic electrolytes: spectroscopic evidence for local pH gradients. *J. Am. Chem. Soc.* **2024**, *146*, 25282-9. DOI PubMed PMC
208. Fan, M.; Huang, J. E.; Miao, R. K.; et al. Cationic-group-functionalized electrocatalysts enable stable acidic CO_2 electrolysis. *Nat. Catal.* **2023**, *6*, 763-72. DOI
209. Huang, J. E.; Li, F.; Ozden, A.; et al. CO_2 electrolysis to multicarbon products in strong acid. *Science* **2021**, *372*, 1074-8. DOI PubMed
210. Monteiro, M. C. O.; Philips, M. F.; Schouten, K. J. P.; Koper, M. T. M. Efficiency and selectivity of CO_2 reduction to CO on gold gas diffusion electrodes in acidic media. *Nat. Commun.* **2021**, *12*, 4943. DOI PubMed PMC
211. Xie, Y.; Ou, P.; Wang, X.; et al. High carbon utilization in CO_2 reduction to multi-carbon products in acidic media. *Nat. Catal.* **2022**, *5*, 564-70. DOI
212. Henkelman, G.; Uberuaga, B. P.; Jónsson, H. A climbing image nudged elastic band method for finding saddle points and minimum energy paths. *J. Chem. Phys.* **2000**, *113*, 9901-4. DOI
213. Henkelman, G.; Jónsson, H. A dimer method for finding saddle points on high dimensional potential surfaces using only first derivatives. *J. Chem. Phys.* **1999**, *111*, 7010-22. DOI
214. Mathew, K.; Sundararaman, R.; Letchworth-Weaver, K.; Arias, T. A.; Hennig, R. G. Implicit solvation model for density-functional study of nanocrystal surfaces and reaction pathways. *J. Chem. Phys.* **2014**, *140*, 084106. DOI PubMed
215. Bramley, G.; Nguyen, M. T.; Glezakou, V. A.; Rousseau, R.; Skylaris, C. K. Reconciling work functions and adsorption enthalpies for implicit solvent models: a Pt (111)/water interface case study. *J. Chem. Theory. Comput.* **2020**, *16*, 2703-15. DOI PubMed
216. Hörmann, N. G.; Guo, Z.; Ambrosio, F.; Andreussi, O.; Pasquarello, A.; Marzari, N. Absolute band alignment at semiconductor-water interfaces using explicit and implicit descriptions for liquid water. *npj. Comput. Mater.* **2019**, *5*, 238. DOI
217. Islam, S. M. R.; Khezeli, F.; Ringe, S.; Plaisance, C. An implicit electrolyte model for plane wave density functional theory exhibiting nonlinear response and a nonlocal cavity definition. *J. Chem. Phys.* **2023**, *159*, 234117. DOI
218. Perego, S.; Bonati, L. Data efficient machine learning potentials for modeling catalytic reactivity via active learning and enhanced sampling. *npj. Comput. Mater.* **2024**, *10*, 1481. DOI
219. Ding, R.; Chen, J.; Chen, Y.; Liu, J.; Bando, Y.; Wang, X. Unlocking the potential: machine learning applications in electrocatalyst design for electrochemical hydrogen energy transformation. *Chem. Soc. Rev.* **2024**, *53*, 11390-461. DOI
220. Mou, L. H.; Han, T.; Smith, P. E. S.; Sharman, E.; Jiang, J. Machine learning descriptors for data-driven catalysis study. *Adv. Sci.* **2023**, *10*, e2301020. DOI PubMed PMC
221. Song, Z.; Fan, L.; Lu, S.; Ling, C.; Zhou, Q.; Wang, J. Inverse design of promising electrocatalysts for CO_2 reduction via generative models and bird swarm algorithm. *Nat. Commun.* **2025**, *16*, 1053. DOI PubMed PMC

Disclaimer/Publisher's Note: All statements, opinions, and data contained in this publication are solely those of the individual author(s) and contributor(s) and do not necessarily reflect those of OAE and/or the editor(s). OAE and/or the editor(s) disclaim any responsibility for harm to persons or property resulting from the use of any ideas, methods, instructions, or products mentioned in the content.

© The Author(s) 2026. Open Access This article is licensed under a Creative Commons Attribution 4.0 International License (https://creativecommons.org/licenses/by/4.0/), which permits unrestricted use, sharing, adaptation, distribution and reproduction in any medium or format, for any purpose, even commercially, as long as you give appropriate credit to the original author(s) and the source, provide a link to the Creative Commons license, and indicate if changes were made.